

High Energy Spin- and Momentum-Resolved Photoelectron Spectroscopy of Complex Oxides



Dissertation zur Erlangung des
naturwissenschaftlichen Doktorgrades der
Julius-Maximilians-Universität Würzburg

vorgelegt von

Matthias Schmitt

aus

Weißenburg in Bayern

Würzburg, 2021

Eingereicht am 30.11.2021

bei der Fakultät für Physik und Astronomie

1. Gutachter: Prof. Dr. Ralph Claessen
2. Gutachter: Prof. Dr. Gerd Schönhense
3. Gutachter:
der Dissertation

Vorsitzende(r): Prof. Dr. Vladimir Dyakonov

1. Prüfer: Prof. Dr. Ralph Claessen
 2. Prüfer: Prof. Dr. Gerd Schönhense
 3. Prüfer: Prof. Dr. Giorgio Sangiovanni
- im Promotionskolloquium

Tag des Promotionskolloquiums: 21.03.2022

Doktorurkunde ausgehändigt am:

Abstract

Spin- and k -resolved hard X-ray photoelectron spectroscopy (HAXPES) is a powerful tool to probe bulk electronic properties of complex metal oxides. Due to the low efficiency of common spin detectors of $\approx 10^{-4}$, such experiments have been rarely performed within the hard X-ray regime since the notoriously low photoionization cross sections further lower the performance tremendously. This thesis is about a new type of spin detector, which employs an imaging spin-filter with multichannel electron recording. This increases the efficiency by a factor of 10^4 and makes spin- and k -resolved photoemission at high excitation energies possible. Two different technical approaches were pursued in this thesis: One using a hemispherical deflection analyzer (HDA) and a separate external spin detector chamber, the other one resorting to a momentum- or k -space microscope with time-of-flight (TOF) energy recording and an integrated spin-filter crystal. The latter exhibits significantly higher count rates and—since it was designed for this purpose from scratch—the integrated spin-filter option found out to be more viable than the subsequent upgrade of an existing setup with an HDA. This instrumental development is followed by the investigation of the complex metal oxides (CMOs) KTaO_3 by angle-resolved HAXPES (HARPES) and Fe_3O_4 by spin-resolved HAXPES (spin-HAXPES), respectively.

KTaO_3 (KTO) is a band insulator with a valence-electron configuration of Ta $5d^0$. By angle- and spin-*integrated* HAXPES it is shown that at the buried interface of $\text{LaAlO}_3/\text{KTO}$ —by the generation of oxygen vacancies and hence effective electron doping—a conducting electron system forms in KTO. Further investigations using the momentum-resolution of the k -space TOF microscope show that these states are confined to the surface in KTO and intensity is only obtained from the center or the Γ -point of each Brillouin zone (BZ). These BZs are furthermore square-like arranged reflecting the three-dimensional cubic crystal structure of KTO. However, from a comparison to calculations it is found that the band structure deviates from that of electron-doped bulk KTaO_3 due to the confinement to the interface.

There is broad consensus that Fe_3O_4 is a promising material for spintronics applications due to its high degree of spin polarization at the Fermi level. However, previous attempts to measure the spin polarization by spin-resolved photoemission spectroscopy have been hampered by the use of *low photon energies* resulting in high surface sensitivity. The surfaces of magnetite, though, tend to reconstruct due to their polar nature, and thus their magnetic and electronic properties may strongly deviate from each other and from the bulk, dependent on their orientation and specific preparation. In this work, the intrinsic bulk spin polarization of magnetite at the Fermi level (E_F) by spin-resolved photoelectron spectroscopy, is determined by spin-HAXPES on (111)-oriented thin films, epitaxially grown on $\text{ZnO}(0001)$ to be $P(E_F) = -80_{-20}^{+10}\%$.

Zusammenfassung

Spin- und k -aufgelöste harte Röntgenphotoelektronenspektroskopie (HAXPES) ist ein leistungsfähiges Werkzeug zur Untersuchung der elektronischen Eigenschaften komplexer Metalloxide. Aufgrund der geringen Effizienz gängiger Spin-Detektoren von etwa 10^{-4} wurden solche Experimente im Bereich der harten Röntgenstrahlung nur selten durchgeführt, da die notorisch niedrigen Photoionisationsquerschnitte die Leistungsfähigkeit noch weiter verringern. In dieser Arbeit geht es um einen neuartigen Spin-Detektor, der einen abbildenden Spin-Filter mit Mehrkanal-Elektronenaufzeichnung verwendet. Dies erhöht die Effizienz um einen Faktor 10^4 und ermöglicht spin- und k -aufgelöste Photoemission bei hohen Anregungsenergien. Zwei verschiedene technische Ansätze werden in der vorliegenden Arbeit verfolgt: Zum einen mit einem Halbkugelanalysator (HDA) und einer separaten externen Spin-Detektorkammer, zum anderen mit einem Impuls- oder Impuls-Mikroskop mit Flugzeit-Energieaufzeichnung (TOF) und einem integrierten Spin-Filterkristall. Letzteres weist deutlich höhere Zählraten auf, und—da es von Grund auf für diesen Zweck entwickelt wurde—erwies sich die integrierte Spinfilteroption als praktikabler als die nachträgliche Ausrüstung des bestehenden Aufbaus mit einem HDA. Auf diese instrumentelle Entwicklung folgt die Untersuchung der komplexen Metalloxide (CMOs) KTaO_3 durch winkelaufgelöstes HAXPES (HARPES) und Fe_3O_4 durch spinaufgelöstes HAXPES (spin-HAXPES).

KTaO_3 (KTO) ist ein Bandisolator mit einer Valenz-Elektronenkonfiguration von $\text{Ta } 5d^0$. Durch winkel- und spin-integriertes HAXPES wird gezeigt, dass sich an der vergrabenen Grenzfläche von $\text{dLaAlO}_3/\text{KTO}$ —durch die Erzeugung von Sauerstoff-Fehlstellen und damit effektiver Elektronendotierung—ein leitendes Elektronensystem in KTO bildet. Weitere Untersuchungen mit der Impulsauflösung des TOF-Mikroskops im k -Raum zeigen, dass diese Zustände auf die Oberfläche in KTO beschränkt sind und die Intensität nur vom Zentrum oder dem Γ -Punkt jeder Brillouin-Zone (BZ) gemessen wird. Diese BZn sind darüber hinaus quadratisch angeordnet, was die dreidimensionale kubische Kristallstruktur von KTO widerspiegelt. Aus einem Vergleich mit Bandrechnungen geht jedoch hervor, dass die Bandstruktur aufgrund des Einschlusses an der Grenzfläche von der des elektronen-dotierten KTO-Volumens abweicht.

Es besteht ein breiter Konsens darüber, dass Fe_3O_4 aufgrund seines hohen Grades an Spinpolarisation am Fermi-Niveau ein vielversprechendes Material für Spintronik-Anwendungen ist. Bisherige Versuche, die Spinpolarisation durch spinaufgelöste Photoemissionsspektroskopie zu messen, wurden jedoch durch die Verwendung von *niedrigen Photonenergien* behindert, was zu einer hohen Oberflächenempfindlichkeit führt. Die Oberflächen von Magnetit neigen jedoch aufgrund ihres polaren Charakters zu Rekonstruktionen, so dass ihre magnetischen und elektronischen Eigenschaften stark voneinander und vom Volumen abweichen können, abhängig von ihrer Oberflächenorientierung und ihrer spezifischen Präparation. In dieser Arbeit wird die intrinsische Bulk-Spinpolarisation von Magnetit am Fermi-Niveau (E_F) durch spinaufgelöste Photoelektronenspektroskopie an (111)-orientierten dünnen Filmen, die epitaktisch auf $\text{ZnO}(0001)$ gewachsen sind, zu $P(E_F) = -80_{-20}^{+10} \%$ bestimmt.

Contents

1	Introduction	1
2	Material Systems	3
2.1	Potassium Tantalate KTaO_3	3
2.1.1	Perovskite Crystal Structure	4
2.1.2	Electronic Structure	5
2.2	Magnetite Fe_3O_4	6
2.2.1	Inverse-Spinel Crystal Structure	7
2.2.2	Electronic Structure and Magnetism	8
2.2.3	Theoretical Description of the Valence Band Spin Polarization	9
2.2.3.1	Density-Functional Theory Calculations	9
2.2.3.2	Model of Photoemission from Localized Fe 3d States	12
2.2.4	Previous Experimental Studies	13
2.3	Summary	14
3	Principles of Photoemission	17
3.1	Energetics and Kinematics	17
3.2	Many Body Description	19
3.3	The Role of Excitation Energy	21
3.4	Synchrotron-based Hard X-ray Radiation	24
4	Spin-Resolved Photoelectron Spectroscopy	29
4.1	Quantum Mechanical Description of the Electron Spin	30
4.2	Spin-Orbit Interaction	31
4.3	Differential Scattering Cross Sections	34
4.4	Different Concepts of Spin Detectors	37
4.4.1	Mott Detector	38
4.4.2	Low-Energy Electron Diffraction of Spin-Polarized Electrons	41
4.4.3	Imaging Spin-Filtering with Multichannel Detection	43
4.5	Summary and Discussion	44
5	Concepts and Implementation of a Spin-HAXPES Endstation	47
5.1	Hemispherical Deflection Analyzer with External Spin Detector	48
5.1.1	Basic Principles	48
5.1.2	Spin-Filter Surface Preparation	54
5.1.2.1	Two-Step Flashing Procedure	55

5.1.2.2	Electron Diffraction Study of the Surface	56
5.1.3	First Measurements and Characterization	58
5.2	Time-of-Flight Microscope with Integrated Spin-Filter	66
5.2.1	Basic Principles and Comparison to a Hemispherical Analyzer	67
5.2.2	TOF-based Spin- and k-resolved Photoelectron Spectroscopy	71
5.2.3	Future Instrumental Developments	78
5.3	Summary	81
6	Buried Electron System in the LaAlO₃/KTaO₃ Heterostructure	83
6.1	Electronic Properties of the LAO/KTO-Interface	83
6.2	Momentum-Resolved Hard X-ray Time-of-Flight Photoemission of the 2DES	83
6.3	Summary	88
7	Determination of the Valence-Band Spin Polarization of Magnetite	89
7.1	Thin Film Growth and Characterization of Fe ₃ O ₄ (111) on ZnO(0001)	89
7.1.1	Low and High Energy Electron Diffraction	89
7.1.2	X-ray Photoelectron Spectroscopy	90
7.1.3	X-ray Magnetic Circular Dichroism	91
7.2	Spin-Resolved Photoemission of the Valence Band	92
7.3	Summary and Discussion	96
8	Conclusion	99
	Bibliography	101
	Appendix	115
	List of Own Publications	119
	Danksagung	121

List of Figures

2.1	Unit cell of a cubic perovskite ABO_3	4
2.2	Crystal field splitting and surface confinement potential in KTO	6
2.3	Schematic view of the Datta-Das spintransistor	7
2.4	Inverse-spinel unit cell of magnetite	8
2.5	High-spin electron configuration of magnetite	9
2.6	Total and site-decomposed spin-resolved DOS of magnetite	10
2.7	Spin-resolved DOS of magnetite	11
2.8	Photoemission process from a localized $\text{Fe}^{2+} 3d^6$ shell	12
3.1	Scheme of the photon-in electron-out process of photoemission	18
3.2	Momentum conservation in the photoemission process	19
3.3	Inelastic mean free path λ_{IMFP} of photoelectrons	22
3.4	Scheme of the electron synchrotron PETRA III	24
3.5	Energy bandwidth as a function of photon energy	26
3.6	Photon flux for different harmonics	27
4.1	Stern-Gerlach experiment	29
4.2	Illustration of the two possible spin states <i>up</i> and <i>down</i>	30
4.3	Scattering scheme of two electron beams passing the nucleus	34
4.4	Schematic view of the left-right asymmetry	37
4.5	Schematic view of a Mott detector	38
4.6	Schematic view of the first SPLEED detector	41
4.7	Rotation diagrams for a (0,0) beam with 100 eV	42
4.8	Schematic of imaging spin-filtering	43
4.9	Reflectivity and Asymmetry of Au/Ir(100)	45
4.10	Overview of the development of the FoM of different spin detectors	46
5.1	Schematic view of a hemispherical deflection analyzer	49
5.2	Photoemission spectra of Au for different analyzer modes	52
5.3	Schematic view of the experimental setup of the HDA	53
5.4	Electrostatic lens potentials of the spin detector	53
5.5	Energy dependent reflectivity and Sherman function of W(001)	54
5.6	Illustration of the crystal holder with the electron bombardment heating	55
5.7	RGA spectra during the flashing cycles	56
5.8	Overview of different LEED patterns corresponding to different carbon densities	57
5.9	LEED patterns recorded after full cleaning cycles	58

5.10	Experimentally determined reflectivity of the spin-filter as function of scattering energy	59
5.11	Stability of the reflectivity	60
5.12	Detector image of the O 1s and Au 4f peaks	61
5.13	Background of the detector image	62
5.14	Spin-resolved valence band of magnetite	63
5.15	Reproducibility of consecutive measurements	65
5.16	Magnetite valence band measured with and without spin detector	66
5.17	Schematic view of the k -space microscope lens system	68
5.18	Energy resolution and time-of-flight of the momentum microscope	70
5.19	Constant energy maps and band maps of Mo(110)	72
5.20	Survey spectrum of a GaIn _{3%} Mn _{2.5%} As sample	73
5.21	Simplified schematic view of the TOF-based hXPD	74
5.22	Hard X-ray mapping of the valence band of Re(0001)	76
5.23	Different core-level spectra with the corresponding diffractograms	77
5.24	Momentum microscope with imaging spin-filter inserted	78
5.25	Built-in z-chicane	79
5.26	TOF-Booster concept	81
5.27	Images of the installed endstations	82
6.1	Ta 4f and valence-band spectra of dLAO/KTO	84
6.2	Fermi surface maps at different photon energies of the dLAO/KTO heterostructure	85
6.3	Optimized Fermi surface map and band map of the dLAO/KTO heterostructure	87
7.1	Electron diffraction on magnetite	90
7.2	XPS spectra of Fe 2p and the valence band	91
7.3	XMCD measurements of the magnetite sample	92
7.4	Raw data of the spin-resolved measurements on magnetite	93
7.5	Sherman function of the spin-filter crystal	94
7.6	Experimentally determined spin polarization of magnetite	95
7.7	Experimentally determined spin-DOS of magnetite	97
A.1	Schematic view and working principle of an MCP and a DLD	116
A.2	Time scan of the chamber pressure during 750 LPFs	117
A.3	LEED image after preparation cycle in a contaminated atmosphere	118

List of Acronyms

- ARPES** Angle-Resolved Resolved Photoemission/Photoelectron Spectroscopy
- APW** Augmented-Plane-Wave
- ASW** Augmented-Spherical-Waves
- BZ** Brillouin Zone
- CAE** Constant Analyzer Energy
- CRR** Constant Retard Ratio
- DC** Direct Current
- DCM** Double Crystal Monochromator
- DFT** Density-Functional Theory
- DLD** Delayline Detector
- DOS** Density of States
- ESCA** Electron Spectroscopy for Chemical Analysis
- HARPES** Angle-Resolved Hard X-ray Photoemission/Photoelectron Spectroscopy
- HAXPES** Hard X-ray Photoemission/Photoelectron Spectroscopy
- HDA** Hemispherical Deflection Analyzer
- HPF** High Power Flash
- hXPD** Hard X-ray Photoelectron Diffraction
- FLL-DCC** Fully Localized Limit - Double Counting Corrected
- FoM** Figure-of-Merit
- GGA** General Gradient Approximation
- IMFP** Inelastic Mean Free Path
- LDA** Local Density Approximation

LEED Low-Energy Electron Diffraction

LPF Low Power Flash

LSDA Local Spin Density Approximation

MBE Molecular Beam Epitaxy

MCP Microchannel Plate

nsc Natural Single Crystal

PAW Projector Augmented Wave

PES Photoemission/Photoelectron Spectroscopy

PLD Pulsed Laser Deposition

q2DES Quasi-Two Dimensional Electron System

RGA Residual Gas Analyzer

SCAN Strongly Constrained and Appropriately Normed

SCC-DFTBN Self-Consistent Charge Density-Functional Tight Binding

SOC Spin-Orbit Coupling

spin-DOS Spin-Resolved Density of States

SPLEED Low-Energy Electron Diffraction of Spin-Polarized Electrons

SQUID Superconducting Quantum Interference Device

TBLMTO Tight Binding Linear Muffin-Tin Orbital

TOF Time-of-Flight

UHV Ultrahigh Vacuum

VLEED Very Low-Energy Electron Diffraction

XMCD X-ray Magnetic Circular Dichroism

XRD X-ray Diffraction

XPS X-ray Photoelectron Spectroscopy

+U Correlation effects are taken into account

1 Introduction

In 1916, P. Debye and A. Sommerfeld predicted a *space quantization* of electrons based on their findings from experiments on the Zeeman effect [1]. Later, in 1922, O. Stern and W. Gerlach [2] conducted an experiment that proved the Bohr-Sommerfeld hypothesis that states that the direction of the angular momentum of a silver atom is quantized. Based on these findings, in 1925, G. E. Uhlenbeck and S. Goudsmith [3] were the first to propose the electron *spin*, which was completed by W. Pauli using matrices and multi-component wave functions to establish a non-relativistic formulation based on quantum mechanics—previously introduced by the work of Schrödinger and Heisenberg [4]. In 1928, P. Dirac upgraded the Pauli equation by introducing the theory of special relativity [5].

Photoelectron spectroscopy (PES) is a suitable experimental technique to study the electron spin. Hereby, the intensity of electrons with a certain energy previously excited by light with a decent energy is measured. Due to Heisenberg's principle of uncertainty and the Lorentz force acting on charged particles, the spin of the photoelectron cannot be separated by a Stern-Gerlach-Experiment [6]. Thus, a different path has to be followed, which is based on the interaction between the electron spin and matter. Beside exchange interactions with a ferromagnet the most common way is spin-orbit coupling (SOC) when the photoelectron is scattered off a high- Z material. Due to the low reflectivity of those target materials and a spin-selectivity far below 100%, the efficiency of those scattering processes is of the order of $\approx 10^{-4}$. This greatly complicates spin-resolved PES due to low count rates. Especially, when probing heterostructures, in which the investigated material is buried beneath, e.g., a capping layer or when an enhanced probing depth is needed to investigate bulk properties of a crystal, high excitation energies have to be used. These high energies—in particular when probing the valence band—result in drastically decreased photoionization cross sections, further significantly decreasing the count rates, leading to worse statistics and therefore resulting in greatly increased acquisition times. This has hampered the use of common spin detectors based on spin-orbit coupling like, e.g., a spin polarized low energy diffraction (SPLEED) detector [7] or Mott detectors [8], to be used in the hard X-ray regime for many decades. The development of two-dimensional electron detectors and the associated ability to measure a spin-selectively scattered two-dimensional electron distribution encouraged a new method of spin-filtering that utilizes an imaging spin-filter in combination with multichannel electron recording. Such a type of detector, exhibits an efficiency 10^4 times higher than the above mentioned single channel spin detectors. Beside the commonly used hemispherical deflection analyzer (HDA) for energy filtering, also the time-of-flight (TOF) scheme for energy recording can be used in combination with such an imaging spin-filter. This milestone allows for spin-resolved photoemission within the hard X-ray (spin-HAXPES) regime and therefore the bulk-sensitive investigation of electronic properties with previously

unattained efficiency. Modern multichannel electron detectors also enable momentum- or k -resolved PES, where the angle of the photoelectrons exiting the sample is measured. This allows the direct investigation of the band structure of the sample.

The focus of this thesis are complex oxide materials that exhibit a large variety of functional properties, based on the interplay of lattice, spin, charge, and orbital degrees of freedom. These properties range from superconductivity to multiferroicity, while electron correlation effects play an important role in defining these properties. In modern quantum transport, not the electron charge but its spin is increasingly coming into focus, which is the center of research in *spintronics* and—for high- Z materials with strong SOC—*spin-orbitronics*.

For the latter an interesting candidate with a strong interplay between the electron spin and its charge is KTaO_3 (KTO). This complex oxide-based material system crystallizes in a perovskite lattice with outstanding physical properties: Next to recently found superconductivity below 2 K [9], in the band insulator KTO (Ta $5d^0$ electron configuration), a surface confined quasi-two-dimensional electron system (q2DES) with Ta $5d^{0+\delta}$ configuration—based on the formation of oxygen vacancies—stabilizes at the buried interface disordered LaAlO_3 (dLAO) and KTO, and—due to the high- Z element Ta—exhibits strong SOC. This interesting q2DES is studied by angle-resolved hard X-ray photoelectron spectroscopy (HARPES). A material system considered for the use in spintronic applications, due to its predicted full spin polarization at the Fermi level,—researched by mankind for over 2500 years now—is the inverse-spinel iron oxide magnetite (Fe_3O_4). The spin polarization of magnetite in the near- E_F region has been studied by spin-resolved photoemission for about 50 years without finding any unified answer. Due to the polar nature of its surfaces they tend to reconstruct, having impact on the measured spin polarization when low excitation energies are employed. Truly bulk-sensitive measurements are needed requiring high photon energies. Therefore, the value of the spin polarization at E_F is determined by spin-HAXPES.

Outline of this thesis

At the beginning, in chapter 2, the crystal structures and electronic properties are discussed for both oxides. In addition, for magnetite, all relevant experimental and theoretical work done so far with focus on the spin polarization near E_F is reviewed. To understand k - and spin-resolved photoemission, chapter 3 covers the principles of PES, how high excitation energies can increase the information depth, and the peculiarities of the generation of synchrotron-based hard X-ray radiation. Chapter 4 deals with the quantum mechanical description of the electron spin, the origin of SOC and its effect on the differential scattering cross sections, and how this can be used for the instrumental realization of different spin detector concepts. Chapter 5 is about the technical implementation of spin-filtering in different PES setups—either based on an HDA or TOF energy recording—adapted for the hard X-ray regime. The chapters 6 and 7 show the results of the HARPES study of KTO and the spin-HAXPES study of magnetite. The achieved results of this thesis are then summarized in chapter 8.

2 Material Systems

Within this thesis two different material systems were studied by means of either k - or spin-resolved hard X-ray photoelectron spectroscopy. In this chapter both material systems are introduced and discussed regarding their crystal structure, electronic properties, and—so far applicable—magnetic properties.

2.1 Potassium Tantalate KTaO_3

Ternary metal oxides with the composition ABO_3 , with the cations A and B and the anion oxygen O , cover a wide range of interesting ground states like multiferroic insulators, magnetic semiconductors, and even superconducting metals [10, 11]. An interesting phenomenon studied in these materials is the emergence of a quasi-two-dimensional electron system (q2DES) at their heterointerfaces and surfaces [12]. The most prototypical and prominent example of such a q2DES in transition metal oxides is based on the perovskite SrTiO_3 (STO). This can mostly be ascribed to n -doping of a few top most layers and can be realised by many different ways like the local doping with impurity atoms, applying an electric field and thus accumulate negative charge, or by chemical reduction or high photon flux irradiation and therefore change of the local stoichiometry [13–16].

Such q2DESs are even more interesting when generated within more exotic high- Z elements, which in addition exhibit exceptionally large spin-orbit coupling (SOC) like Ta in the $5d$ -transition metal oxide compound KTaO_3 (KTO). This q2DES in KTO shows clear signatures of weak antilocalization at low temperatures [17] and, when combined with the ferromagnet EuO , also a hysteric magnetoresistance up to 25 K was observed [18]. These properties, as they serve as a platform for *spin-orbitronic* applications that exploit the interplay between the electron spin and its charge for future quantum transport devices [19]. The stabilization of a metallic q2DES in single crystal KTO has already been shown previously [20–22], which was mainly attributed to the formation of oxygen vacancies V_O at the topmost layers of the (001) and (111) surfaces. This fact makes the realization of a q2DES for applications quite cumbersome, since these vacancies are not stable under ambient conditions. The V_O will be refilled in air and the q2DES vanishes. To prevent this, a capping layer of several unit cells of disordered LaAlO_3 (dLAO) grown in an oxygen depleted atmosphere is introduced to act as a diffusion barrier. This layer is grown on top of KTO(001) single crystals by pulsed laser deposition (PLD) as described elsewhere [23]. The measurement of a q2DES at a buried interface by means of k -resolved photoelectron spectroscopy is elaborate since a higher information depth is required, making the use of hard X-rays inevitable.

2.1.1 Perovskite Crystal Structure

Figure 2.1 (a) shows the unit cell of an ideal cubic perovskite structure of KTO in an ionic picture: The corners of the unit cell are occupied by the A (green) and the center by a B (blue) cation. The latter is surrounded by six O^{2-} ligand anions (red), located at the face centered positions, forming an octahedron. The large variety of properties and ground states such a perovskite structure can have, depends on the combination of the different metal cations A and B, since the cation radii r define the symmetry of the unit cell. A measure for this is the so-called tolerance factor $t = (r_A + r_O)/\sqrt{2}(r_B + r_O)$ [24]. While for $t = 1$ the unit cell has a centrosymmetric perovskite structure—as shown in Fig. 2.1 (a)—, a value of greater or less than 1 forces the unit cell into a different symmetry like, e.g., orthorhombic or tetragonal. These symmetries are stabilized by, e.g., tilting and/or rotating of the oxygen octahedra often in combination with a Jahn-Teller-like distortion, or the displacement of the body-centered B cation. While in KTO the unit cell with a lattice constant of $a_{\text{KTO}} = 3.989 \text{ \AA}$ is cubic with a tolerance factor of $t_{\text{KTO}} = 1.06$ and therefore the octahedrons remain undistorted, in, e.g., YTiO_3 (YTO) due to the way smaller Y^{3+} ion radius—while the radii of Ta and Ti are quite similar—the tolerance factor is only $t_{\text{YTO}} = 0.89$ and thus YTO crystallizes in a GdFeO_3 -type distorted orthorhombic perovskite structure. This leads to a significant decrease of the B-O-B bond angle to 140° which results in a ferromagnetic ground state below $T_C = 30 \text{ K}$ [25–27].

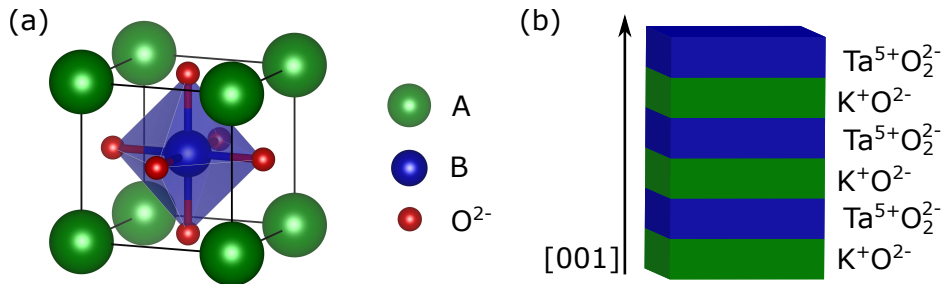


Figure 2.1: (a) Unit cell of a cubic perovskite ABO_3 with the cations A (green) and B (blue) and the oxygen anion O^{2-} (red) forming an octahedron with the B ion in the center. (b) For KTaO_3 : Alternating negatively charged $[\text{K}^+\text{O}^{2-}]^-$ and positively charged $[\text{Ta}^{5+}\text{O}_2^{2-}]^+$ layers in $[001]$ direction. Note: All lattice drawings in this thesis were made using the free software VESTA [28].

In the $[001]$ -direction the perovskite structure has an alternating AO and BO_2 stacking order, which is shown for KTO in Fig. 2.1 (b). Thereby, the K^+O^{2-} -layer is negatively charged, while the $\text{Ta}^{5+}\text{O}_2^{2-}$ -layer is positively charged and the crystal is therefore polar. This alternating charged stacking order generates a diverging electrostatic potential, which is often referred to as *polar catastrophe*, which has to be compensated at the surface in order to stabilize the crystal structure. This can be done in many different ways, e.g., by charge transfer, changes in the surface morphology, chemical doping, or structural reconstruction. In the case of KTO, the latter mechanism leads to a mixed KO/TaO_2 termination of the (001) surface, which lowers the formation energy of V_O and allows a much faster initial creation of the two-dimensional electron system [21, 29].

2.1.2 Electronic Structure

KTaO_3 in its ground state has a Ta $5d^0$ valence electron configuration and is thus a band insulator with a band gap of $E_g = 3.6 \text{ eV}$ [30]. By chemical n -doping with, e.g., Li, Ba or Ca atoms, metallicity can be introduced into KTO which results in a Ta $d^{0+\delta}$ valence state. Although for KTO it has already been shown that oxygen vacancies can be introduced by exposure to a highly intense photon beam, in this thesis only KTO substrates with a 1.6 nm disordered LAO (dLAO) capping layer were investigated. The advantage of such a dLAO/KTO heterostructure over bare KTO is that the disordered, oxygen-depleted LAO (for more information on the PLD growth see Ref. [31]) generates V_O over the entire dLAO-covered surface of the KTO substrate and not just at the irradiated sample spot, as is the case when bare KTO substrates are used. This prevents charging during the photoemission experiment because the q2DES is connected to ground via the side of the KTO substrate, where conductive silver paint is applied. The so generated V_O reduce the Ta $^{5+}$ atoms at the dLAO/KTO heterointerface to Ta $^{4+}$ and therefore Ta $5d$ carriers are accumulated on the surface of KTO and form the q2DES which grants metallicity. This spectral weight originating from Ta $5d^{0+\delta}$ carriers should be located only at the center of the BZ as is expected from the vertex of the Ta $5d$ -derived conduction bands of KTO [20, 21]. This can be understood from its conduction band structure: Due to the octahedral crystal field the orbital degeneracy of the unoccupied Ta $5d$ -orbitals is lifted as shown in Fig. 2.2 (a). This results in the d -orbitals, which exhibit a t_{2g} symmetry with respect to the $2p$ orbitals of the oxygen ligands—, i.e., d_{xy} , d_{yz} , and d_{xz} to be lowered in energy, forming a “triplet”. Those with e_g symmetry, i.e., $d_{x^2-y^2}$ and d_{z^2} , are of higher energy, forming a “doublet”. Thus, only a three band situation (t_{2g} orbitals) is considered here. Figure 2.2 (b) shows exemplarily the d_{xy} -orbitals. Due to this planar geometry, there is an orientation dependence of the hopping probability, which leads to enhanced charge fluctuations within the principal plane of the respective orbitals of adjacent B cations and thus to an effectively smaller electron mass in the $x - y$ -plane. Perpendicular to this plane (z -direction), on the other hand, a charge fluctuation is inhibited and the electron mass is therefore heavier. Due to the high- Z character of Ta, KTO also exhibits large SOC of $\Delta_{\text{SO}} = 470 \text{ meV}$. This lifts the three-fold degeneracy at the Γ -point by energetically raising one of the light bands by Δ_{SO} . At the same time, SOC strongly mixes the specific orbital character of the conduction bands in bulk KTO [20]. By generating V_O at the surface—representing a positive potential decreasing towards the bulk—the Ta $5d$ -derived bands are pulled down below the Fermi level (E_F) and, therefore, these states are populated [20]. Due to the limitation of the V_O to the surface, the motion of electrons within z -direction is constrained, which results in quantum well states (QWSs). This leads to the fact that the formed electron system is *quasi*-two-dimensional.

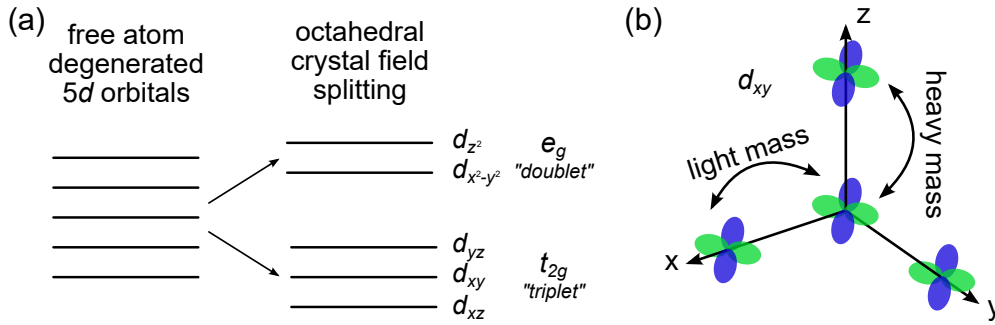


Figure 2.2: (a): Degeneracy of the 5d orbitals in a free atom and the lifted degeneracy due to the crystal field splitting in the perovskite with the two orbital symmetries e_g and t_{2g} . (b) Planar geometry of the d_{xy} -orbital: Hopping is enhanced within the $x-y$ -plane (light mass) and restrained in z -direction (heavy mass).

2.2 Magnetite Fe_3O_4

Magnetite Fe_3O_4 is the most prominent compound of a large variety of iron oxides discovered over the last three millennia like, e.g., $\alpha\text{-Fe}_2\text{O}_3$ (hematite), $\gamma\text{-Fe}_2\text{O}_3$ (maghemite), $\varepsilon\text{-Fe}_2\text{O}_3$, or wüstite (Fe_{1-x}O) [32]. The discovery of ferrimagnetism in particular has been a major driving force in research. Since the semiconductor industry is reaching the limits in continuously decreasing transistor structures, there is an urgent need for new materials and transistor types. In this respect, spintronic + spin-orbitronic is a promising way, i.e., to consider not only the electron charge but also the spin degree of freedom [33, 34].

One spintronic device in which the electron spin is used, is the Datta-Das spin transistor [35, 36]. The schematic is shown in Fig. 2.3 (a). The left spin-electrode (source) injects spin-polarized electrons (purple arrows) into the semiconducting channel (SC), which are then transported to the right spin-selective contact (drain). By applying a gate voltage and thus an effective magnetic field (blue arrows), due to SOC the electron spins start to precess while travelling from source to drain [37]. Figure 2.3 (b) shows a sketch of the electron transport between the two contacts [38]. If the spin of the precessed electron is parallel to the drain states, the electron can leave the semiconductor, thus an electric current flows and the transistor is in the *ON* state. Whereas, for the anti-parallel aligned electron spin, there are no matching states at E_F in the drain electrode leading to a high resistance and the transistor is *OFF*. An essential property of such spin-selective electrodes is a spin polarization as complete as possible at E_F , otherwise the leak current in the *OFF* state could be too high.

In such electronic devices, the conductance mismatch between the ohmic ferromagnetic metal contact and the semiconductor plays an important role [39, 40]. Although Datta and Das have proposed using Fe as a spin injector, many experiments have not shown convincing results [41–43]. Another material with a more promising conductance mismatch was found to be magnetite [44], which is predicted to have a complete, i.e., -100% , spin polarization at E_F . However, there have been many controversial discussions about the half-metallic nature of magnetite in the past. To probe its intrinsic spin polarization, several spin-resolved photoemission studies have already been carried out so far. Also from the theoretical side,

many studies have been done to further clarify this issue. Nevertheless, a unified answer has not been found. The following sections will further go into detail about the crystal and electronic structure as well as the magnetism of magnetite and will introduce the reader to the previous work done by means of theoretical calculations and modelling, as well as experimental studies using spin-resolved PES.

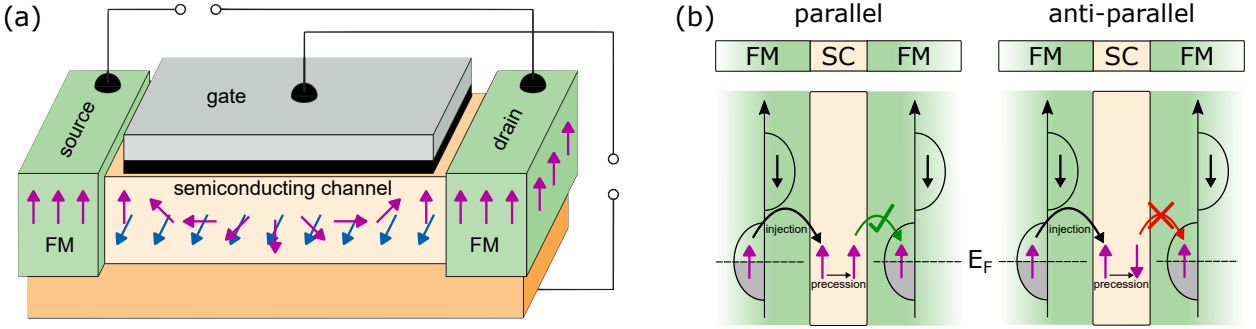


Figure 2.3: (a) Schematic view of the Datta-Das spintransistor based on the idea from S. Datta and B. Das [35]. Adapted from Ref. [36]. (b) Schematic illustration of the electron transport: (left) parallel alignment of the electron spin leads to a current of spin-up electrons at E_F into the drain electrode. (right) anti-parallel alignment leads to high resistance since transport of the spin-down electron into the spin-up state is impeded. Adapted from Ref. [38].

2.2.1 Inverse-Spinel Crystal Structure

Magnetite was one of the first minerals whose crystal structure was investigated by X-ray diffraction (XRD) [45]. In 1979 Hill *et al.* found the crystal structure to be that of an inverse-spinel (space group $Fd\bar{3}m$) at room temperature with the chemical formula Fe_3O_4 or more precisely $Fe^{2+}(Fe^{3+})_2O_4$ [46, 47], which is shown in Fig. 2.4. The slightly distorted face-centered cubic (fcc) unit cell has a lattice parameter of $a = 8.394 \text{ \AA}$ [48] and is built from 32 oxygen anions, which form an approximate cubic close-packed array. It consists of two sublattices: One denoted Fe_{tet} with 8 tetrahedrally coordinated Fe^{3+} cations (green) and the other denoted Fe_{oct} with octahedrally coordinated Fe ions with a mixed valency of 8 Fe^{2+} and 8 Fe^{3+} cations (blue) randomly distributed. Adjacent octahedra have equal edges and share a corner with the next tetrahedron. The slight distortion of the unit cell expands the tetrahedra towards their corners and leads to a weak trigonally distortion of the octahedra.

Furthermore, due to the specific stacking order of the $Fe^{2+/3+}$ cations and O^{2-} anions, the surfaces are polar, which renders them highly unstable with respect to atomic reconstruction [49–51]. This in turn affects the magnetic and electronic properties at the surface, which thus may strongly deviate from those of the bulk. In fact, the intrinsic instability of the magnetite (100) and (111) surfaces is known to result in a variety of possible metastable reconstructions [52–54]. Furthermore, the corresponding phases strongly depend on the details of the surface preparation [54], which can cause poor reproducibility in experiment.

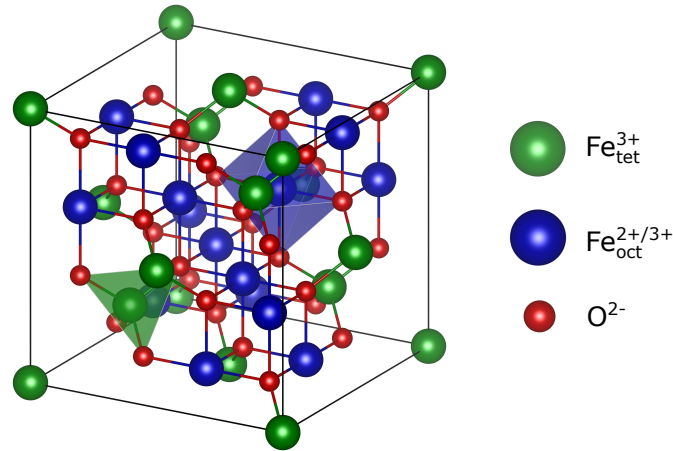


Figure 2.4: Inverse-spinel unit cell of magnetite Fe_3O_4 with the iron sublattices Fe_{tet} , consisting of only Fe^{3+} ions, and Fe_{oct} , where Fe^{2+} and Fe^{3+} ions are randomly distributed. Together with the oxygen anion iron forms tetrahedrons (green) within Fe_{tet} and octahedrons (blue) within Fe_{oct} .

2.2.2 Electronic Structure and Magnetism

The magnetic nature of magnetite is already known to humankind since 2500 years [55, 56] and it was M. L. Néel [57] who suggested the high-spin electron configuration shown in Fig. 2.5 in 1948. In this high-spin configuration, the spins of $\text{Fe}_{\text{tet}}^{3+}$ (spin-down) and $\text{Fe}_{\text{oct}}^{3+}$ (spin-up) are anti-parallel to each other, which results in a vanishing net magnetization. Since the O $2p$ valence-band states are fully occupied and therefore do not carry any magnetic moment, the total net magnetization is a result from the magnetic moments of the remaining $\text{Fe}_{\text{oct}}^{2+}$ with $4\mu_{\text{B}}$ per atom. The single minority (spin-down) electron located on the $\text{Fe}_{\text{oct}}^{2+}$ site is mobile and can hop via double exchange (DE) across the neighbouring oxygen atoms. This delocalization within the Fe-O-Fe-group is the reason for the mixed valency within the octahedral sublattice and responsible for the relatively large conductivity of magnetite in comparison with other iron oxides.

By cooling down below a temperature of $T_{\text{V}} \approx 120$ K magnetite undergoes a metal-to-insulator transition. This so-called Verwey transition is named after E. J. W. Verwey who investigated the conduction behaviour of magnetite upon cooling from room temperature down to about 50 K [58, 59]. Verwey related this transition to the ordering of Fe^{2+} cations on the Fe_{oct} sublattice, together with a charge arrangement of (001) planes, which are alternately occupied by Fe^{2+} and Fe^{3+} cations (Verwey charge ordering model) [60]. These charge ordering effects at low temperatures weaken the hopping of the electrons on the Fe_{oct} sites, decreasing the conductivity of magnetite.

Later experiments showed—beside the change in conductivity by two orders of magnitude—there is also a structural change from the cubic high-temperature phase to a monoclinic one [61, 62].

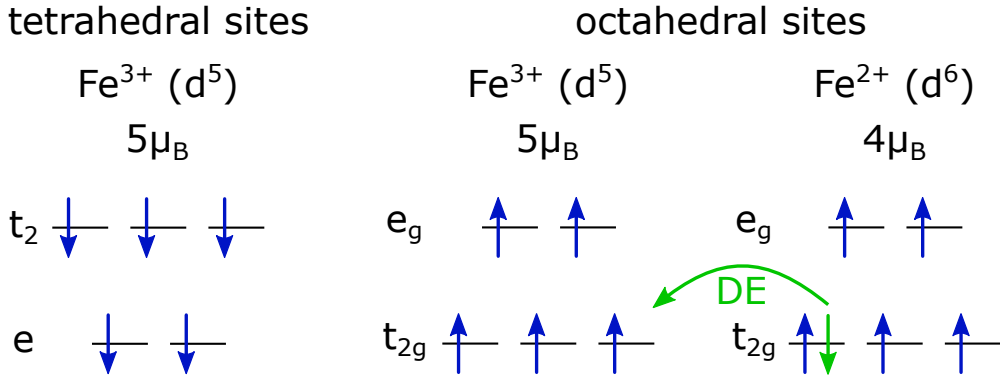


Figure 2.5: High-spin electron configuration of the tetrahedral and octahedral sublattices as suggested by Néel [57]. On both sites the Fe $3d$ states are split up by the crystal field stabilization energy Δ_{tet} and Δ_{oct} , respectively. The magnetic moments of Fe_{tet}^{3+} and Fe_{oct}^{3+} are anti-parallel to each other resulting in a net magnetization of zero. Thus, the total net magnetization of $4\mu_B$ per unit cell results from the magnetic moments of the Fe_{oct}^{2+} sublattice.

As previously mentioned, these properties of magnetite can strongly differ at the surface, due to the specific stacking order of the $Fe^{2+/3+}$ cations and O^{2-} anions in its inverse-spinel crystal structure and are only valid when assuming bulk-like Fe_3O_4 .

2.2.3 Theoretical Description of the Valence Band Spin Polarization

The possibility that the minority spin-down electrons on the Fe_{oct} sublattice give rise to a fully spin-polarized electron system at E_F triggered many theoretical investigations. Since the 1970s two different theoretical approaches have been made to predict the spin polarization of its valence band. The first one is based on density-functional theory (DFT) calculations in combination with different approximations and implementations, while the second one is especially adapted for PES and is a model calculation that describes the photoemission process from a localized electron point of view. In this chapter an overview of both theories is given and discussed.

2.2.3.1 Density-Functional Theory Calculations

In 1984 for the first time when the electronic structure of bulk magnetite was investigated by DFT [63] using the augmented plane wave (APW) method and the high-temperature (HT) cubic phase of magnetite with $Fd\bar{3}m$ symmetry. These calculations, considering magnetite from an itinerant electron point of view, indeed show only minority charge carriers at the Fermi level with a gap in the majority band and therefore predict a spin polarization P at E_F of -100% .

More and more DFT-based calculations with many different approximations and implementations have been used to further investigate magnetite, e.g., in terms of the low-temperature (LT) phase with $P2_1/c$ symmetry, correlation effects, and strain [52, 53, 63–91].

For example, Yanase and Hamada [68] applied an extended version of APW, which uses full-potential linearization in combination with the local density spin approximation (LSDA), to

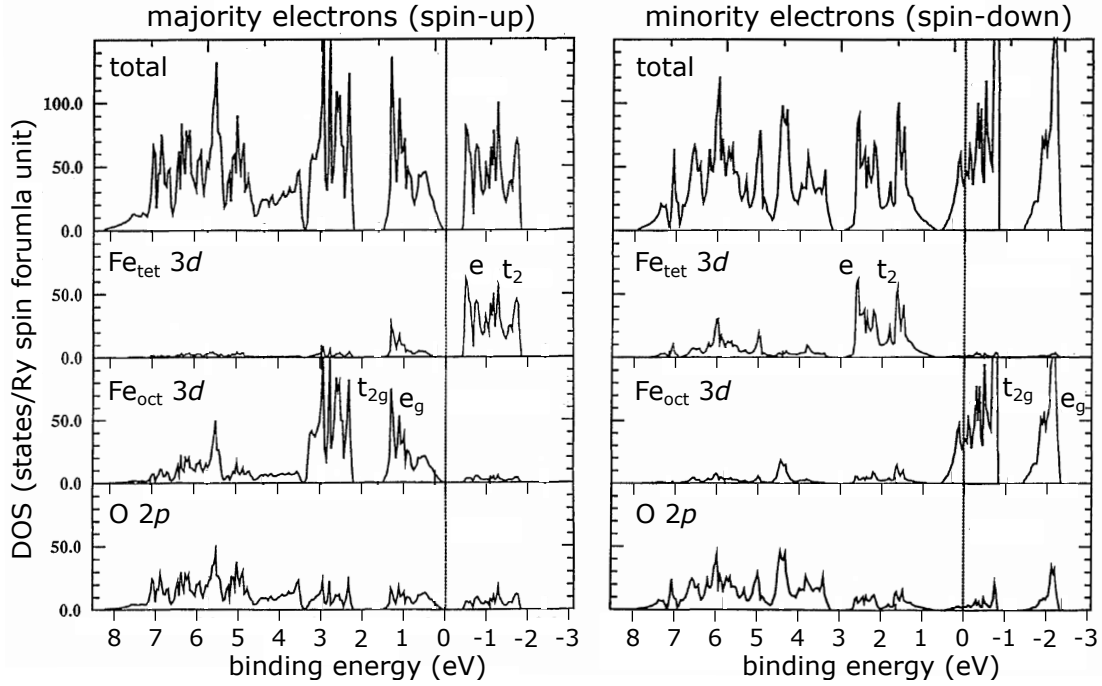


Figure 2.6: Total and site-decomposed spin-resolved DOS for magnetite calculated by means of DFT-based full-potential linearized augmented-plane-wave method with the local spin density approximation from Yanase and Hamada [68].

calculate the site-decomposed density of states (DOS) of bulk magnetite for the HT phase, which is shown in Fig. 2.6 for spin-up and spin-down electrons. In this way, the authors overcome the uncertainty of the shape of the Fermi surface and the charge density, which could not be accurately determined in the preceding calculations. The authors also conclude that there are only minority charge carriers at the Fermi level and show a gap in the majority bands. The O $2p$ subshell, which is in the range of about 3.5 to 8 eV is completely filled, while for binding energies lower than 3.5 eV the spectral weight predominantly originates from Fe $3d$ states. Due to hybridization, the region between O $2p$ and Fe $3d$ has contributions from both subshells.

Later Leonov *et al.* [75] was the first that used LSDA+U (taking correlation effects into account) in the tight-binding linear muffin-tin orbital (TBLMTO) calculation scheme together with the recently refined—using high-resolution X-ray and neutron powder diffraction data—LT crystal structure of magnetite considering long-range charge ordering [92, 93]. A very detailed study of the spin-resolved DOS (spin-DOS) of magnetite for the HT and LT phase as well as with ($U = 4$ eV) and without ($U = 0$) considering correlation effects was performed by Piekarczyk *et al.* [79] and is shown for the LT and HT phase in Fig. 2.7. When neglecting correlation effects— independently of the used structural symmetry—, magnetite is considered to be a half-metallic ferromagnet with a -100% spin polarization at E_F and a gap in the majority band of about 200 meV. For the correlated HT phase the claim of half-metallicity still holds, but due to an increase of the exchange splitting between the spin-up and spin-down states, the spin-up states of the Fe_{oct} ions and the spin-down states of the

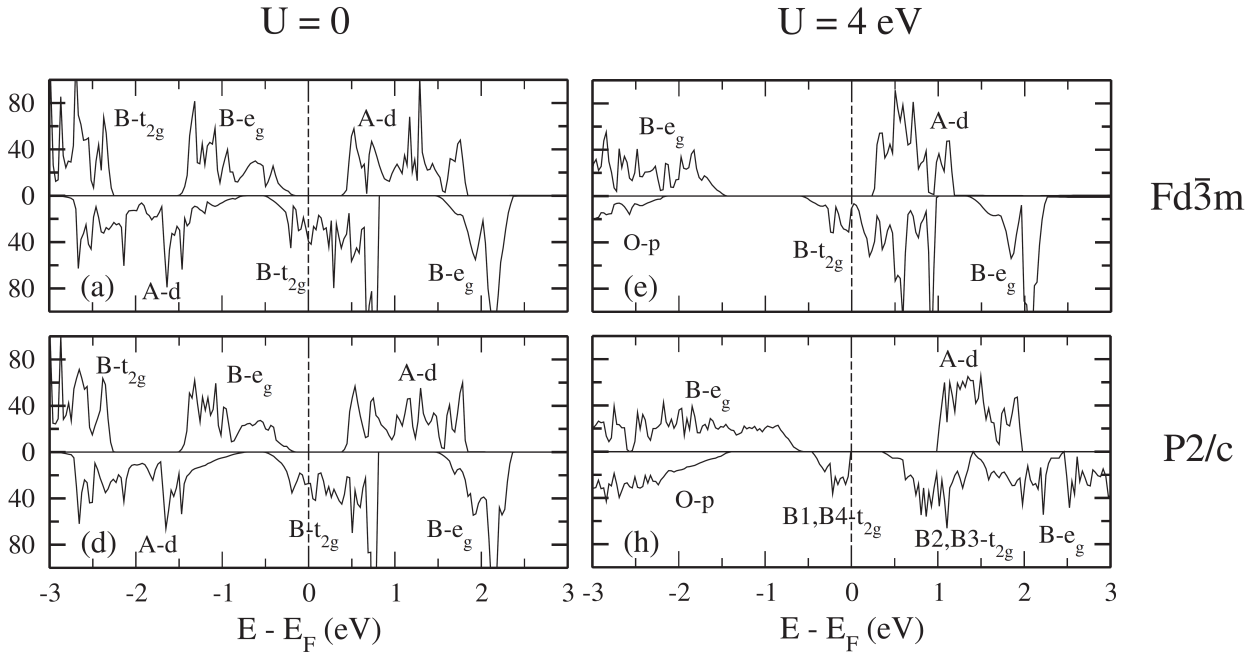


Figure 2.7: Spin-resolved DOS for magnetite calculated with GGA(+U) from Piekarz *et al.* [79] for the HT ($\text{Fd}\bar{3}\text{m}$) and LT ($\text{P}2/\text{c}$) phase without ($U = 0 \text{ eV}$) and with ($U = 4 \text{ eV}$) correlation effects taken into account. Thereby, A represents the Fe_{tet} and B the Fe_{oct} sublattice, respectively.

Fe_{tet} ions are shifted to lower energies, which leads to a drastic increase of the majority band gap to about 1.5 eV. In addition, the spectral weight of the minority t_{2g} states right above E_{F} is decreased, indicating an enhancement of electron localization due to local electron interactions [79]. Switching to the LT phase, magnetite undergoes a metal-to-insulator transition (Verwey transition) and a small gap in the minority band of about 0.18 eV opens, which is in good agreement with experimental values [94, 95]. Nevertheless, although the majority gap decreases again with respect to the correlated HT phase down to about 600 meV, the highest occupied states are still only those of minority charge carriers and therefore full spin polarization near E_{F} is preserved.

A list of further relevant DFT calculations carried out with different approximations so far is shown in the appendix in Tab. A.1 with their predicted spin polarization at the Fermi level. *All* DFT calculations predict a complete bulk spin polarization of -100% at E_{F} . It is noted that the few studies explicitly accounting for surface effects find the electrons at E_{F} only partially polarized, highlighting again that the properties of surface and bulk strongly differ in magnetite.

However, one should bear in mind that the Verwey transition may not be adequately captured by DFT calculations since correlations are treated only statically on a mean-field level. Furthermore, only ground state properties are considered in DFT instead of the photoemission process itself.

2.2.3.2 Model of Photoemission from Localized Fe 3d States

In 1978 Alvarado and Bagus [96] came up with a model calculation that considers the photoemission process for ferrites from a localized 3d shell in a magnetically ordered state at $T = 0$ K. In their model they assume that the spin of the total system S , which consists of the final state spin of the $3d^{n-1}$ system left behind S_z^f —magnetic ordering in z -direction assumed—and the spin of the photoelectron $s = 1/2$, is conserved. Therefore, $S^i = S_z^i \equiv S$ applies, with S^i denoting the spin of the initial $3d^n$ electron system. This spin conservation leads S_z^f to take two different values:

$$S_z^f = S_z + 1/2 \quad \text{and} \quad S_z^f = S_z - 1/2, \quad (2.1)$$

where the first term describes the emission of a minority (spin-down) electron and the latter the emission of a majority (spin-up) electron. For a high-spin system with a half or less than half-filled 3d shell ($n \leq 5$), only the emission of majority electrons has to be considered and the polarization of the photoelectrons in this case is clearly +100%. But for magnetite with a more than half-filled initial system with $3d^6$ configuration, also the emission of minority electrons has to be taken into account. The corresponding emission processes are illustrated in Fig. 2.8, where the wavefunction of the emitted minority and majority photoelectrons are denoted with ψ_A and ψ_B , respectively.

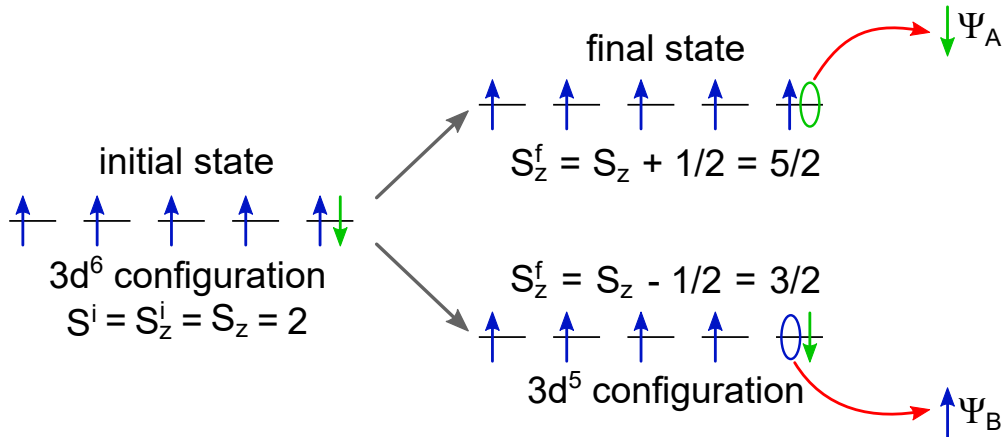


Figure 2.8: Illustration of the model of the photoemission process from a localized Fe^{2+} $3d^6$ shell under the conservation of the spin of the total system S_z [96]. An initial state with spin S_z^i results in two different final states with spin S_z^f depending on whether a minority (spin-down, ψ_A) or majority (spin-up, ψ_B) electron is emitted.

For this $3d^6$ configuration the final wavefunction Ψ_f is a superposition of $3d^{n-1}$ ion states with both of the values for S_z^f :

$$\begin{aligned}\psi_f(S, S_z) &= |2, 2\rangle \\ &= A\psi_A + B\psi_B \\ &= A|S + \frac{1}{2}, S + \frac{1}{2}\rangle|\frac{1}{2}, -\frac{1}{2}\rangle + B|S + \frac{1}{2}, S - \frac{1}{2}\rangle|\frac{1}{2}, \frac{1}{2}\rangle \\ &= A|\frac{5}{2}, \frac{5}{2}\rangle|\frac{1}{2}, -\frac{1}{2}\rangle + B|\frac{5}{2}, \frac{3}{2}\rangle|\frac{1}{2}, \frac{1}{2}\rangle.\end{aligned}\tag{2.2}$$

From the condition that the d^{n-1} ion and the photoelectron couple together to form the eigenfunction of S^2 , i.e., $S^2\psi = S(S+1)\psi$, one can obtain the mixing coefficients A and B by using a step-up operator [97], leading to:

$$A = \sqrt{\frac{5}{6}} \quad \text{and} \quad B = \sqrt{\frac{1}{6}}\tag{2.3}$$

and it follows for the polarization P of the photoelectrons of the Fe^{2+} $3d$ shell:

$$P = \frac{B^2 - A^2}{A^2 + B^2} = -\frac{2}{3} = -66.7\%.\tag{2.4}$$

Like the DFT calculations, also this model predicts the polarization to be negative and thus, that the emission is predominantly that of minority electrons. Nevertheless, it does not provide a specific value for the spin polarization directly at E_F , but of the whole Fe^{2+} $3d$ shell. While for a d^6 configuration the polarization of this shell is -66.7% , this value would decrease in magnitude for bigger n , e.g., for a d^9 system the polarization P has a value of only -33% .

2.2.4 Previous Experimental Studies

Since the first spin-resolved PES study on the band structure of natural single crystals (nsc) of magnetite in the 1970s [98], there have been many further attempts to determine the spin polarization. Depending on the type of samples—single crystals and thin films prepared by different deposition techniques—and, specifically, surface orientation and preparation, values for the spin polarization at E_F ranging from $+30\%$ to -80% have been reported over the past 40 years (see Table 2.1) [84, 98–109].

Generally, this surprisingly large scatter of values is rooted in the fact that previous photoemission studies employed low excitation energies in the range from several 10 to several 100 eV, resulting in a rather low probing depth of a few atomic layers only (see Sec. 3.3). In some cases, photon energies below 10 eV were used, but due to the lack of systematic data it is unclear whether, concomitantly, the probing depth is enhanced, as was shown for some selected materials [110, 111].

A low probing depth, however, hampers the interpretation of the spin polarization data in the case of magnetite due to surface effects as described in Sec. 2.2.1 and it is thus not surprising that photoemission has provided a broad range of spin polarization values, with

Table 2.1: Overview of the measured spin polarizations P at E_F from previous spin-resolved photoemission studies

Authors	Sample	Method of sample /surface preparation	$h\nu$ (eV)	P (%)
Kay <i>et al.</i> [99]	Fe ₃ O ₄ (n/a)	reactive sputter deposition	4.5	+30
Kim <i>et al.</i> [100]	Fe ₃ O ₄ (111)	oxidation of Fe films grown on W	40	+16
Alvarado <i>et al.</i> [98]	Fe ₃ O ₄ nsc	cleaved single crystal	4.5	-35
Morton <i>et al.</i> [101]	Fe ₃ O ₄ (100)	reactive DC sputtering	160	-40
Vescovo <i>et al.</i> [102]	Fe ₃ O ₄ (100)	plasma-assisted MBE	40	-50
Fonin <i>et al.</i> [103-105]	Fe ₃ O ₄ (100)	MBE	58	-55
Huang <i>et al.</i> [106]	Fe ₃ O ₄ (100)	MBE	450	-55.5
Alvarado <i>et al.</i> [107]	Fe ₃ O ₄ nsc	cleaved single crystal	5.2	-65
Tobin <i>et al.</i> [108]	Fe ₃ O ₄ (100)	reactive DC sputtering	160	-65
Wang <i>et al.</i> [84]	Fe ₃ O ₄ (100)	epitaxial grown on MgO(001)	4.65	-72
Dedkov <i>et al.</i> [109]	Fe ₃ O ₄ (111)	oxidation of Fe films grown on W	21.2	-80
Fonin <i>et al.</i> [103, 105]	Fe ₃ O ₄ (111)	oxidation of Fe films grown on W	21.2	-80

a reliable experimental determination of the true intrinsic bulk value still lacking.

To settle the issue of the intrinsic spin polarization of magnetite, truly bulk-sensitive spin-resolved photoemission has to be performed to rule out any surface effects. Previous spin- and angle-integrated measurements of the valence band showed still significant differences in the spectra for the (111) and (100) surface orientations at photon energies as high as ≈ 700 eV [95]. Therefore, to really probe bulk properties, photon energies in the hard X-ray regime have to be used. This was prevented previously by the notoriously low photoionization cross sections in the hard X-ray regime (see also Sec. 3.3) in combination with the poor efficiency for Mott scattering (see also Sec. 4.4.1), which for a long time was the basic design principle of photoemission spin detectors. Therefore, new routes have to be followed to enable bulk-sensitive, spin-resolved photoemission experiments.

2.3 Summary

Potassium tantalate Although KTO is a band insulator, the positive charge of oxygen vacancies at the buried interface of LAO/KTO introduces metallicity by pulling the Ta $5d$ -derived bands below E_F and populating them with the two electrons released per oxygen vacancy. Due to the decrease of this potential towards the bulk, the motion of the electrons is constrained within a *finite* depth. Therefore, the formed electron system at the dLAO/KTO interface can be seen as *quasi*-two-dimensional.

Magnetite The complexity of the unit cell of magnetite in combination with the structural changes when undergoing the Verwey transition, results in changes in the conductivity of several orders of magnitude, and the presence of correlation effects within the Fe $3d$ shell make Fe_3O_4 a challenging candidate when it comes to theoretical calculations based on DFT. Several calculations using a large variety of approximations and implementations predict a spin polarization at E_F of -100% although they slightly differ regarding the fine structure of the O $2p$ and Fe $3d$ states. Nevertheless, the question is whether DFT is suitable for such strongly correlated electron systems and capable of—due to the calculation of ground states—the correct prediction of the photoemission process.

The different approach from Alvarado and Bagus therefore does not make a prediction of the spin polarization directly at E_F , but of the whole Fe^{2+} shell with a value of -66.7% by considering the emission of photoelectrons from localized $3d$ states. But clearly, this theory completely neglects band structure effects.

Also from the experimental side no unified answer has yet been given for the true bulk spin polarization of magnetite due to the low excitation energies used in these studies resulting in a broad variety of polarization values at E_F .

To investigate both, the buried q2DES at the heterointerface of LAO/KTO and the bulk spin polarization of magnetite in the near- E_F region, k - and spin-resolved *hard X-ray* photoemission has to be used to make a valuable and meaningful contribution to each subject. In the following chapters, the principles of the photoemission process are discussed especially regarding the need and generation of hard X-ray radiation together with the basics of spin-resolved photoemission and its different technical instrumentation as well as its development over the past decades.

3 Principles of Photoemission

Photoelectron spectroscopy is one of the most versatile and widely used analytical techniques to investigate the occupied part of the electronic structure of materials in solid state physics and material science. Based on the photoelectric effect, which was discovered in 1887 by H. Hertz [112], it utilizes the fact that electrons are emitted from a solid upon irradiation with light. Einstein later explained this effect with the quantized nature of light [113]. From the 1950's on K. Siegbahn worked on the development of the first high-resolution photoelectron spectrometer allowing for the measurement of the kinetic energies of strongly bound electrons by using light in the X-ray regime. Under the progress of the last decades this technique, formerly known as electron spectroscopy for chemical analysis (ESCA), has been extended not only to determine the chemical and electronic structure of materials regarding their core levels, but also to map the electronic dispersions in the valence band, which is known as angle-resolved photoelectron spectroscopy (ARPES). One of the most elaborate PES techniques is to measure the valence band spin-resolved, giving the possibility to discriminate the electrons regarding their spin state.

In this section, the most relevant concepts of PES are introduced based on several reviews and textbooks [111, 114, 115] with special focus on the role of the excitation energy on the photoemission process and the generation and work with synchrotron-based hard X-ray radiation.

3.1 Energetics and Kinematics

The principle of photoemission is shown in Fig. 3.1 (a). A monochromatized photon beam with the energy $h\nu$ impinges on the sample with an angle of incidence Ψ with respect to the surface normal. When the energy of the photons is high enough, the excited electrons can escape the sample with their kinetic energy E_{kin} and are collected and detected by the analyzer and the detector, which are described in more detail in chapter 5. From the kinetic energy and the corresponding intensity of the photoelectrons, a photoemission spectrum is obtained, which is shown schematically in Fig. 3.1 (b). Thereby, the equation which relates the photon energy $h\nu$ and the kinetic energy of the photoelectrons to the binding energy E_{B} of the electrons in the sample is:

$$E_{\text{kin}} = h\nu - |E_{\text{B}}| - \phi, \quad (3.1)$$

where ϕ is the work function and represents the energy which is needed to lift the photoelectron from the Fermi level E_{F} up to the vacuum level. Due to the experimental resolution (Gaussian broadening) and the finite lifetime of the core hole left behind when the electron

is ejected (Lorentzian broadening), the core levels are shown as Voigt-like peaks with the center at the respective binding energy. From such a spectrum, one can infer the electronic and chemical structure, e.g., the oxidation states of the various chemical elements that make up the probed sample. In addition to the broadening, the valence band is cut off by the Fermi distribution at E_F .

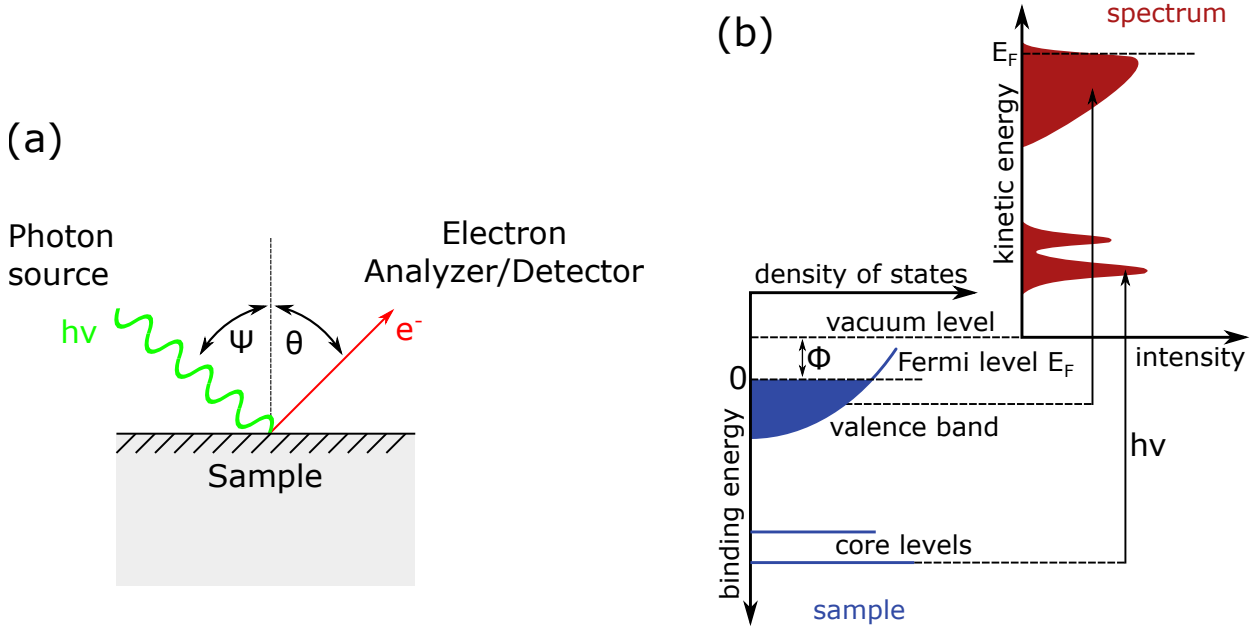


Figure 3.1: (a) Principle of the photon-in electron-out process of photoelectron spectroscopy with the incident angle Ψ and the emission angle θ . (b) Experimentally obtained spectrum reflecting the density of states of the probed sample. Adapted from Ref. [114].

When probing—beside energy and intensity—the emission angle θ of the photoelectrons, one can further investigate the momentum-resolved electronic structure and thus directly probe the dispersion of the valence states. Let \mathbf{K}_f denote the momentum of the photoelectrons in vacuum, $\mathbf{k}_{h\nu}$ the momentum of the absorbed photon, \mathbf{k}_i the momentum of the electron in the initial state and \mathbf{k}_f in the final state within the solid, then due to momentum conservation one can unite the components parallel and perpendicular to the surface with \mathbf{G} being a reciprocal lattice vector (see Fig. 3.2 (a)):

$$k_{f\parallel} = k_{i\parallel} + G_{\parallel} + k_{h\nu\parallel}, \quad (3.2)$$

$$k_{f\perp} = k_{i\perp} + G_{\perp} - k_{h\nu\perp}. \quad (3.3)$$

For low photon energies the contribution of the photon momentum $\mathbf{k}_{h\nu}$ is often neglected. But in this study, mainly high photon energies within the hard X-ray regime are used and thus the photon momentum must be taken into account. Since translational symmetry is preserved parallel to the surface, also the momentum parallel to the surface is conserved during the transition of the photoelectron from the solid to vacuum and $K_{f\parallel} = k_{f\parallel}$ holds. Therefore, the relations between the emission angle θ and the kinetic energy of the photo-

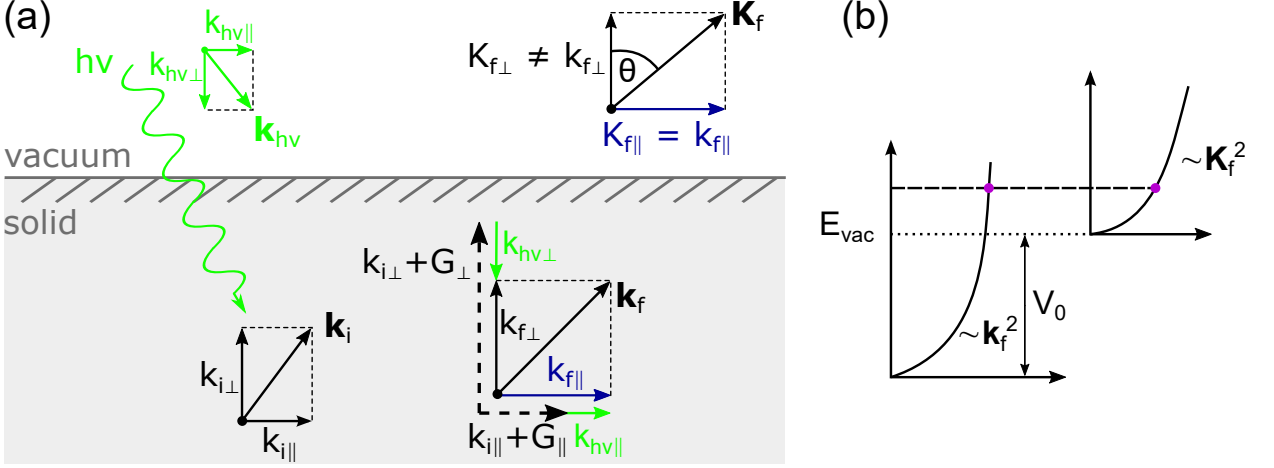


Figure 3.2: (a) Schematic picture of the momentum conservation in the photoemission process, with the photon momentum $\mathbf{k}_{h\nu}$, the electron momentum \mathbf{k}_i in the initial state, the momentum \mathbf{k}_f of the excited photoelectron within the solid, a reciprocal lattice vector \mathbf{G} , and the final electron momentum \mathbf{K}_f in vacuum. (b) Determination of $k_{f\perp}$ assuming an electron free-like final state. Figures adapted from Refs. [111, 116].

electron can be written as [115]:

$$k_{f\parallel} = K_{f\parallel} = \frac{\sqrt{2m_e E_{\text{kin}}}}{\hbar} \sin \theta, \quad (3.4)$$

with the electron mass m_e and the reduced Planck's constant \hbar . In turn, since the translational symmetry is broken perpendicular to the surface, the electron momentum component in this direction, $k_{f\perp}$, is not conserved and therefore $K_{f\perp} \neq k_{f\perp}$, which hampers the determination of $k_{f\perp}$. By assuming a nearly-free-electron like dispersion $E_{k_f} \sim k_f^2$ of the final states, with the vertex of the free-electron parabola located at an energy V_0 —the so-called *inner potential* (see also Fig. 3.2 (b))—below the vacuum level, $k_{f\perp}$ can be expressed by [115]:

$$k_{f\perp} = \frac{\sqrt{2m_e(E_{\text{kin}} \cos^2 \theta + V_0)}}{\hbar}. \quad (3.5)$$

The inner potential V_0 is often treated as an empirical parameter and is being determined from experimental data. The influence of the photon momentum in experiments is further discussed in Sec. 5.2.2 using the example of valence-band mapping of Re(0001) by means of hard X-ray ARPES (HARPES).

3.2 Many Body Description

Having shown within a single-particle picture that energy and momentum conservation links a measured spectrum to the initial state properties, the many-body description of the photoemission process will now be considered. The photocurrent results from the excitation of electrons from the N -electron ground state $|i\rangle$ defined by the wave function Ψ_i^N to a final

state $\langle f|$ with the wave function Ψ_f^N . The transition rate $\omega_{i \rightarrow f}$ of such an excitation can be expressed by using Fermi's Golden Rule [111, 114, 117]:

$$\omega_{i \rightarrow f} = \frac{2\pi}{\hbar} |\langle \Psi_f^N | \mathcal{H}_{per} | \Psi_i^N \rangle|^2 \delta(E_f^N - E_i^N - h\nu), \quad (3.6)$$

where E_i^N and E_f^N denote the energies of the initial and final N -electron states, and \mathcal{H}_{per} is the Hamilton operator describing the small perturbation resulting from the electromagnetic field of the impinging photons. This perturbation can be expressed with the vector potential $\mathbf{A}(\mathbf{r}_i)$ by the canonical replacement of the momentum $\mathbf{p}_i \rightarrow \mathbf{p}_i - e\mathbf{A}(\mathbf{r}_i)$, and after separating the unperturbed part one gets:

$$\mathcal{H}_{per} = -\frac{e}{2m_e} (\mathbf{A}(\mathbf{r}_i) \cdot \mathbf{p}_i + \mathbf{p}_i \cdot \mathbf{A}(\mathbf{r}_i)) + \frac{e^2}{2m_e} \mathbf{A}(\mathbf{r}_i)^2, \quad (3.7)$$

with the momentum operator $\mathbf{p}_i = i\hbar\nabla$. Using the commutation rules the terms in brackets can be expressed as $2\mathbf{A}(\mathbf{r}_i) \cdot \mathbf{p}_i + i\hbar(\nabla \cdot \mathbf{A}(\mathbf{r}_i))$. Since every single electron—numbered with i —interacts with the electromagnetic field, one has to sum over all electrons with their momentum \mathbf{p}_i and position operator \mathbf{r}_i . When neglecting two photon processes and therefore the $\mathbf{A}(\mathbf{r}_i)^2$ -term, and using the translation invariance within the solid, i.e., neglecting surface effects, which gives $\text{div } \mathbf{A}(\mathbf{r}_i) = \nabla \cdot \mathbf{A}(\mathbf{r}_i) = 0$, one gets:

$$\mathcal{H}_{per} = \frac{e}{m_e} \sum_{i=1}^N \mathbf{A}(\mathbf{r}_i) \cdot \mathbf{p}_i. \quad (3.8)$$

The second quantization formalism introduces the operator $c_{\mathbf{k}}$, which annihilates an electron in the Bloch state $|\phi_{\kappa\mathbf{k}}\rangle$ with momentum \mathbf{k} and band index κ , and the operator $c_{\mathbf{k}_f}^\dagger$ generating an electron in the final Bloch state $|\phi_{\kappa_f\mathbf{k}_f}\rangle$ with momentum \mathbf{k}_f and band index κ_f . The perturbation operator can then be written as:

$$\mathcal{H}_{per} = \sum_{\mathbf{k}_f, \mathbf{k}} \langle \mathbf{k}_f | \mathcal{H}_{per} | \mathbf{k} \rangle c_{\mathbf{k}_f}^\dagger c_{\mathbf{k}} = \sum_{\mathbf{k}_f, \mathbf{k}} M_{\mathbf{k}_f\mathbf{k}} c_{\mathbf{k}_f}^\dagger c_{\mathbf{k}}, \quad (3.9)$$

where $M_{\mathbf{k}_f\mathbf{k}}$ is the single-electron matrix element in which the momentum conservation is encoded, while the energy conservation is granted by the δ -function in Eq. 3.6. Another simplification step can be done by applying the so-called *sudden approximation*, which neglects the interaction of the photoelectron with the remaining $(N-1)$ -electron system after the photoexcitation. This is all the more the case for high energetic electrons resulting from the use of hard X-ray radiation in this study [118]. Thus, the final state can be approximated and described as:

$$|\Psi_f^N\rangle = c_{\mathbf{k}_f}^\dagger |\Psi_f^{N-1}\rangle, \quad (3.10)$$

with the photoelectron in the state \mathbf{k}_f and the remaining $(N-1)$ -electron system $|\Psi_f^{N-1}\rangle$. The energy of the finale state E_f^N can then be separated into the energy of the $(N-1)$ -electron system E_f^{N-1} and the kinetic energy of the photoelectron E_{kin} .

This inserted in Eq. 3.6 leads to:

$$\omega_{i \rightarrow f} = \frac{2\pi}{\hbar} |\langle \Psi_f^{N-1} | c_{\mathbf{k}_f} \sum_{\mathbf{k}'_f, \mathbf{k}} M_{\mathbf{k}'_f \mathbf{k}} c_{\mathbf{k}'_f}^\dagger c_{\mathbf{k}} | \Psi_i^N \rangle|^2 \delta(E_{\text{kin}} + E_f^{N-1} - E_i^N - h\nu), \quad (3.11)$$

which can be simplified by applying momentum conservation and operator algebra:

$$\omega_{i \rightarrow f} = \frac{2\pi}{\hbar} \left| \sum_{\mathbf{k}} M_{\mathbf{k}_f \mathbf{k}} \langle \Psi_f^{N-1} | c_{\mathbf{k}} | \Psi_i^N \rangle \right|^2 \delta(E_{\text{kin}} + E_f^{N-1} - E_i^N - h\nu), \quad (3.12)$$

with the sum $\sum_{\mathbf{k}}$ running over the entire Brillouin zone. By summing up over all final states f one gets the photoemission intensity $I(\mathbf{k}_f, \varepsilon)$:

$$I(\mathbf{k}_f, \varepsilon) \propto \sum_{\mathbf{k}} |M_{\mathbf{k}_f \mathbf{k}}|^2 \underbrace{\sum_f |\langle \Psi_f^{N-1} | c_{\mathbf{k}} | \Psi_i^N \rangle|^2 \delta(\varepsilon + E_f^{N-1} - E_i^N)}_{A^<(\mathbf{k}, \varepsilon)}, \quad (3.13)$$

where $A^<(\mathbf{k}, \varepsilon)$ is the single-electron spectral removal function with $\varepsilon = E_{\text{kin}} - h\nu$, which is directly measured by PES and describes the probability of removing an electron with momentum \mathbf{k} and energy ε from the initial state $|\Psi_i^N\rangle$. While the removal function takes many body effects into account, including shifts and broadening of the photoemission lines, the single-electron matrix element $M_{\mathbf{k}_f \mathbf{k}}$ considers the excitation process like the photon momentum $\mathbf{k}_{h\nu}$, polarization, photoelectron final state $|\phi_{\kappa_f \mathbf{k}_f}\rangle$, and also the experimental geometry.

3.3 The Role of Excitation Energy

After the photoexcitation, while propagating to the surface, the photoelectron might scatter inelastically, e.g., by the excitation of plasmons or phonons. As a result, the initial intensity of the photoemission process I_0 undergoes a Beer-Lambert-like damping ending up with the intensity of the photoelectrons at the surface of the sample $I(z)$ being:

$$I(z) = I_0 \exp\left(-\frac{z}{\lambda_{\text{IMFP}} \cos \theta}\right), \quad (3.14)$$

where z denotes the distance from the emitting atom to the sample surface, λ_{IMFP} the inelastic mean free path (IMFP) of the photoelectrons and θ the detection angle (see Fig. 3.1 (a)). The term $\lambda_{\text{IMFP}} \cos \theta$ is often defined as the effective IMFP λ_{eff} . In Fig. 3.3 (a) the IMFP for many different materials is shown as a function of E_{kin} (black dots) together with a dashed line as a guide to the eye often referred to as *universal curve*. Above 50 eV the predominant scattering mechanism is the excitation of plasmons which depends on the density of the valence electrons, which is similar for many different materials.

In this energy range up to several keV, a well-established approximation for λ_{IMFP} is the semi-empirical TPP-2M formula proposed by Tanuma, Powell, and Penn [119–121]:

$$\lambda_{\text{IMFP}} = \frac{E_{\text{kin}}}{E_{\text{P}}^2 [\beta \ln(\gamma E_{\text{kin}}) - (C/E_{\text{kin}}) + (D/E_{\text{kin}}^2)]} [\text{\AA}], \quad (3.15)$$

with the plasmon energy $E_{\text{P}} = 28.8(N_{\text{v}}\rho/M)^{1/2}$, where N_{v} denotes the number of valence electrons, ρ the density, and M the molar mass. From these quantities, together with the energy of the band gap E_{g} , the material-specific parameters β , γ , C , and D are calculated. Figure 3.3 (a) also shows λ_{IMFP} calculated with Eq. 3.15 for Fe_3O_4 , KTaO_3 , and LaAlO_3 between 60 eV and 10 keV.

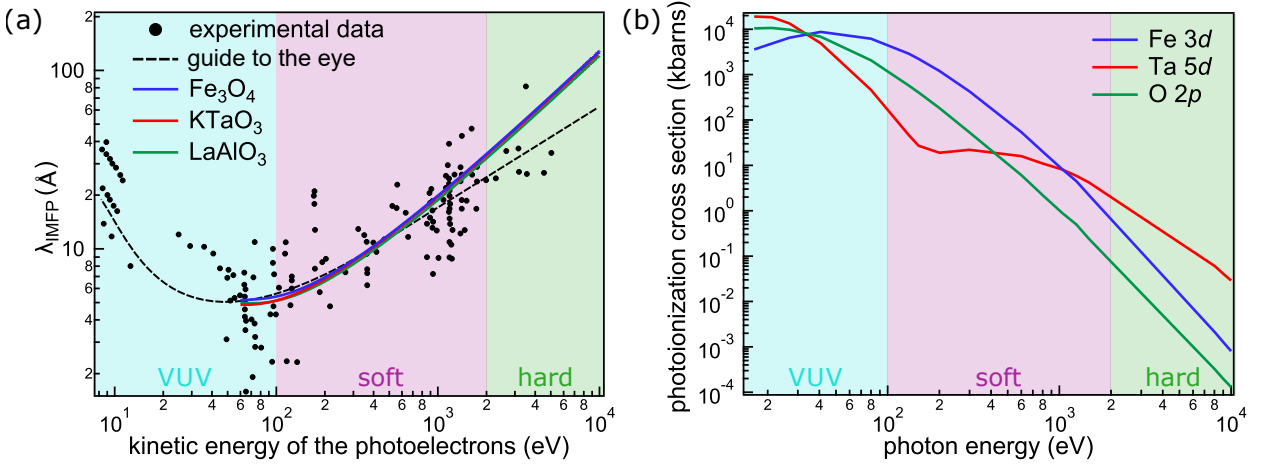


Figure 3.3: (a) Inelastic mean free path λ_{IMFP} of electrons as a function of kinetic energy calculated with Eq. 3.15 for Fe_3O_4 , KTaO_3 , and LaAlO_3 . The *universal curve* is shown as dashed line. Experimental data adopted from Ref. [122]. (b) Photoionization cross sections for Fe 3d, Ta 5d, and O 2p as a function of photon energy. Data adopted from Ref. [123, 124].

It is clearly deducible that λ_{IMFP} strongly depends on the kinetic energy E_{kin} and thus also on the used photon energy $h\nu$. For weakly bound valence electrons $E_{\text{kin}} \approx h\nu$ applies. Therefore, higher photon energies allow more electrons from deeper in the sample to reach its surface, escape into the vacuum, and be detected. Thus, for bulk-sensitive measurements and the study of buried heterostructures *high photon energies* are needed. The region above 2 keV is often referred to as the *hard X-ray* regime, in which the spin- and k -resolved data in this study were acquired. Lower photon energies in the range of several 100 eV are denoted as *soft X-ray* and even lower energies of only a few 10 eV as vacuum ultraviolet (VUV) radiation.

In contrast to the gain of information depth while using hard X-rays, the photoionization cross sections depicted in Fig. 3.3 (b) strongly decrease by several orders of magnitude as exemplarily shown for the Fe 3d, Ta 5d, and O 2p core levels. This results not only in a tremendous loss in count rate and a concomitant increase in acquisition time, but also in a change of the lineshape of a photoemission spectrum, especially when the cross sections of hybridized states, e.g., O 2p and Fe 3d, change differently relative to each other.

Another important issue when using hard X-rays which has to be considered—especially when performing HARPES—is the increasing influence of phonon effects. At high photon energies, the temperature dependent creation and annihilation of phonons during the photoexcitation process is no longer negligible as is the case at low excitation energies. The measured intensity in HARPES can be separated into two components [125, 126]:

$$I(h\nu, T) = I_{\text{DT}}(h\nu, T) + I_{\text{NDT}}(h\nu, T), \quad (3.16)$$

with I_{DT} being the emitted intensity for the k -conserving direct transitions (DTs), suitable for the recording of the sample's bandstructure, while the intensity I_{NDT} of the non-direct transitions (NDTs) includes additional vibrational lattice excitations, smearing out momentum information and therefore the k -resolution of the experiment.

The energy- and temperature-dependence of I_{DT} can be described in a thermal disorder model by the Debye-Waller factor $DW(T)$ [127]:

$$DW(T) = \exp\left(-\frac{1}{3}|\mathbf{G}|^2\langle U^2(T)\rangle\right). \quad (3.17)$$

Thereby \mathbf{G} represents the reciprocal lattice vector—being large in HARPES experiments—and the $\langle U^2(T)\rangle$ -term represents the vibrational mean-squared atomic displacement at a given temperature T . The latter can be expressed by $\langle U^2(T)\rangle = T(3h^2/M_a k_B \theta_D^2)$ with the atomic mass M_a , the Boltzmann constant k_B , and the material-specific Debye-temperature θ_D [128]. I_{NDT} scales inversely to I_{DT} and—although a more complex relation has been suggested [126, 129]—in a first order approximation can be estimated to scale as $\sim [1 - DW(T)]$ [125].

Therefore, to keep $DW(T)$ high in order to maintain a high proportion of DTs, $\langle U^2(T)\rangle$ should be kept small. Thus, HARPES measurements are often conducted at cryogenic temperatures and on samples with relative stiff lattices, i.e., for large atomic masses (high- Z) and high Debye-temperatures. As a consequence, this technique has so far only been applied to a few prototypical material systems like, e.g., W and $\text{Ga}_{1-x}\text{Mn}_x\text{As}$ [128, 130], $\text{Ga}_{1-x}\text{Mn}_x\text{P}$ [131], Mo and TiTe_2 [132], and LaB_6 [133]. Since Ta in KTO is also a high- Z element, the investigation of the Ta-based buried q2DES at the interface of LAO/KTO might also be a suitable candidate for HARPES experiment, which will be further discussed in chapter 6.

To summarize, for bulk-sensitive angle-resolved photoemission high excitation energies—granting an extended information depth—are needed, which also introduce some obstacles limiting the feasibility of resolving valence-band structures in HARPES experiments. Especially, high energy resolution as well as spectrometers with—a high DW assumed—high k -resolution and—considering the dropping absorption cross sections—radiation sources with high photon flux are needed.

3.4 Synchrotron-based Hard X-ray Radiation

While vacuum ultraviolet and soft X-ray radiation—with a fixed photon energy—can be generated easily by state-of-the-art laboratory-based sources like gas-discharge lamps, lasers or X-ray guns, the generation of hard X-ray radiation is much more elaborate. Although liquid gallium-based sources with a fixed photon energy of 9.25 keV are available in the meantime [134], the most common way for the generation of energy-variable hard X-ray radiation is the use of a synchrotron facility, which will be discussed in this section.

Figure 3.4 (a) shows the schematic structure of the electron synchrotron PETRA III (DESY, Hamburg) from the generation until the experimental hutch P22, at which all k - and spin-resolved photoemission data shown in this thesis were acquired.

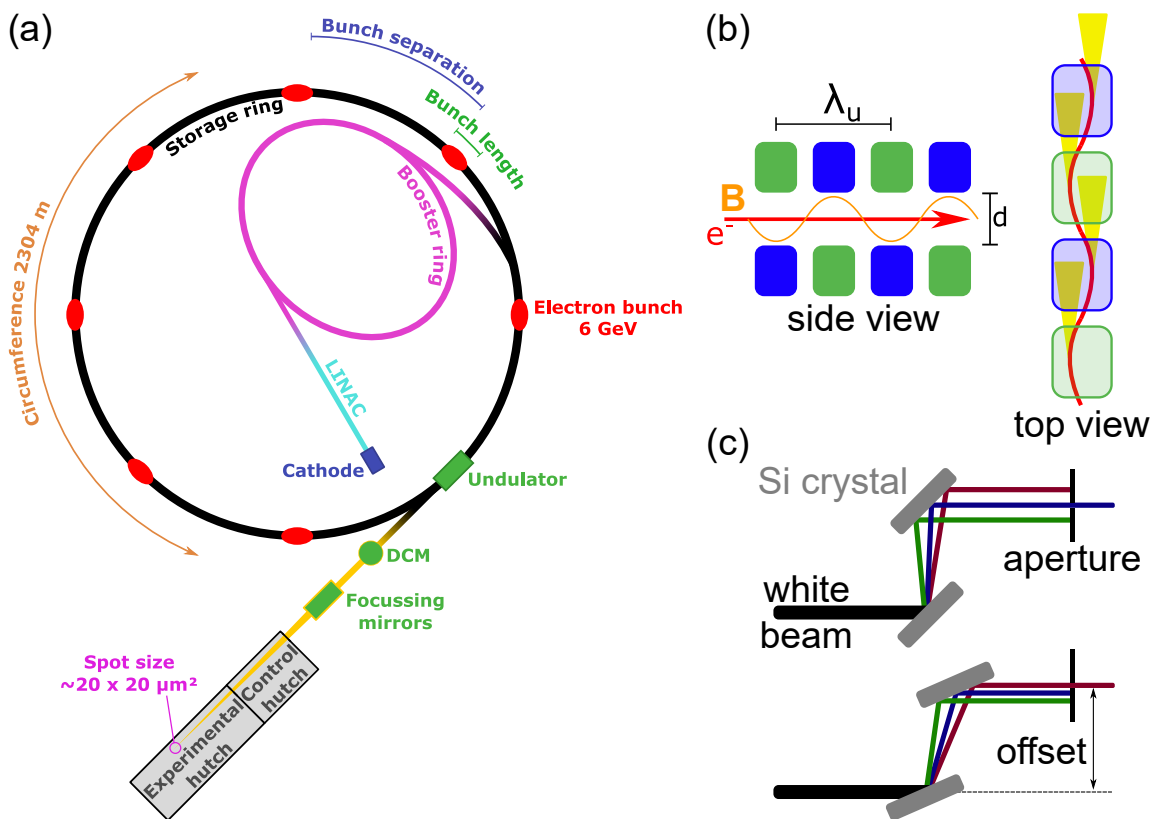


Figure 3.4: (a) Schematic design of the electron synchrotron PETRA III (DESY, Hamburg): The cathode generates electrons, which are separated in multiple packages or bunches while being accelerated to 100 MeV within the LINAC and later up to 6 GeV within the booster ring before finally injected into the storage ring. While orbiting electromagnetic radiation is generated within the undulators and monochromatized with the double crystal monochromator (DCM) before being focused with the mirrors. (b) Working principle of an undulator: Alternating magnet pairs (green and blue) with a distance d and a periodicity λ_u generate a magnetic field B (orange) accelerating the electrons perpendicular to their direction of motion (red arrow) and electromagnetic radiation (yellow cones) is emitted. (c) DCM: A Si crystal pair together with an aperture monochromatizes the incoming “white” beam, granting a decent energy bandwidth of the radiation. By rotating the crystals the photon energy can be varied. Different colors thereby represent different photon energies.

At the beginning is a cathode generating electrons, which then are separated into multiple packages or bunches with about 10^{11} electron each while being accelerated within a linear accelerator (LINAC) to a kinetic energy of 100 MeV. In the booster ring the electron bunches are further accelerated to the final energy of 6 GeV while orbiting and are subsequently injected into the large storage ring with a circumference of about 2.3 km. Along the storage ring several insertion devices—like undulators, wigglers, and bending magnets—are installed. Figure 3.4 (b) shows a scheme of an undulator used for the generation of hard X-rays. Alternating magnet pairs, with a distance of d and a periodicity of λ_u , generate a magnetic field \mathbf{B} and accelerate the electrons perpendicular to their direction of motion (red arrow in the side view) on a sinusoidal trajectory. Since the electrons move with relativistic velocities, the resulting emission of the radiation is within the direction of motion (yellow cones). Thereby, the characteristics of the radiation at the exit of such an insertion device depends on several parameters, which are connected to each other via the parameter K [111]:

$$K = \frac{eB\lambda_u}{2\pi m_e c}. \quad (3.18)$$

While for strong magnetic fields \mathbf{B} and large periodicity λ_u the value for K is greater than 1—such devices are called wigglers (or bending magnets for $K \gg 1$)—, for the generation of hard X-rays one uses smaller fields and a shorter periodicity to obtain values for K below 1. As a consequence, the single radiation cones within the undulator can interfere coherently with each other and for the resulting radiation intensity applies $I \propto N^2$, when N is the number of magnet pairs—compared to $I \propto N$, which applies for wigglers.

The radiation generated by an undulator is always linearly polarized in the plane of the accelerated electron trajectories. Nevertheless, there are several concepts—e.g., by combining two undulators whose pairs of magnets are perpendicular to each other or by adding a phase shifter to the beam path—to change the polarization as desired, which also allows for measurements of the X-ray magnetic circular dichroism (XMCD, see also Sec. 7.1.3).

Since for the photoemission experiments in this thesis a monochromatized photon beam with a decent energy bandwidth and a photon energy of more than 3 keV is required, the generated unmonochromatized “white” beam coming from the undulator enters a double crystal monochromator (DCM), which is shown in Fig. 3.4 (c). Here, a pair of two parallel Si crystals are mounted to a goniometer and—due to the heavy heat load of the white beam—are cooled by liquid nitrogen (LN_2). The white beam impinges on the first crystal and the beam is diffracted according to Bragg’s law:

$$2d_{hkl} \sin \theta_B = n\lambda, \quad (3.19)$$

with the diffraction order n , the lattice parameter d in the crystal direction denoted by the miller indices h , k , and l . Depending on the photon energy, by rotating the crystal with the goniometer, the Bragg angle θ_B can be changed. The second Si crystal, rotating at the same time as the first, acts like a mirror, reflecting the beam so that the incoming and outgoing beams have a constant offset of only a few mm or cm, but are still in the same plane. At the end of the monochromator there is a small aperture allowing only a narrow bandwidth of

the beam to exit. This geometry allows, on the one hand, the beamline, which is the part of the synchrotron from the undulator to the endstation where the experiment is carried out, to be built in a straight line. On the other hand, it is very easy just by rotating the crystals to continuously change the photon energy. The most common surface orientation of the Si crystals is (111), but there are also many other surface orientations used at synchrotron facilities. Figure 3.5 (a) shows a variety of usable crystal surfaces and their achievable energy bandwidth as a function of the photon energy at the hard X-ray beamline P22. The standard DCM is denoted with “+−”, while a so-called 4 bounce post-monochromator is labeled with “+ − −+”. By changing the surface orientation one also changes the lattice parameter and therefore the diffraction conditions. By using, e.g., a Si(311) crystal pair, the energy resolution can be increased significantly with respect to Si(111). Figure 3.5 (b) compares the intensity of the monochromatized beam for different crystals. By increasing the energy resolution, one has to sacrifice beam intensity. So when changing the Si(111) to a Si(311) crystal pair, the resolution is increased by more than a factor of 4, but the intensity is decreased by a factor of 5. The highest energy resolution with the used setup can be achieved when using the Si(333) post-monochromator, which results in an intensity loss of a factor of 20 with respect to the Si(111), but allows for an energy resolution of down to 40 meV at 6 keV. Soft X-ray beamlines with much lower photon energies use optical gratings as dispersive elements instead, since the lattice parameters of Si crystals are too small for the larger wavelengths in the soft X-ray regime.

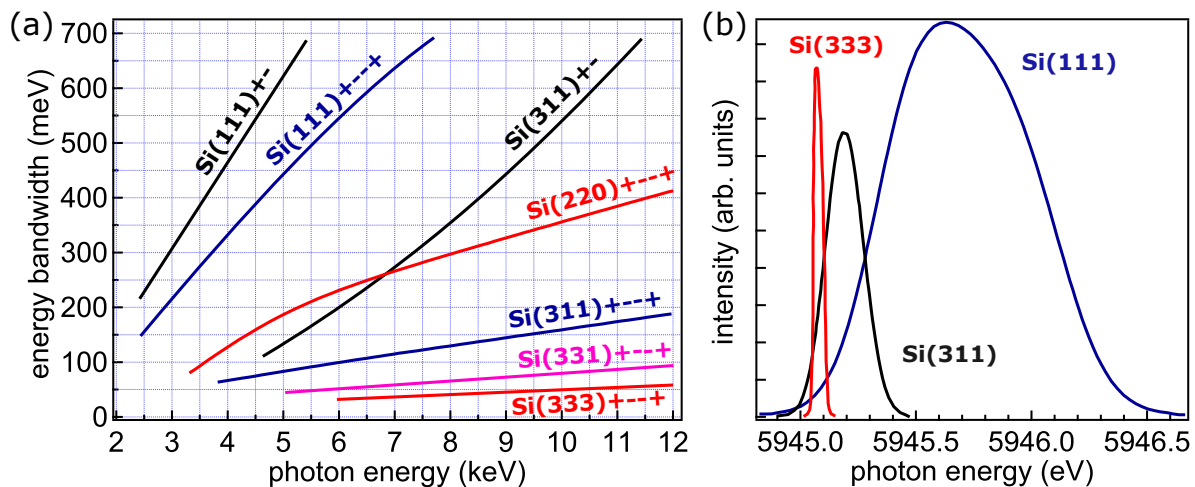


Figure 3.5: (a) Comparison of the energy bandwidth as a function of the photon energy for different crystal surfaces and geometries. (b) Double crystal reflection for the (111), (311), and (333) surface. The area under the curve scales with the beam intensity. The nominal photon energy was set to 5945 eV. The energetic shift between the three spectra originates from the precision of the crystal alignment and goniometer. Data adopted from Ref. [135].

Beside this first interference order originating from the undulator, there are also higher harmonic orders exiting the insertion device with less intensity but higher energy, which is shown in Fig. 3.6. It should be noted that only higher orders with odd numbers contribute to the *on axis* radiation, since the orders with even numbers are not coherent with the undulator field and thus do not emit radiation in the direction of electron motion.

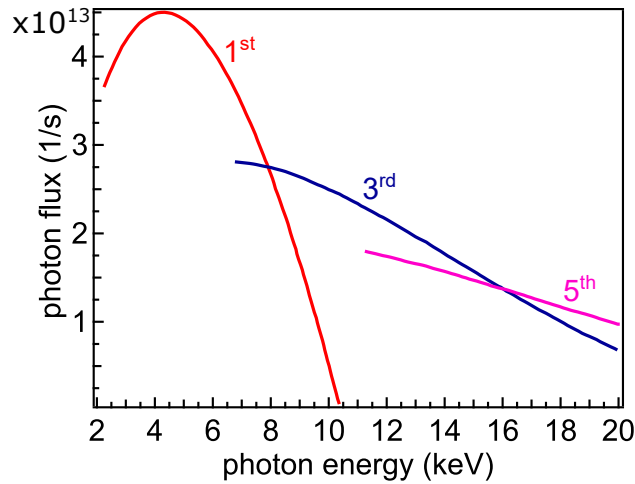


Figure 3.6: Photon flux of the different harmonics as a function of photon energy. Data adopted from Ref. [135].

After the photon beam has been monochromatized it has to be focused, since when exiting the undulator the beam has a beam divergence in both—horizontal and vertical—direction. With a typical beamline length of about 80 m, this divergence would lead to a huge photon beam spot on the sample, which can strongly reduce the spatial resolution and count rate, depending on the experimental instrument used. Therefore, reflection mirrors with surfaces of spherical, toroidal, cylindrical, ellipsoidal or parabolic shape are often used in a total reflection mode [111]. Thus, with two mirrors—one for each plane—the beam size on the sample can be reduced to about $20 \times 20 \mu\text{m}^2$.

Beside the already mentioned quantities, the overall performance of a beamline can be expressed with the spectral brilliance $B_{\Delta\omega/\omega}$ [136]:

$$B_{\Delta\omega/\omega} = \frac{\Delta P}{\Delta\Omega \cdot \Delta A \cdot \Delta\omega/\omega} \text{ [ph/s/mrad}^2\text{/mm}^2\text{/0.1\%bw]}, \quad (3.20)$$

with the photon flux ΔP , the angular divergence of the photons $\Delta\Omega$, the spot size ΔA at the sample position, and the spectral bandwidth $\Delta\omega/\omega$ of the beam. PETRA III reaches values of about 10^{21} ph/s/mrad²/mm²/0.1%bw [137] and is therefore one of the most brilliant synchrotrons in the world, making it superior compared to conventional state-of-the-art X-ray guns on so many levels, especially with respect to HARPES and spin-HAXPES.

4 Spin-Resolved Photoelectron Spectroscopy

In 1916, P. Debye and A. Sommerfeld predicted a *space quantization* of electrons based on their findings from experiments on the Zeeman effect [1]. At that time, modern quantum mechanics did not yet exist and the view of the atomic world was still classical. The most common model for the description of electrons in an atom was the Bohr-Sommerfeld model, which is based on the atomic model of N. Bohr from 1913 [138] and included only the principal (n), angular (l), and magnetic (m) quantum number. Later, in 1922, O. Stern and W. Gerlach conducted an experiment to prove the Bohr-Sommerfeld hypothesis, which states that the direction of angular momentum of a silver atom is quantized. A schematic overview of the Stern-Gerlach experiment is shown in Fig. 4.1. A beam of neutral silver atoms is sent from a furnace through an inhomogeneous magnetic field and the intensity of the beam is observed on a detector screen. While travelling through the magnetic field, the force $\mathbf{F} = \mu_z \cdot \frac{\partial B}{\partial z} \mathbf{e}_z$, with $\frac{\partial B}{\partial z}$ reflecting the inhomogeneity of the magnetic field, acts on the magnetic moment μ_z of the silver atoms. The result of only two intensity spots on the detector instead of an arbitrary distribution of intensity in the z -direction confirms that the outer Ag $5s$ valence electrons must have an intrinsic quantized angular momentum—all other electrons are in closed shells—which can take only two different values. In 1925, G. E. Uhlenbeck and S. Goudsmit hypothesized the existence of the electron *spin* [3], and in 1926 it was W. Pauli who formalized the theory of spin using modern quantum mechanics [4], which had been developed in the meantime by E. Schrödinger and W. Heisenberg. In 1928, P. Dirac upgraded the Pauli equation by introducing the theory of special relativity [5]. These formalisms are described in more detail mathematically below.

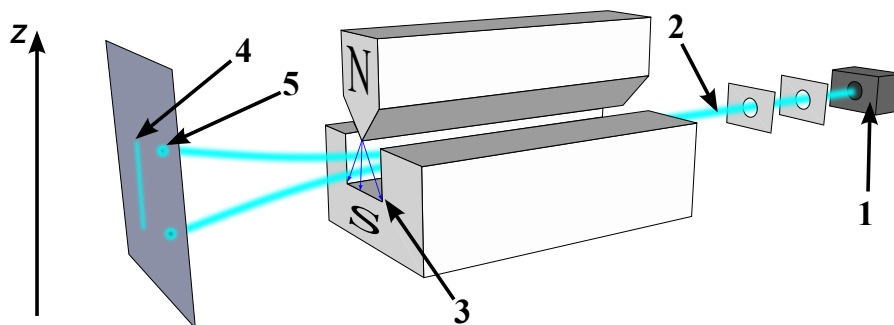


Figure 4.1: Stern-Gerlach experiment: From a furnace (1) neutral silver atoms (2) travel through an inhomogeneous magnetic field (3), being deflected up or down depending on their spin, and are detected on a screen. (4) depicts the classically expected result while (5) the one actually observed. *WikiMedia Commons [139] under the Creative Commons BY-SA 4.0 license.*

4.1 Quantum Mechanical Description of the Electron Spin

The quantum mechanical property of the spin is represented by an operator

$$\mathbf{s} = (s_x, s_y, s_z), \quad (4.1)$$

which satisfies the commutation relations characteristic of angular momenta

$$[s_x, s_y] = i\hbar s_z, \quad [s_y, s_z] = i\hbar s_x, \quad [s_z, s_x] = i\hbar s_y. \quad (4.2)$$

These relations are fulfilled when the spin operator is written as $\mathbf{s} = \hbar/2 \boldsymbol{\sigma}$, with the Pauli spin matrices $\boldsymbol{\sigma} = (\sigma_x, \sigma_y, \sigma_z)$, whereby σ_z is diagonal:

$$\sigma_x = \begin{pmatrix} 0 & 1 \\ 1 & 0 \end{pmatrix}, \quad \sigma_y = \begin{pmatrix} 0 & -i \\ i & 0 \end{pmatrix}, \quad \sigma_z = \begin{pmatrix} 1 & 0 \\ 0 & -1 \end{pmatrix}. \quad (4.3)$$

Assuming a beam of electrons along the z -axis with the projection of the spin aligned along the z -axis, the spin state can be characterized by the spin function \mathcal{X} with complex coefficients a_1 and a_2 :

$$\mathcal{X} = a_1|\alpha\rangle + a_2|\beta\rangle = a_1 \begin{pmatrix} 1 \\ 0 \end{pmatrix} + a_2 \begin{pmatrix} 0 \\ 1 \end{pmatrix} = \begin{pmatrix} a_1 \\ a_2 \end{pmatrix}. \quad (4.4)$$

The basis functions $|\alpha\rangle$ and $|\beta\rangle$ are eigenfunctions of the Pauli matrix σ_z with eigenvalues of ± 1 . The squares $|a_1|^2$ and $|a_2|^2$ give the probability of finding the value $+\frac{\hbar}{2}$ and $-\frac{\hbar}{2}$ with respect to the z -axis in a measurement, and $|a_1|^2 + |a_2|^2 = 1$. This means the spin vector lies somewhere on a cone around the z -axis with the length $s = \sqrt{3/4}\hbar$, resulting in its projection onto the axis being $+\frac{1}{2}\hbar$ or $-\frac{1}{2}\hbar$, which is illustrated in Fig. 4.2.

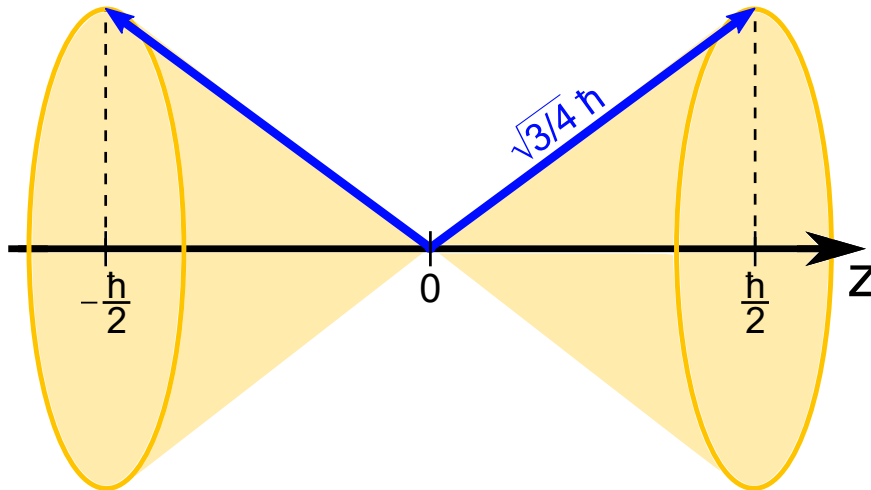


Figure 4.2: Illustration of the two possible spin states *up* and *down* (blue arrows). Both lie on a cone with length $\pm\sqrt{3/4}\hbar$. Projected onto the z -axis the length is $\pm\frac{1}{2}\hbar$.

The polarization \mathbf{P} is defined by the expectation value of the spin operator $\boldsymbol{\sigma}$ and is given for a non-normalized spin function \mathcal{X} by:

$$\mathbf{P} = \frac{\langle \mathcal{X} | \boldsymbol{\sigma} | \mathcal{X} \rangle}{\langle \mathcal{X} | \mathcal{X} \rangle}. \quad (4.5)$$

In contrast to the vector quantity \mathbf{P} , the degree of polarization P_z with respect to the z -axis is a scalar with a value of $-1 \leq P_z \leq 1$ and is given by:

$$P_z = \frac{\langle \mathcal{X} | \sigma_z | \mathcal{X} \rangle}{\langle \mathcal{X} | \mathcal{X} \rangle} = \frac{|a_1|^2 - |a_2|^2}{|a_1|^2 + |a_2|^2}. \quad (4.6)$$

The degree of polarization of an electron beam in z -direction can accordingly be written as:

$$P_z = \frac{N^\uparrow - N^\downarrow}{N^\uparrow + N^\downarrow}, \quad (4.7)$$

where $N^{\uparrow\downarrow}$ is the number of electrons with spin parallel (up) and antiparallel (down) to the z -axis, respectively.

4.2 Spin-Orbit Interaction

Since a Stern-Gerlach experiment is not applicable to measure the spin polarization of an electron beam along a quantization axis—due to its negative charge and the resulting additional Lorentz force—, scattering processes based on exchange interaction or spin-orbit coupling are used to distinguish between the two possible spin states. The following section focuses on SOC in elastic electron-atom scattering since it is more commonly used in modern spin detectors.

Electron beams can be polarized by scattering—analogue to electro-magnetic waves—because the angular distribution of the electrons depends on their polarization state. This can be described combining the principles of quantum mechanics with the relativistic behavior of electrons by linearizing the relativistic generalization of the Schrödinger equation and thus obtain the Dirac equation [5]:

$$\left(\mathcal{H}^2 - c \sum_{\mu} p_{\mu}^2 - m_e^2 c^4 \right) \Psi = 0, \quad (4.8)$$

with \mathcal{H} being the Hamiltonian, c the speed of light, $p_{\mu} = p_x, p_y, p_z$ the components of the momentum operator, m_e the mass of an electron, and Ψ a 4-component spinor. This can also be expressed as:

$$\left(\mathcal{H} - c \sum_{\mu} \alpha_{\mu} p_{\mu} - \beta m_e c^2 \right) \left(\mathcal{H} + c \sum_{\mu} \alpha_{\mu} p_{\mu} + \beta m_e c^2 \right) \Psi = 0, \quad (4.9)$$

with the constant coefficients α_μ and β satisfying the relations:

$$\alpha_\mu \alpha_{\mu'} + \alpha_{\mu'} \alpha_\mu = 2\delta_{\mu\mu'}, \quad \alpha_\mu \beta + \beta \alpha_\mu = 0, \quad \beta^2 = 1. \quad (4.10)$$

This can be verified by solving the linearized equation:

$$\left(\mathcal{H} - c \sum_{\mu} \alpha_{\mu} p_{\mu} - \beta m_e c^2 \right) \Psi = 0. \quad (4.11)$$

For a free electron, one can solve this equation with the ansatz of a plane wave propagating in z -direction:

$$\Psi_{\lambda} = a_{\lambda} e^{i(kz - \omega t)}, \quad \text{with } \lambda = 1, \dots, 4, \quad (4.12)$$

which yields two eigenvectors representing the spin states *up* and *down*:

$$\Psi_{\uparrow} = A \begin{pmatrix} 1 \\ 0 \\ \frac{cp_z}{E+m_e c^2} \\ 0 \end{pmatrix} e^{i(kz - \omega t)}, \quad \Psi_{\downarrow} = B \begin{pmatrix} 0 \\ 1 \\ 0 \\ \frac{-cp_z}{E+m_e c^2} \end{pmatrix} e^{i(kz - \omega t)}, \quad (4.13)$$

with A and B being constants. This can easily be verified since with the spin operator $\mathbf{s} = \hbar/2 \boldsymbol{\sigma}$ and the generalized Pauli spin matrices:

$$\sigma_x = \begin{pmatrix} 0 & 1 & 0 & 0 \\ 1 & 0 & 0 & 0 \\ 0 & 0 & 0 & 1 \\ 0 & 0 & 1 & 0 \end{pmatrix}, \quad \sigma_y = \begin{pmatrix} 0 & -i & 0 & 0 \\ i & 0 & 0 & 0 \\ 0 & 0 & 0 & -i \\ 0 & 0 & i & 0 \end{pmatrix}, \quad \sigma_z = \begin{pmatrix} 1 & 0 & 0 & 0 \\ 0 & -1 & 0 & 0 \\ 0 & 0 & 1 & 0 \\ 0 & 0 & 0 & -1 \end{pmatrix}, \quad (4.14)$$

it directly follows that the spin of an electron is an intrinsic property:

$$\mathbf{s}_z \Psi_{\uparrow} = +\frac{\hbar}{2} \Psi_{\uparrow} \quad \text{and} \quad \mathbf{s}_z \Psi_{\downarrow} = -\frac{\hbar}{2} \Psi_{\downarrow}. \quad (4.15)$$

Introducing an external field by substitution of the momentum \mathbf{p} with $\mathbf{p} - (e/c)\mathbf{A}$, with the vector potential \mathbf{A} and the elementary charge e , and the Hamiltonian \mathcal{H} with $\mathcal{H} - e\phi$, with the scalar potential ϕ , and inserting it in Eq. 4.9 gives [6]:

$$\left[\mathcal{H} - e\phi - c\boldsymbol{\alpha} \cdot \left(\mathbf{p} - \frac{e}{c}\mathbf{A} \right) - \beta m_e c^2 \right] \times \left[\mathcal{H} - e\phi + c\boldsymbol{\alpha} \cdot \left(\mathbf{p} - \frac{e}{c}\mathbf{A} \right) + \beta m_e c^2 \right] \Psi = 0. \quad (4.16)$$

After multiplying and with the approximation of the kinetic and potential energies being small compared to $m_e c^2$ we obtain:

$$\left[\underbrace{\frac{1}{2m_e} \left(\mathbf{p} - \frac{e}{c} \mathbf{A} \right)^2 + e\phi}_{\text{I}} - \underbrace{\frac{e\hbar}{2m_e c} \boldsymbol{\sigma} \cdot \mathbf{B}}_{\text{II}} + i \underbrace{\frac{e\hbar}{4m_e^2 c^2} \mathbf{E} \cdot \mathbf{p}}_{\text{III}} - \underbrace{\frac{e\hbar}{4m_e^2 c^2} \boldsymbol{\sigma} \cdot [\mathbf{E} \times \mathbf{p}]}_{\text{IV}} \right] \Psi = W \Psi, \quad (4.17)$$

with the magnetic field \mathbf{B} and the electric field \mathbf{E} , and $W + m_e c^2$ being the total energy. The term I is the Hamilton operator of the non-relativistic Schrödinger equation for a particle without spin in an electromagnetic field. Combining that with term II, which describes the interaction energy $-\boldsymbol{\mu} \cdot \mathbf{B}$ of a magnetic dipole with the external magnetic field, leads to the Pauli equation for a non-relativistic electron with spin. Thereby, $\boldsymbol{\mu} = (e\hbar/2m_e c) \boldsymbol{\sigma}$ is the operator of the magnetic moment and illustrates once more the reason for using $(\hbar/2) \boldsymbol{\sigma}$ as the spin operator \mathbf{s} . Term III is a relativistic correction which has no classical analogue. Lastly, the fourth term introduces the spin-orbit coupling, which describes the interaction between the electron momentum \mathbf{p} and an electric field \mathbf{E} . Assuming an atom, i.e., a central potential $V(r)$ where $\mathbf{E} = -e^{-1}(dV/dr)(\mathbf{r}/r)$ and the angular momentum of the electron $\mathbf{l} = \mathbf{r} \times \mathbf{p}$, one gets from term IV of Eq. 4.17 the interaction energy U_{SOC} :

$$U_{SOC} = -\frac{e}{2m_e^2 c^2} \mathbf{s} \cdot \left[-\frac{1}{e} \frac{dV}{dr} \frac{\mathbf{r}}{r} \times \mathbf{p} \right] = \frac{1}{2m_e^2 c^2} \frac{1}{r} \frac{dV}{dr} (\mathbf{s} \cdot \mathbf{l}). \quad (4.18)$$

With the Coulomb potential $V(r) = -\frac{Ze^2}{r}$, with Z being the atomic number, one gets:

$$U_{SOC} \propto \frac{Z}{r^3} (\mathbf{s} \cdot \mathbf{l}). \quad (4.19)$$

Since $U_{SOC} \propto 1/r^3$ and $1/r^3 \propto Z^3$ from Eq. 4.19 follows a dependence of $U_{SOC} \propto Z^4$. That means that SOC is strongest for heavy- Z elements like tungsten, gold or iridium and in the close vicinity of the nucleus [140]. Therefore, SOC acts as an additional scattering potential in addition to the Coulomb potential and depends—for a given target material—on the orientation of the spin of the electron with respect to its angular momentum, as is depicted in Fig. 4.3. When an electron passes the nucleus (N) from the right side with the position vector \mathbf{r} (orange), its angular momentum \mathbf{L} (green) is pointing upwards. In Fig. 4.3 this is denoted with a circle and a dot in it. If the spin of the electron is parallel to its angular momentum (blue), the additional scattering potential—beside the attractive Coulomb potential—is also attractive and the electron is deflected more strongly toward the nucleus than an electron with the opposite spin direction (red). Then the spin is antiparallel to the angular momentum and thus the additional potential is repulsive. This results in the electron being less deflected by the nucleus. If the electron passes the nucleus on the left side, the angular momentum is directed downwards, depicted with a circle and a cross in it. The electron with spin-down thus experiences a stronger deflection, as in this case the additional scattering potential is attractive. The electron with spin-up is deflected accordingly less.

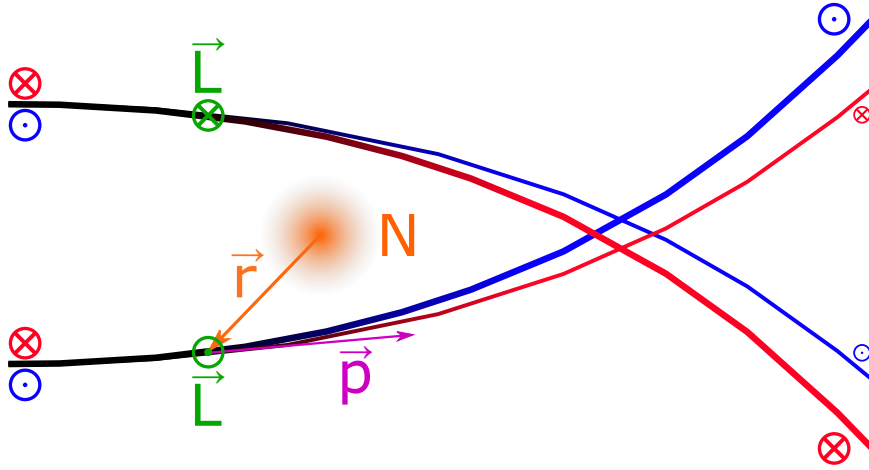


Figure 4.3: Schematic scattering of two electron beams (black) passing the nucleus (N) from the left and right side. \mathbf{L} is the angular momentum, \mathbf{p} the momentum vector, and \mathbf{r} the position vector the electron. The final scattering potential depends on the sign of the angular momentum. Electrons with spin-up are shown in blue and spin-down in red.

4.3 Differential Scattering Cross Sections

Having introduced the Dirac equation and the effect of spin-orbit coupling, we can now treat the resulting differential cross sections for electrons when being elastically scattered off the central potential of the nucleus in a solid. Taking electrons as an incident plane wave in z -direction, expressed as a linear combination of both solutions from Eq. 4.13, to solve the Dirac equation leads to the asymptotic wavefunction Ψ_λ :

$$\Psi_\lambda \xrightarrow{r \rightarrow \infty} a_\lambda e^{ikz} + a'_\lambda(\theta, \phi) \frac{e^{ikr}}{r}, \quad (4.20)$$

with $\lambda = 1, \dots, 4$ being the four components of the wavefunction and $a'_\lambda(\theta, \phi)$ as the amplitude of the scattered spherical wave. From the Schrödinger theory one finds for the generalized differential cross section [6]:

$$\frac{d\sigma}{d\Omega}(\theta, \phi) \equiv \sigma(\theta, \phi) = \frac{\sum_{\lambda=1}^4 |a'_\lambda(\theta, \phi)|^2}{\sum_{\lambda=1}^4 |a_\lambda|^2}. \quad (4.21)$$

This can be simplified by the fact that the a_λ are not independent from each other, which can be seen from Eqs. 4.12 and 4.13:

$$r \equiv \frac{|a_3|}{|a_1|} = \frac{|a_4|}{|a_2|} = \frac{cp_z}{E + m_e c^2}. \quad (4.22)$$

The same relation applies to the a'_λ since far away from the scattering center, one can consider the spherical wave as the result of the superposition of several plane waves propagating in different directions from the center. Thus, for the cross section follows:

$$\sigma(\theta, \phi) = \frac{|a'_1|^2 + |a'_2|^2 + |a'_1|^2 r^2 + |a'_2|^2 r^2}{|a_1|^2 + |a_2|^2 + |a_1|^2 r^2 + |a_2|^2 r^2} = \frac{|a'_1|^2 + |a'_2|^2}{|a_1|^2 + |a_2|^2}. \quad (4.23)$$

Note that the components a'_3 and a'_4 need not to be considered here, since they are small compared to a'_1 and a'_2 . Therefore, in case of a polarisation in $+z$ -direction the asymptotic solutions for the Dirac equation are:

$$\Psi_1 \xrightarrow[r \rightarrow \infty]{} e^{ikz} + f_1(\theta, \phi) \frac{e^{ikr}}{r} \quad \text{and} \quad \Psi_2 \xrightarrow[r \rightarrow \infty]{} 0 + g_1(\theta, \phi) \frac{e^{ikr}}{r}. \quad (4.24)$$

It turns out that the second component after the scattering is not necessarily zero as the spin can be flipped by SOC. This is due to the—from the electron point of view—magnetic field emanating from the moving charge of the nucleus which represents an electric current. This is denoted by the spin-flip amplitude $g_1(\theta, \phi)$. For an incident plane wave polarized in $-z$ -direction it follows analogously:

$$\Psi_1 \xrightarrow[r \rightarrow \infty]{} 0 + g_2(\theta, \phi) \frac{e^{ikr}}{r} \quad \text{and} \quad \Psi_2 \xrightarrow[r \rightarrow \infty]{} e^{ikz} + f_2(\theta, \phi) \frac{e^{ikr}}{r}. \quad (4.25)$$

The scattering problem in the case of the Schrödinger equation can be solved by the partial waves method. Here due to the fact that one has a system of simultaneous differential equations, the solution is much more complicated. Therefore, only the basic idea and the physical background will be discussed in the following. For the detailed calculations the interested reader is referred to the work of Mott and Massey [141].

First, a particular solution with two pairs of $\Psi_1(\theta, \phi)$ and $\Psi_2(\theta, \phi)$ for both spin directions with z being the quantization axis is found. These solutions include a ϕ -dependent term, which does not occur in the Schrödinger treatment of scattering. It is explained by the conservation law for $\mathbf{j}^2 = (\mathbf{l} + \mathbf{s})^2$. Before the scattering $m_s = +1/2$ (assuming the electron spin is in $+z$ -direction) and $m_l = 0$, i.e., the angular momentum component $m_j = +1/2$. The latter must be conserved after the scattering process. A spin flip results in the decrease of the z -component of the spin which must be compensated by an increase of the angular momentum component in this direction. Therefore, there must be a non-zero expectation value for this component. The corresponding operator can be written as:

$$l_z = -i\hbar \frac{\partial}{\partial \phi}, \quad (4.26)$$

which shows, that the solution is a ϕ -dependent term.

By combining the two pairs from the particular solution, a general solution can be found with the scattering amplitudes $f_{1,2}(\theta, \phi)$ and $g_{1,2}(\theta, \phi)$. Thereby, it can be shown that the dependence of the scattering amplitude $f_{1,2}$ can be reduced to the dependence of the scattering angle θ and the scattering phase η , which depend on the energy of the electrons

and on the scattering potential, which is determined by the target material. Therefore, the scattering amplitudes can be expressed by:

$$\begin{aligned} f_2(\theta) &= f_1(\theta) = f(\theta) \\ g_2(\theta, \phi) &= -g_1 e^{-2i\phi} = -g(\theta) e^{-i\phi}. \end{aligned} \quad (4.27)$$

One can now treat the case of an incident wave with an arbitrary spin direction:

$$A \begin{pmatrix} 1 \\ 0 \end{pmatrix} e^{ikz} + B \begin{pmatrix} 0 \\ 1 \end{pmatrix} e^{ikz} = \begin{pmatrix} A \\ B \end{pmatrix} e^{ikz}, \quad (4.28)$$

and therefore one gets for the scattered spherical wave by coherent superposition of Eqs. 4.24, 4.25, 4.27, and 4.28:

$$\begin{pmatrix} a_1' \\ a_2' \end{pmatrix} \frac{e^{ikr}}{r} = A \begin{pmatrix} f_1 \\ g_1 \end{pmatrix} \frac{e^{ikr}}{r} + B \begin{pmatrix} g_2 \\ f_2 \end{pmatrix} \frac{e^{ikr}}{r} = \begin{pmatrix} Af - Bge^{-i\phi} \\ Bf + Age^{i\phi} \end{pmatrix} \frac{e^{ikr}}{r}, \quad (4.29)$$

and finally the differential cross section from Eq. 4.23:

$$\sigma(\theta, \phi) = \underbrace{(|f|^2 + |g|^2)}_{\text{I}} \left[1 + \underbrace{\left(i \frac{fg^* - f^*g}{|f|^2 + |g|^2} \right)}_{\text{II}} \underbrace{\left(\frac{-AB^* e^{i\phi} + A^* B e^{-i\phi}}{i(|A|^2 + |B|^2)} \right)}_{\text{III}} \right]. \quad (4.30)$$

Thereby, the first term describes the scattering amplitude, which is independent of the spin polarization. Term II is the so-called Sherman function $S(\theta)$, which is a measure for the polarization ability of the scattering process and depends on the angle θ . Lastly, the third term describes the cross section, which depends on the angle ϕ and the spin polarisation.

For a better understanding, we consider the case with $A = B = 1$ and the beam being fully polarized in x -direction (see Fig. 4.4 (a)). This simplifies Eq. 4.30 to:

$$\sigma(\theta, \phi) = (|f|^2 + |g|^2)[1 - S(\theta) \sin \phi]. \quad (4.31)$$

The ϕ -dependence here is important since the primary beam is not axially symmetric with respect to the propagation direction. For the electrons with spin-up (blue), the intensity is minimal when scattered to the right ($\phi = 90^\circ$, θ) and maximal when scattered left ($\phi = 270^\circ$, θ). For the other spin direction (red) it is accordingly vice versa, which is also known as the left-right scattering asymmetry and is the basic operating principle of a Mott detector (see Sec. 4.4.1). In Fig. 4.4 (b) the cross section $\sigma(\theta, \phi)$ is plotted against the angle ϕ and a constant θ for both, spin-up and spin-down. For the angles $\phi = 0^\circ$ and 180° the scattering intensity for both spin polarizations is equal.

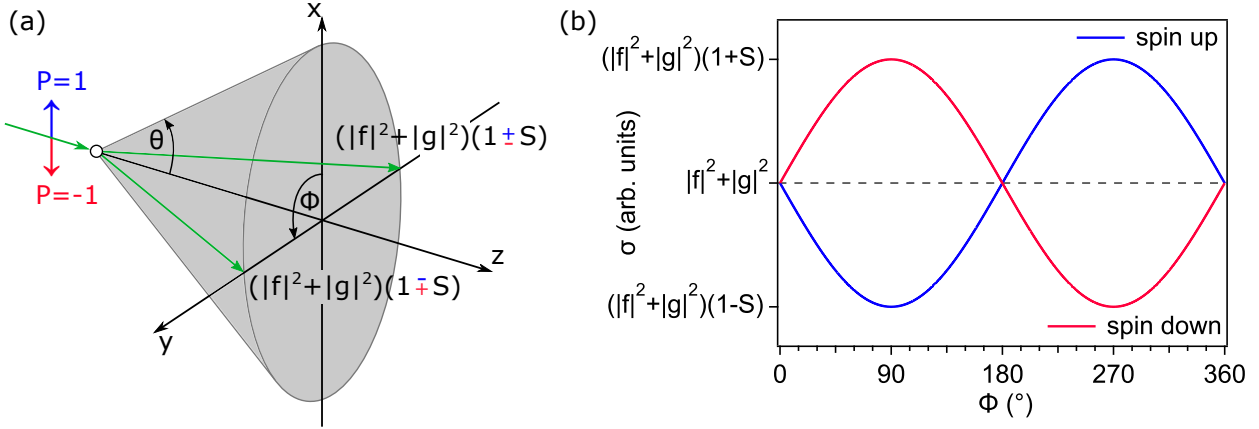


Figure 4.4: (a): Schematic view of the left-right scattering asymmetry for two differently polarized electron beams in x -direction. Blue denotes the spin-up electrons and red spin-down. The green arrows indicate the angles under which the electrons are scattered within the yz -plane. (b): Cross section σ plotted against the angle ϕ for the two different polarization directions up (blue) and down (red).

By defining the sum of the squared scattered intensities as the total intensity $I(\theta) = |f(\theta)|^2 + |g(\theta)|^2$, and using the unity vector:

$$\hat{\mathbf{n}} = \frac{\mathbf{k}_1 \times \mathbf{k}_2}{|\mathbf{k}_1 \times \mathbf{k}_2|}, \quad (4.32)$$

which is perpendicular to the scattering plane, and \mathbf{k}_1 and \mathbf{k}_2 are the electron momenta before and after the scattering, one gets with the polarization \mathbf{P} and Eq. 4.31:

$$\sigma(\theta, \phi) = I(\theta)[1 + S(\theta)\mathbf{P} \cdot \hat{\mathbf{n}}]. \quad (4.33)$$

The advantage of this formula is that it is independent of the choice of the coordinate system since the scalar product is invariant under coordinate transformations. One sees that only the spin component which is perpendicular to the scattering plane contributes to the scattering asymmetry. In contrast, when the polarisation lies within the scattering plane, the components make no contribution at all.

4.4 Different Concepts of Spin Detectors

The early development of special detectors for spin-resolved photoemission experiments started in the 1960's with the Mott detector [8] based on the left-right asymmetry introduced in the previous section. Throughout the next decades, this type of detector was mostly utilized for the investigation of ferromagnetic materials [142]. Later—from the 1980's on—new detector concepts were introduced: Low-energy electron diffraction of spin-polarized electrons (SPLEED) [143], diffuse scattering detector [144], and multichannel spin-filtering using W(001) [145], Ir(100) [146], or Au/Ir(100) [147], which are all based on SOC. While the first concepts were only applied in the soft X-ray and VUV range, they were also adapted

for the more challenging hard X-ray regime starting in the 2010s. First for the study of core levels [148], later also for valence states [149], both based on SPLEED detectors.

Mott, SPLEED, and multichannel detectors are the most common and widely used spin detector concepts for spin-resolved photoemission. In the following section, these three detector concepts are discussed in detail, especially with respect to their Figure-of-Merit. The interested reader will find a comprehensive listing of less common or highly specialized detector concepts elsewhere [142].

4.4.1 Mott Detector

The Mott detector, the principle of which was first presented in 1966 [8], is today the most commonly used spin detector, which utilizes spin-orbit coupling. Figure 4.5 shows a schematic view of its principle concept. A highly accelerated electron beam with intensity I_0 and a kinetic energy of $E_{\text{kin}} = 20 \text{ keV} - 120 \text{ keV}$, which is polarized with respect to the quantization axis z , is quasielastically scattered off by a high- Z target material like Au. Due to the SOC induced left-right asymmetry, the scattering probability for electrons polarized in $-z$ -direction is different from that the ones polarized in $+z$ -direction. Therefore, the scattered intensity measured by the channeltron (CT) on the left side I_L is different from the one measured on the right side I_R .

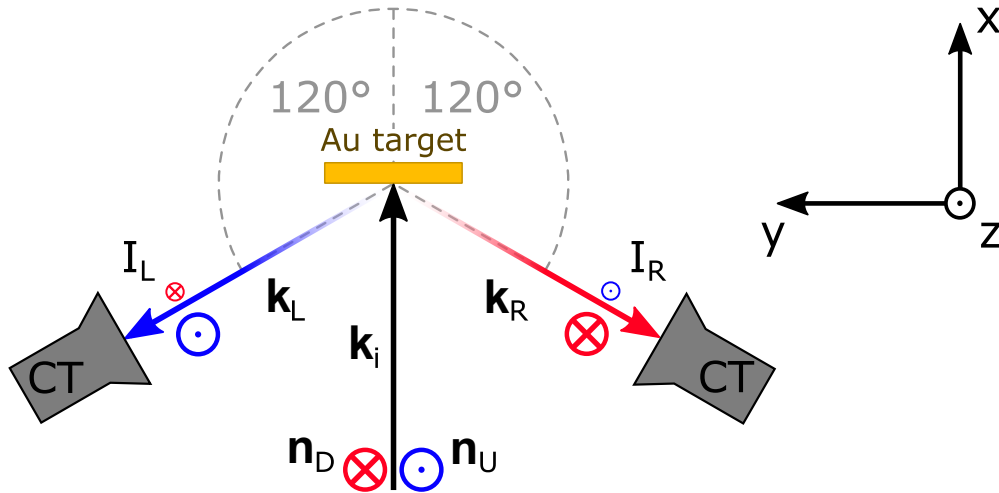


Figure 4.5: Schematic view of a Mott detector: Electron beam with $E_{\text{kin}} = 20 \text{ keV} - 120 \text{ keV}$ polarized along the quantization axis z is scattered at a high- Z target, e.g., a polycrystalline gold foil. The two channeltrons (CT) are within the scattering plane (xy -plane perpendicular to the quantization axis) at a scattering angle of 120° .

In this geometry, the momentum vector of the initial beam is $\mathbf{k}_i = (1, 0, 0)^T$, and the vectors of the scattered beams $\mathbf{k}_L = 1/\sqrt{5}(-1, 2, 0)^T$ and $\mathbf{k}_R = 1/\sqrt{5}(-1, -2, 0)^T$, the spin pointing towards the positive z -direction (spin-up) is denoted with the unity vector $\mathbf{n}_U = (0, 0, 1)^T$ and the one pointing in the opposite direction (spin-down) with $\mathbf{n}_D = (0, 0, -1)^T$.

Using the Eqs. 4.32 and 4.33 the scattered intensities can be expressed by:

$$\begin{aligned}
I_L(\theta) &= \sigma_{\uparrow,L}(\theta)N_{\uparrow} + \sigma_{\downarrow,L}(\theta)N_{\downarrow} \\
&= N_{\uparrow}I(\theta) \left[1 + S(\theta) \begin{pmatrix} 0 \\ 0 \\ 1 \end{pmatrix} \cdot \begin{pmatrix} 0 \\ 0 \\ 1 \end{pmatrix} \right] + N_{\downarrow}I(\theta) \left[1 + S(\theta) \begin{pmatrix} 0 \\ 0 \\ -1 \end{pmatrix} \cdot \begin{pmatrix} 0 \\ 0 \\ 1 \end{pmatrix} \right] \\
&= N_{\uparrow}I(\theta)[1 + S(\theta)] + N_{\downarrow}I(\theta)[1 - S(\theta)],
\end{aligned} \tag{4.34}$$

and

$$\begin{aligned}
I_R(\theta) &= \sigma_{\uparrow,R}(\theta)N_{\uparrow} + \sigma_{\downarrow,R}(\theta)N_{\downarrow} \\
&= N_{\uparrow}I(\theta) \left[1 + S(\theta) \begin{pmatrix} 0 \\ 0 \\ 1 \end{pmatrix} \cdot \begin{pmatrix} 0 \\ 0 \\ -1 \end{pmatrix} \right] + N_{\downarrow}I(\theta) \left[1 + S(\theta) \begin{pmatrix} 0 \\ 0 \\ -1 \end{pmatrix} \cdot \begin{pmatrix} 0 \\ 0 \\ -1 \end{pmatrix} \right] \\
&= N_{\uparrow}I(\theta)[1 - S(\theta)] + N_{\downarrow}I(\theta)[1 + S(\theta)].
\end{aligned} \tag{4.35}$$

With the scattered intensities and Eq. 4.7 the asymmetry A can now be determined:

$$\begin{aligned}
A &= \frac{I_L - I_R}{I_L + I_R} \\
&= \frac{N_{\uparrow}[1 + S(\theta)] + N_{\downarrow}[1 - S(\theta)] - (N_{\uparrow}[1 - S(\theta)] + N_{\downarrow}[1 + S(\theta)])}{N_{\uparrow}[1 + S(\theta)] + N_{\downarrow}[1 - S(\theta)] + N_{\uparrow}[1 - S(\theta)] + N_{\downarrow}[1 + S(\theta)]} \\
&= S(\theta) \frac{N_{\uparrow} - N_{\downarrow}}{N_{\uparrow} + N_{\downarrow}}.
\end{aligned} \tag{4.36}$$

Most of the Mott detectors—typically using a gold scattering target—are operating in this geometry with a scattering angle of 120° and a scattering energy of 100 keV since the Sherman function is maximal for these parameters [150].

With the polarization P and the number of the total photoelectrons $N = N_{\uparrow} + N_{\downarrow}$ the spectral intensities for spin-up (N_{\uparrow}) and spin-down (N_{\downarrow}) can be expressed by:

$$N_{\uparrow\downarrow} = \frac{1}{2}(1 \pm P)N. \tag{4.37}$$

It has to be considered that the measurement of asymmetry is subject to both, systematic (ΔP_{sys}) and statistical (ΔP_{stat}) errors. The error of the polarization ΔP can be expressed as [151]:

$$\Delta P = \sqrt{\Delta P_{sys}^2 + \Delta P_{stat}^2} = \sqrt{\left(\frac{A}{S^2}\Delta S\right)^2 + \left(\frac{\Delta A}{S}\right)^2}. \tag{4.38}$$

While the error of the Sherman function ΔS is unknown, the error of the asymmetry ΔA can be expressed using Gaussian error propagation of Eq. 4.36:

$$\begin{aligned}\Delta A &= \sqrt{\left(\frac{\partial A}{\partial I_L}\right)^2 \Delta I_L^2 + \left(\frac{\partial A}{\partial I_R}\right)^2 \Delta I_R^2} \\ &= \sqrt{\left(\frac{2I_L}{(I_L + I_R)^2}\right)^2 I_L + \left(\frac{-2I_R}{(I_L + I_R)^2}\right)^2 I_R} \\ &= \sqrt{\frac{4I_L I_R}{I^3}},\end{aligned}\tag{4.39}$$

where $I = I_L + I_R$ and the count rate statistics of the detector $\Delta I_{L,R} = \sqrt{I_{L,R}}$ is already included. With $1 - P^2 S^2 = 4I_L I_R / I^2$ it follows that:

$$\Delta A = \sqrt{\frac{1}{N}(1 - P^2 S^2)},\tag{4.40}$$

and therefore the statistical error of the polarization:

$$\Delta P_{stat} = \frac{\Delta A}{S} = \sqrt{\frac{1}{N} \left(\frac{1}{S^2} - P^2 \right)} \simeq \sqrt{\frac{1}{N S^2}},\tag{4.41}$$

where the term P^2 can be neglected since $P^2 \ll 1/S^2$. With the relation $N \propto I/I_0$ the statistical error can be further expressed by:

$$\Delta P_{stat} \propto \frac{1}{S \sqrt{I/I_0}},\tag{4.42}$$

with I_0 being the intensity of the incident beam and I that of the elastically scattered beam. This expression is a constant factor of the spin polarimeter and its reciprocal square is called efficiency or Figure-of-Merit (FoM):

$$\text{FoM} = S^2 \frac{I}{I_0}.\tag{4.43}$$

Thus, the efficiency strongly depends on the ability of the used target material to polarize the electron beam and its probability of electron scattering, which determines the ratio of scattered and incident intensity. For an ideal detector, where every electron is elastically scattered and the Sherman function is 1, the FoM has a maximum value of 1.

Although the high scattering energies of up to 120 keV make high demands on the experimental setup, e.g., because of the complex insulation of electrical contacts, this is necessary because the Mott scattering cross sections decrease strongly at lower energies [152]. At these high energies, a typical value for the scattering probability of the Au target is of the order of 10^{-2} and the Sherman function is about 0.2. This leads to a FoM of only $\approx 10^{-4}$ [153],

which illustrates the extremely low efficiency of such spin polarimeters, so that long measuring times are required to get a decent signal-to-noise ratio.

However, there is still instrumental development for spin detectors based on Mott scattering. Strocov *et al.* [154] have presented a concept for an imaging Mott detector (iMott) operating with a kinetic energy of 40 keV and a Au target. However, the determination of its FoM is still pending.

4.4.2 Low-Energy Electron Diffraction of Spin-Polarized Electrons

Another way to utilize spin-orbit interaction for spin-resolved photoemission was first successfully introduced in 1979 and is based on low-energy electron diffraction of spin-polarized electrons (SPLEED) [7]. Figure 4.6 shows the first concept of such a detector.

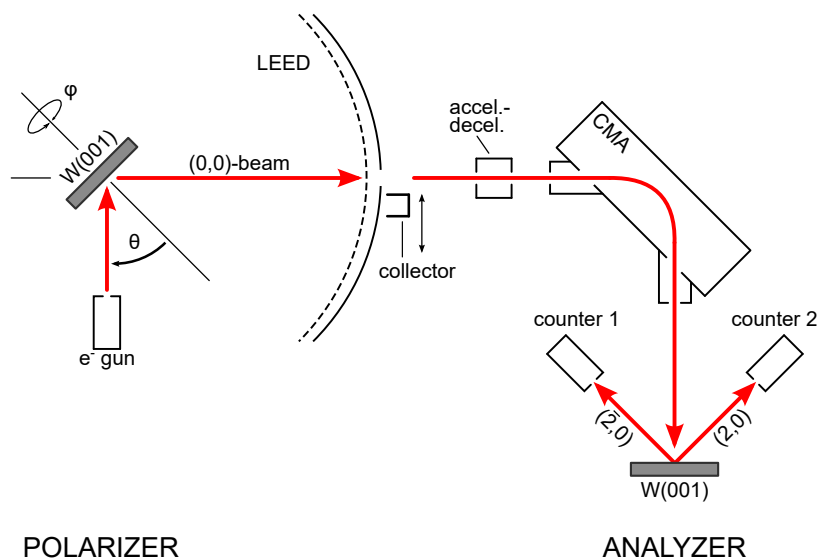


Figure 4.6: Schematic view of the first SPLEED detector and its basic concept from 1979. Figure adapted from Ref. [7].

In this double-scattering experiment unpolarized electrons from an electron gun impinge on a W(001) crystal (polarizer). The specular reflected (0,0) and now polarized electron beam passes through a hole in the LEED screen, and with a movable Faraday cup (collector) the quasielastically scattered intensity can be measured. Entering the analyzer, the kinetic energy of the electron beam can be adjusted with an acceleration-deceleration stage and subsequently analysed with a cylindrical mirror analyzer (CMA) before the beam impinges with an energy of $E = 105 \text{ eV}$ on the second W(001) crystal. While the incidence angle at the first W crystal is $\theta = 47.5^\circ \pm 1^\circ$ with respect to the surface normal, the angle at the second one is $\theta = 0^\circ \pm 0.5^\circ$, which is a typical geometry for LEED experiments. Two channeltrons detect the intensity of the diffracted (2,0) and $(\bar{2},0)$ beams. By rotating the first crystal, the intensity and polarization of the (0,0) beam can be changed. Figure 4.7 shows the rotation diagrams for (a) the intensity and (b) the polarization of the beam with a kinetic energy of 100 eV (blue dots) compared to theoretical calculations (red lines).

For the polarization P applies:

$$P = \frac{1}{B} \cdot \frac{A - T}{1 - AT}, \quad (4.44)$$

with A being the measured asymmetry determined by the different intensities from the two channeltrons, $T \leq 2\%$ being the apparatus asymmetry, and $B = 0.28 \pm 0.05$ the experimentally determined detector sensitivity, which corresponds to the Sherman function of Mott detectors and is the intensity asymmetry which would be obtained for a totally polarized incident beam [7]. The reader interested in how the calculations were performed is referred to the relativistic LEED theory by R. Feder [155–157].

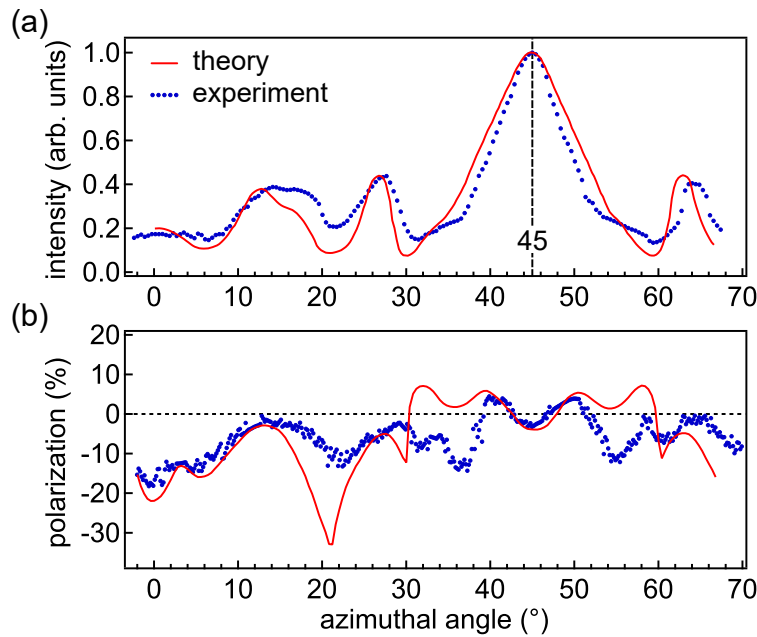


Figure 4.7: Experimentally determined rotation diagrams for a (0,0) beam with 100 eV kinetic energy compared to theoretical calculations based on the relativistic LEED theory: (a) Intensity, normalized at $\phi = 45^\circ$; (b) Polarization. Data adapted from Ref. [7].

Within the kinematic diffraction theory, which considers only single diffraction effects and describes the diffraction at single crystals, the intensity and the polarisation should remain constant when rotating the crystal, since the diffraction condition is independent of the azimuthal angle [140]. But both, the experiment as well as the theory show four pronounced maxima of the intensity and even a change in the sign of the polarisation. This can only be explained by the dynamic diffraction theory considering multiple scattering of low-energy electrons. The maximum at $\phi = 45^\circ$ and the missing maximum at $\phi = 0^\circ$ can be referred to the fourfold symmetry of W(001) [140]. This experiment clearly shows that the multiple scattering of electrons play a significant role and therefore the polarisation strongly depends on the azimuthal angle. While in the kinematic approximation the intensity and the asymmetry are related in such a way that at a maximum in intensity the asymmetry becomes minimal, both quantities are independent of each other when multiple scattering is taken into account. Therefore, for a SPLEED detector, one must find the correct scattering parameters such as the azimuthal angle ϕ , the scattering angle θ , and the scattering energy

E_{scatt} at which—in the best case—the scattering intensity and asymmetry are maximal. Although, the FoM is comparable to a Mott detector, the advantage of SPLEED detectors is the low scattering energy of only about 100 eV and therefore, they do not have to handle high voltages, which makes the work less demanding and safer [142].

4.4.3 Imaging Spin-Filtering with Multichannel Detection

Both previously described spin detectors use channeltrons for electron counting which, due to the fact that those are *single* channel detectors, lack the ability of multiplexing. To overcome this obstacle and the resulting low count rates and to exploit the capability of modern electron spectrometers measuring a two-dimensional electron distribution using a microchannel plate (MCP) in combination with a charged coupled device (CCD) detector or a delayline detector (DLD), *multichannel imaging* spin-filtering—like SPLEED also based on specular reflection at a single crystal—has been developed over the last 10 years [145, 146]. The basic principle for a W(001) spin-filter crystal with 45° scattering angle is shown in Fig. 4.8 for the real space (a) and reciprocal space (b) including the Ewald construction for two different scattering energies.

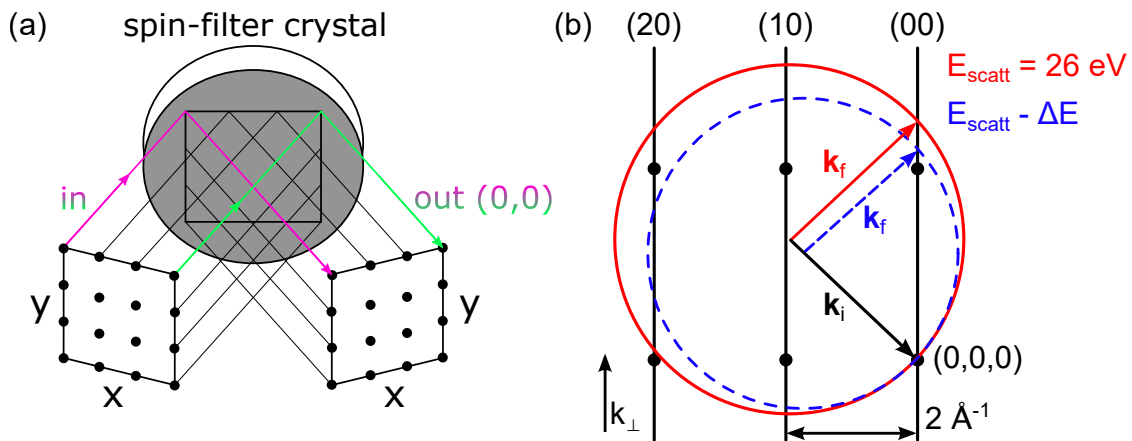


Figure 4.8: Principle of an imaging spin-filter crystal W(001) with 45° scattering angle reflecting a two-dimensional electron distribution in (a) real space and (b) reciprocal space for two different scattering energies. Figures adapted from Ref. [158].

Hereby, a two-dimensional photoelectron distribution impinges on a spin-filter crystal at a scattering angle with respect to the surface normal (not shown here) and with a certain scattering energy E_{scatt} . Which physical quantity the two axes of the electron distribution represent, depends on the use of the respective dispersive element. When using an HDA, x refers to the angular or non-dispersive reciprocal k_x -direction and y represents the kinetic energy of the photoelectrons (see Sec. 5.1.1). Instead, when TOF-based energy recording is employed, both axes refer to the reciprocal directions k_x and k_y , while the kinetic energy is encoded in the time-of-flight (see Sec. 5.2.2). The parallel electron beams are specularly reflected while they—due to their low scattering energy of several 10 eV—penetrate only ≈ 4 monolayers into the spin-filter crystal [122]. As described in Sec. 4.2 SOC is strong for high- Z elements. Thus, standard crystals for this kind of spin detector are, e.g., W(001) and

Ir(100). For the latter a passivation of the surface with a pseudomorph gold layer is often used to extend the lifetime of the crystal surface and also to enhance the Sherman function. The required thorough surface preparation of the spin-filter crystal will be discussed in detail in Sec. 5.1.2. Depending on the scattering energy E_{scatt} and angle θ the measured asymmetry and reflectivity of these crystals strongly differ. Figure 4.9 shows the reflectivity, asymmetry, and resulting FoM for different diffraction conditions for W(001) and Au/Ir(100) spin-filter crystals. These measurements show that only a few working points are favorable for a high FoM and an elaborate calibration of the spin-filter crystal is needed. To determine the spin asymmetry, always a set of two measurements has to be performed. Thereby, three different practical ways have been established so far, with the scattering angle always remaining constant:

- Measuring the sample magnetized in two opposite directions with respect to the quantization axis of the spin detector at a fixed scattering energy E_{scatt} [159].
- If the asymmetry shows a positive and a negative maximum in about 1 eV energy range, switch E_{scatt} between the two values for each measurement [160].
- Rotate the spin-filter crystal by about 30° with respect to its surface normal (azimuthal angle ϕ) and slightly adjust E_{scatt} for both measurements [161].

Which method to prefer depends on the electron spectrometer and spin-filter crystal used. In this thesis, the first method of re-magnetizing the sample is used for the spin-resolved measurements.

The reflected and spin-filtered (0,0) electron beam is then recorded with a two-dimensional DLD. A short overview of the basic structure and operation of a DLD is given in the appendix. To compare the FoM of a spin detector based on an imaging spin-filter with state-of-the-art single-channel acquisition, the *two-dimensional* Figure-of-Merit (FoM_{2D}) can be inferred from Eq. 4.43 by multiplication with the number of simultaneously resolved data points N :

$$\text{FoM}_{2\text{D}} = N \langle \text{FoM} \rangle = N \langle S^2 \frac{I}{I_0} \rangle. \quad (4.45)$$

For, e.g., $N = 1000$ data points together with a reflectivity of 1.2 %, and a Sherman function of 0.41 it follows:

$$\text{FoM}_{2\text{D}} = 1000 \cdot (0.41^2 \cdot 1.2 \times 10^{-2}) \simeq 2.0. \quad (4.46)$$

Compared to a Mott or SPLEED detector, such an imaging spin-filter with multichannel acquisition is therefore 10^4 times more efficient.

4.5 Summary and Discussion

After introducing the quantum mechanical properties of the electron spin, its interaction with the orbital momentum and the resulting differential cross sections for spin-up and spin-down electrons, different detector concepts based on SOC were presented. While a

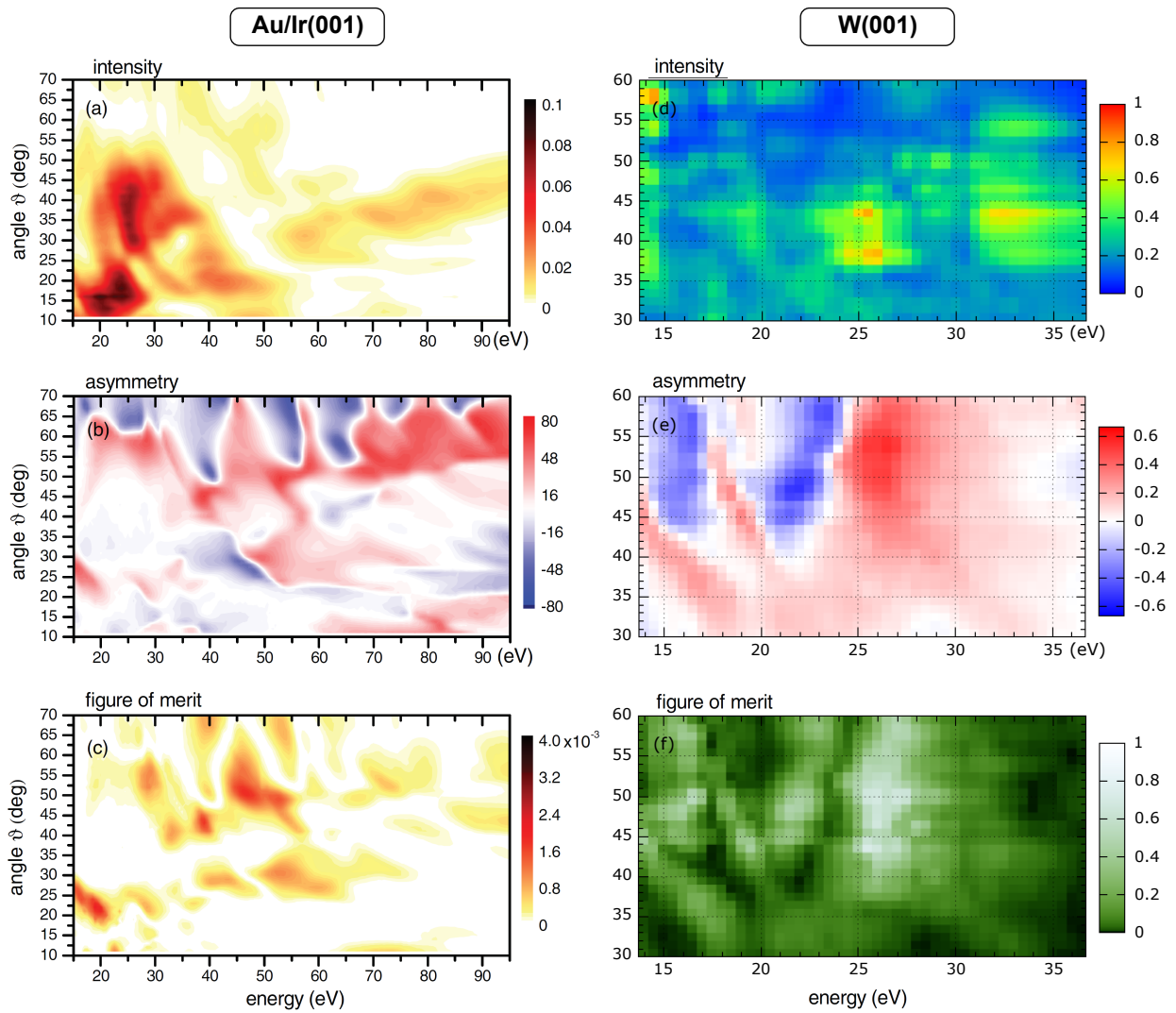


Figure 4.9: Experimentally determined reflectivity, asymmetry, and FoM for Au/Ir(100) (left) [162] and for W(001) (right) [163].

Mott and a SPLEED detector have a comparable FoM, the multichannel acquisition of the two-dimensional spin-filter concept has enormously increased the effective FoM (FoM_{2D}) by a factor of 10^4 , making this type of spin detector superior. In Fig. 4.10 the historical development of the different concepts and their FoM for the past 60 years is shown [7, 8, 145, 158, 164–175]. While detectors based on Mott or exchange scattering are usually combined with an HDA, the introduction of TOF-based energy recording lays the foundation for an instrumental development closer to the theoretical maximum of the FoM of 1. It was not until the introduction of multichannel spin-filtering and the two-dimensional FoM_{2D} that came with it, that a major and important leap in the efficiency of spin detectors was made, allowing for efficiencies far beyond that of single-channel spin detectors. This improvement results in much higher count rates and is thus a key feature for spin-resolved *hard X-ray* photoelectron spectroscopy.

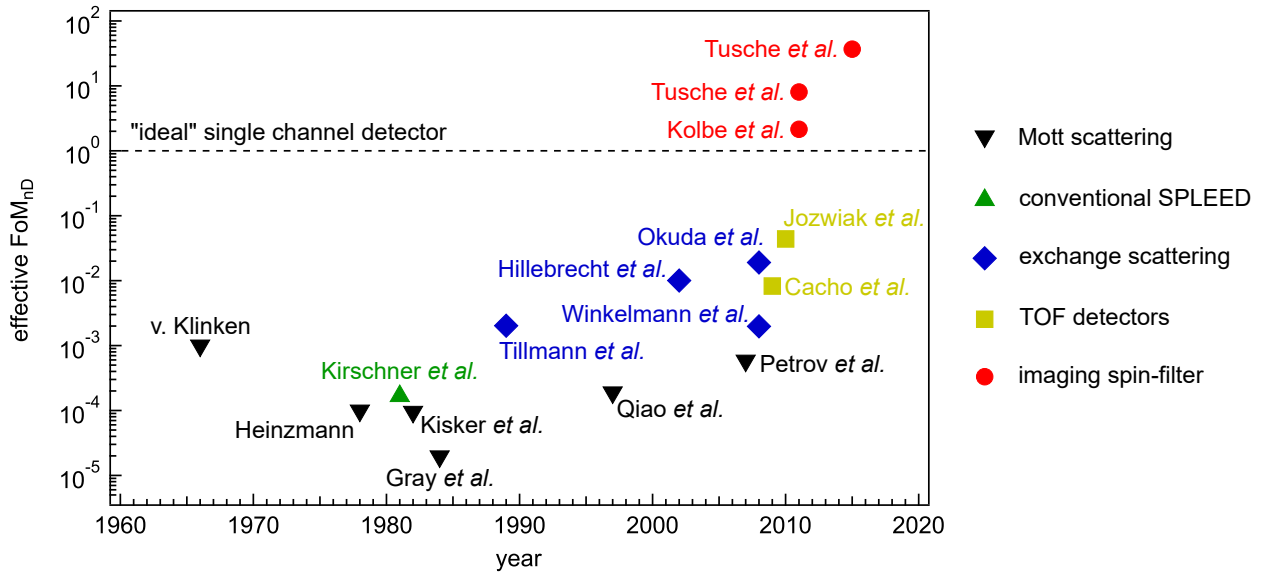


Figure 4.10: Overview of the development of different spin detector concepts over the past 60 years. Data adapted from Ref. [176].

Thus, in the following thesis, this technique—previously exploited for the VUV and soft X-ray regime only—is adapted for the high energy range featuring two different instrumental concepts. The first is the adaptation of an already existing setup for HARPES using an HDA, which is extended by an external spin detector including a W(001) spin-filter crystal. And the second concept is a newly developed k -space or momentum microscope, featuring TOF-based energy recording with the built-in option of spin-filtering using an Ir(100) crystal. Both concepts are discussed in detail and compared to each other to find the most suitable instrumental setup for studying the electronic and magnetic properties of complex oxides.

5 Concepts and Implementation of a Spin-HAXPES Endstation

The distribution in energy, direction, start time and position of the emitted photoelectron cannot be directly observed, but has to be translated by an electron spectrometer, which therefore plays a central role when performing PES. In the early days, only the electron intensity I was usually recorded using a single channel detector—and thus no lateral information—and measuring point by point, which can be accordingly described as a zero-dimensional recording scheme. Later, such curves could be acquired by measuring the intensity of the photoelectrons according to their time-of-flight (TOF) $I(E_{\text{kin}})$, in which the kinetic energy is encoded, in one shot, which improved the recording scheme to one-dimensional. With the introduction of multichannel detectors in the 1970s this situation has begun to change [177]. From then on, with the use of hemispherical deflection analyzers (HDAs) it was possible to measure two-dimensions simultaneously (energy together with one reciprocal direction $I(E_{\text{kin}}, k_x)$, or two reciprocal direction at one energy $I(k_x, k_y)$) [178]. By combining such 2D detectors with the TOF energy recording instead, it was possible to measure both reciprocal directions along with the kinetic energy, resulting in a three-dimensional recording scheme $I(E_{\text{kin}}, k_x, k_y)$. With the concept of an imaging spin detector which maintains a two-dimensional electron distribution while filtering the electron spin, even a four-dimensional recording scheme $I(P_x, E_{\text{kin}}, k_x, k_y)$, with the polarization in x -direction P_x , could be achieved, which opens new astonishing ways for PES to explore. This thesis is about the implementation, characterization, and commissioning of two different technical approaches for hard X-ray based angle- and spin-resolved photoemission. The first one is the upgrade of the existing HAXPES endstation equipped with an HDA at the hard X-ray beamline P09 of the storage ring of PETRA III (DESY) with an external spin detector chamber. The second one is a completely new designed momentum-microscope featuring TOF energy recording with built-in spin-filter option set up at beamline P22 (DESY). Both instrumental approaches were developed by the group of Prof. Schönhense (University of Mainz).

In the following sections, a detailed overview of the basic principles of both spectrometer types is given with focus on their technical realization when combined with an imaging spin-filter as well as advantages and challenges when performing momentum- and spin-resolved photoemission in the hard X-ray regime.

5.1 Hemispherical Deflection Analyzer with External Spin Detector

The hemispherical deflection analyzer is the most widely used spectrometer type when it comes to core-level PES as well as ARPES. This section is about the basic principle of an HDA—the high energy and high resolution electron analyzer SPECS Phoibos 225HV—which is equipped with an external spin detector chamber including a W(001) spin-filter crystal and a DLD at its exit. After that, the characterization and first measurements with this setup are discussed in detail and which obstacles have to be solved as well as future improvements.

5.1.1 Basic Principles

Hemispherical Deflection Analyzer

The basic design of an HDA is discussed based on Fig. 5.1 (a) with the spherical coordinate system shown in (b). A lens system is attached in front of the entrance of two hemispheres with the radii $R_1 < R_2$. The very first lens defines the entrance of the photoelectrons emitted from the sample, while the sample is located in one of the analyzer's focal plane and the electron detector in the other. This geometry terminates the spherical field of the hemisphere at the entrance and exit of the analyzer and reduces aberrations. To achieve a decent energy resolution, entrance and exit slits with a finite width d_1 and d_2 are available. For the photoelectrons entering the hemispheres, the equation of motion can be expressed by [179]:

$$E_{\text{tot}} = U + T = \text{const.} \quad \Leftrightarrow \quad \dot{E}_{\text{tot}} = 0, \quad (5.1)$$

with the potential energy U and the kinetic energy T . Using the radial coordinates shown in Fig. 5.1 (c), the velocity of the electrons can be expressed as $v = \sqrt{\dot{r}^2 + r^2\dot{\phi}^2}$. Thus, for the kinetic energy follows:

$$T = \frac{1}{2}m_e v^2 = \frac{1}{2}(\dot{r}^2 + r^2\dot{\phi}^2), \quad (5.2)$$

with the radial (\dot{r}) and angular ($\dot{\phi}$) velocities. Since the symmetry of the analyzer is spherical, the total angular momentum is also conserved:

$$L = m_e r^2 \dot{\phi} = \text{const.} \quad \Leftrightarrow \quad \dot{L} = 0, \quad (5.3)$$

$$L^2 = m_e^2 r^4 \dot{\phi}^2 = 2m_e r^2 \left(T - \frac{m_e}{2} \dot{r}^2 \right). \quad (5.4)$$

The kinetic energy can therefore be written as:

$$T = \frac{L^2}{2m_e r^2} + \frac{m_e}{2} \dot{r}^2. \quad (5.5)$$

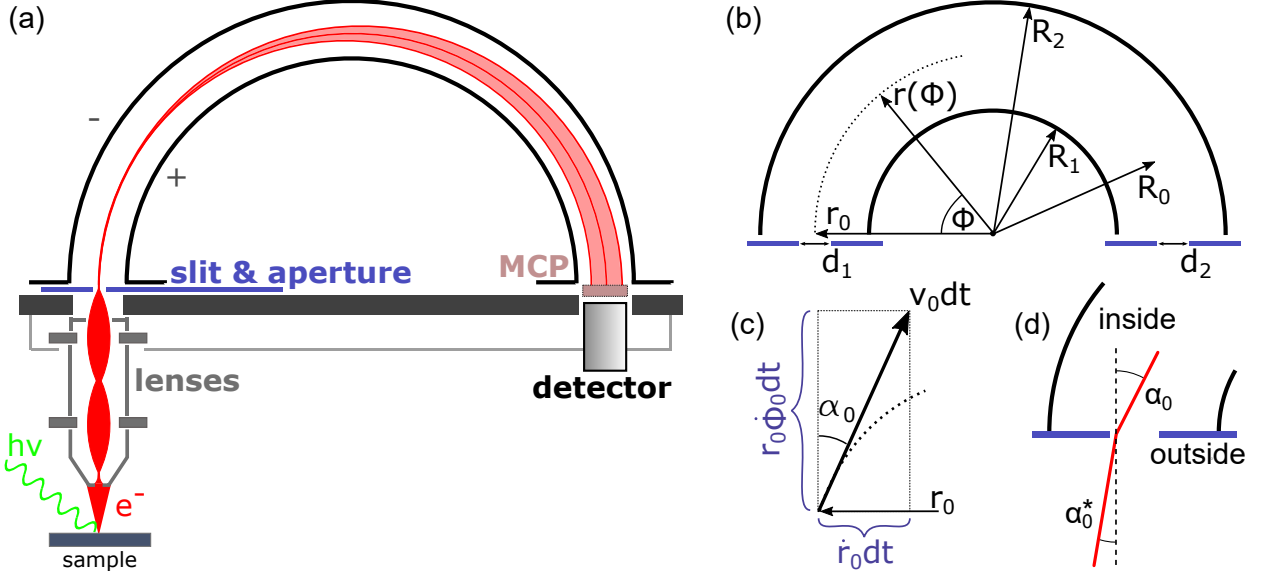


Figure 5.1: (a) Schematic view of a hemispherical deflection analyzer with a two-dimensional detector consisting of an MCP and a DLD. Photoelectrons being emitted from the irradiated sample, are collected by the entrance lens, de- or accelerated to E_{pass} and detected by the DLD. By variation of the voltage of the lens system an energy spectrum is being measured. (b) Corresponding coordinate system. (c) Starting angle α_0 expressed by the radial (\dot{r}) and angular ($\dot{\phi}$) velocity. (d) Refraction of an electron while entering the HDA: Transition from a constant potential U_0 outside (with angle α_0^*) to the spherical potential $U \propto 1/r$ inside the analyzer (with angle α_0).

The motion of the electrons within the analyzer is determined by the $1/r$ potential of the spherical electrodes, which can be written as:

$$U(r) = U_0 \frac{R_0}{r}, \quad (5.6)$$

with the mean radius $R_0 = 1/2(R_1 + R_2)$ of the analyzer. Inserting now the Eqs. 5.6 and 5.5 into Eq. 5.1 gives the definition of the electron's motion within a hemispherical analyzer:

$$E_{\text{tot}} = \underbrace{U_0 \frac{R_0}{r} + \frac{L^2}{2m_e r^2}}_{U_{\text{eff}}} + \frac{m_e}{2} \dot{r}^2, \quad (5.7)$$

where the first two terms are often referred to as the effective potential U_{eff} . This equation can be simplified for a circular orbit where $r = r_0$. Due to the conservation of energy $dE_{\text{tot}}/dr = 0$, one gets $\dot{r} = 0$ and $\dot{\phi} = \text{const.}$ and it follows:

$$\left. \frac{dU_{\text{eff}}}{dr} \right|_{r=r_0} = 0 \quad \Leftrightarrow \quad -U_0 \frac{R_0}{r_0^2} - \frac{L^2}{m_e r_0^3} = 0. \quad (5.8)$$

The angular momentum L can be replaced by using Eq. 5.5 assuming a constant kinetic energy T_0 :

$$U_0 = -2\frac{r_0}{R_0}T_0. \quad (5.9)$$

Considering electrons entering the analyzer under normal incidence ($\alpha_0 = 0$) with a kinetic energy T_0 , they pass through the hemispherical analyzer on a circular trajectory with radius $r_0 = R_0$ and are detected at the exit. This kinetic energy is referred to as the pass energy E_{pass} of the analyzer and with $T_0 = E_{\text{pass}}$ the value of the electrode potentials is given by:

$$E_{\text{pass}} = -\frac{U_0}{2}. \quad (5.10)$$

Assuming a finite mean width $D = (d_1 + d_2)/2$ of the slits in radial direction at $\phi = 0^\circ$ and $\phi = 180^\circ$ and allowing for electrons with incident angles of $\alpha_0^* > 0$ to enter the analyzer, the energy resolution of an HDA is given by [179]:

$$\Delta E = E_{\text{pass}} \left(\frac{D}{2R_0} + \alpha_{0,\text{max}}^{*2} \right). \quad (5.11)$$

Thus, the α^2 -aberration is a major limitation of the resolution of an HDA and according to the *Kuyatt-Simpson criterion*, the $\alpha_{0,\text{max}}^{*2}$ -term should not exceed 0.5 times the “slit”-term $D/2R_0$ [180]. This limits the incident angle in a conventional high resolution HDA typically to $1.5^\circ - 3.0^\circ$ [179]. The angle of incidence β of the electrons in the non-dispersive direction (perpendicular to the dispersive direction) does not contribute to the energy resolution since they travel on equatorial circles (for $\alpha_0 = 0$) or on identical ellipses (for $\alpha_0 > 0$). A more detailed discussion of the α^2 -aberration as well as the *sphere aberration*, taking also the exit angle of the electrons into account, can be found in Refs. [179, 181].

It can also be seen from Eq. 5.11 that, if the photoelectrons pass through the analyzer with their initial kinetic energy E_{kin} , the energy resolution varies over the spectrum. Thus, for a constant energy resolution throughout the spectrum, the energy of the photoelectrons has to be kept at a constant pass energy E_{pass} . This is achieved by the remaining lenses, which accelerate or retard the electrons to E_{pass} before they enter the hemisphere. By sweeping the retarding voltage of the analyzer lens in small intervals ΔE , electrons with different E_{kin} can be successively de- or accelerated to E_{pass} , fly through the analyzer and are counted at the exit by the DLD. In that way, an energy spectrum over several 100 eV or even several 1000 eV, depending on the excitation source, can be acquired. This analyzer operation is the so-called *constant analyzer energy* (CAE) mode. When using a two-dimensional electron detector, here a combination of an MCP and DLD, an energy window of $\approx 10\%$ of E_{pass} is measured [182], since electrons with slightly more and less kinetic energy than E_{pass} , which are slightly less and more deflected within the hemisphere, are still being detected due to the two-dimensional detector area. This, in combination with Eq. 5.11, leads to higher count rates when E_{pass} is increased, while the energy resolution is decreased. Similar principle applies for the choice of the entrance slit. While a narrow slit reduces the count rates significantly, it allows for high energy resolution measurements and vice versa. A smaller d

also reduces the spherical aberration of the analyzer's dispersion, which is determined by the α^2 -term [183]. While using the CAE mode, one can—beside the described *sweeping* mode—also use the *imaging* or *fixed* mode. When measuring in the fixed mode, the retarding potentials are kept constant and only the small energy window $\approx 10\%$ of E_{pass} is measured. This allows for quite a fast acquisition of a small energy spectrum since no time is needed to shift the potentials and wait for them to become stable. A disadvantage of this method is the not necessarily homogeneous electron sensitivity of the detector surface. Since in sweep mode the complete spectrum of electrons is shifted in the dispersive direction across the detector, inhomogeneities—which mainly originate from the MCP—will be averaged out. But when acquiring a constant energy window the problem persists. The most common solution for this is to measure a constant background in fixed mode, which includes all detector inhomogeneities and divide the acquired spectrum by this background.

When operating in this CAE mode, HDAs have an energy dependent transmission function T , which describes the ratio of the initial number of electrons entering and the number of electrons being detected and counted by the detector for a given kinetic energy. Hereby, the determination of T is quite complicated and there are several different approximations [184]. Depending on the geometry of the lens system, the transfer function can be quite simple or more complex and can vary greatly among different analyzer models.

To get rid of this energy dependent transmission, another analyzer operation mode was established, the *constant retard ratio* (CRR) mode. Using this mode, electrons entering the lens system are retarded by a constant proportion of their kinetic energy, which is described by the retard ratio k :

$$k = \frac{E_{\text{kin}}}{E_{\text{pass}}}. \quad (5.12)$$

Throughout the scan range, the pass energy is continuously varied to keep a constant retard ratio. Therefore, the transmission function is constant for all initial kinetic energies, but the energy resolution varies over the energy spectrum. In Fig. 5.2 two photoemission spectra of a gold foil are shown, which were acquired with the same analyzer in the two different operation modes CAE and CRR. While using the CAE mode, a broad background increases in intensity toward lower kinetic energies, which originates from a higher transmission for slower electrons, there is no such a background when using the CRR mode since the transmission function is constant over the entire energy range. Which of the two modes is to prefer, depends on the data one is interested in. All measurements done in this study in combination with an HDA were performed exclusively in the CAE mode, to ensure a constant energy resolution.

External Spin Detector

The principles of multichannel spin-filtering were already discussed in Sec. 4.4.3. Now the technical implementation in combination with an HDA is discussed in detail.

The spin detector is built in 90° geometry and is directly attached to the exit of the hemispherical analyzer as can be seen in Fig. 5.3. This design results in a scattering angle of 45° at the W(001) spin-filter crystal. The two-dimensional electron distribution at the exit

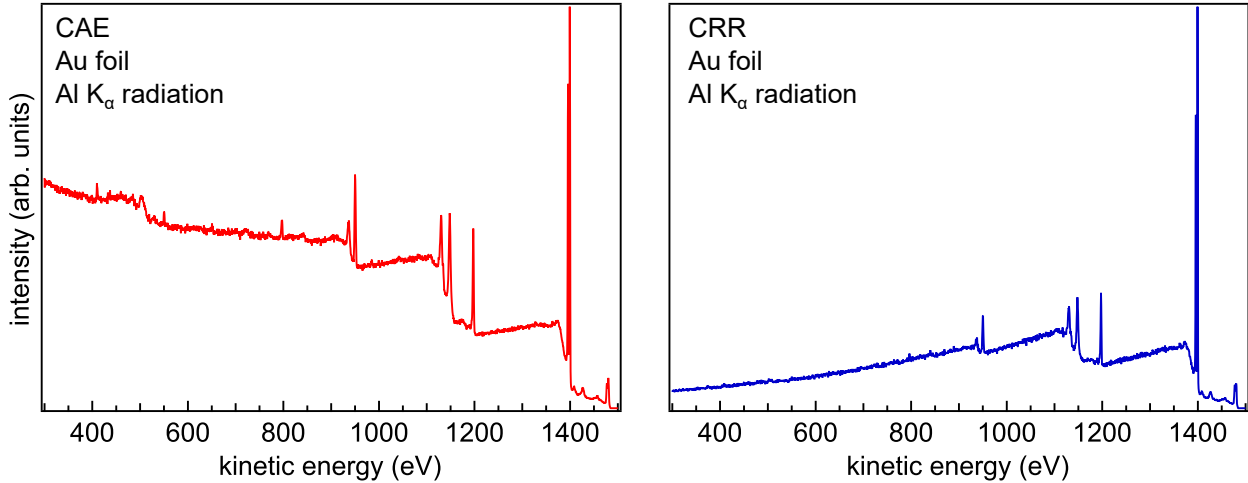


Figure 5.2: Photoemission spectra of a Au foil (excitation source Al K_{α}) measured with the CAE (left) and CRR (right) mode.

of the analyzer is transferred through the spin detector, scattered at the spin-filter crystal and afterwards detected by the DLD at the end of the spin detector chamber. For a proper imaging within the spin detector, several different lens types are built in. At the entrance, a quadrupole provides centering of the photoelectrons entering the detector at an angle of about 5° with respect to the dispersive direction. This quadrupole is followed by cylindrical, conical, and focusing lenses that first invert the image and then provide parallelization of the electron beam. It is important that the electrons are not focused on the crystal as this would lead to many different scattering angles and therefore strongly varying asymmetry and reflectivity values for each electron. Directly before and after the spin-filter crystal a second set of quadrupoles is installed to center the parallel electron beam on the spin-filter crystal and finally on the detector. The spin-filter itself is mounted on a rotary feedthrough allowing for proper alignment of the crystal relative to the scattering plane.

Since the cleanliness of the spin-filter surface also depends on the vacuum conditions within the chamber, the spin detector is further equipped with its own turbo molecular and non-evaporable getter pump granting a chamber pressure in the low 10^{-10} mbar region (see also Sec. 5.1.2).

A detailed view of the electron trajectories within the spin detector and the corresponding lens potentials is shown in Fig. 5.4. The electrostatic fields are represented by black (+) and blue (−) field lines. The spin-filter crystal (gray) is located at the center of the scattering volume (including the crystal and all parts in the direct vicinity, see also Fig. 5.3) to which the scattering potential U_{SV} is applied to. To grant a parallel incidence of the photoelectrons to the crystal surface, two focus points are situated directly in front and after the scattering volume. All lens potentials are floating on the Herzog potential of the HDA. In sweep mode this allows the lens potentials of the spin detector to simultaneously change with the HDA. As discussed in Sec. 4.4.3, the electrons entering the spin detector with a kinetic energy of E_{pass} have to be decelerated to a specific scattering energy, at which asymmetry and reflectivity should both be as high as possible. For the here used 45° scattering angle and a

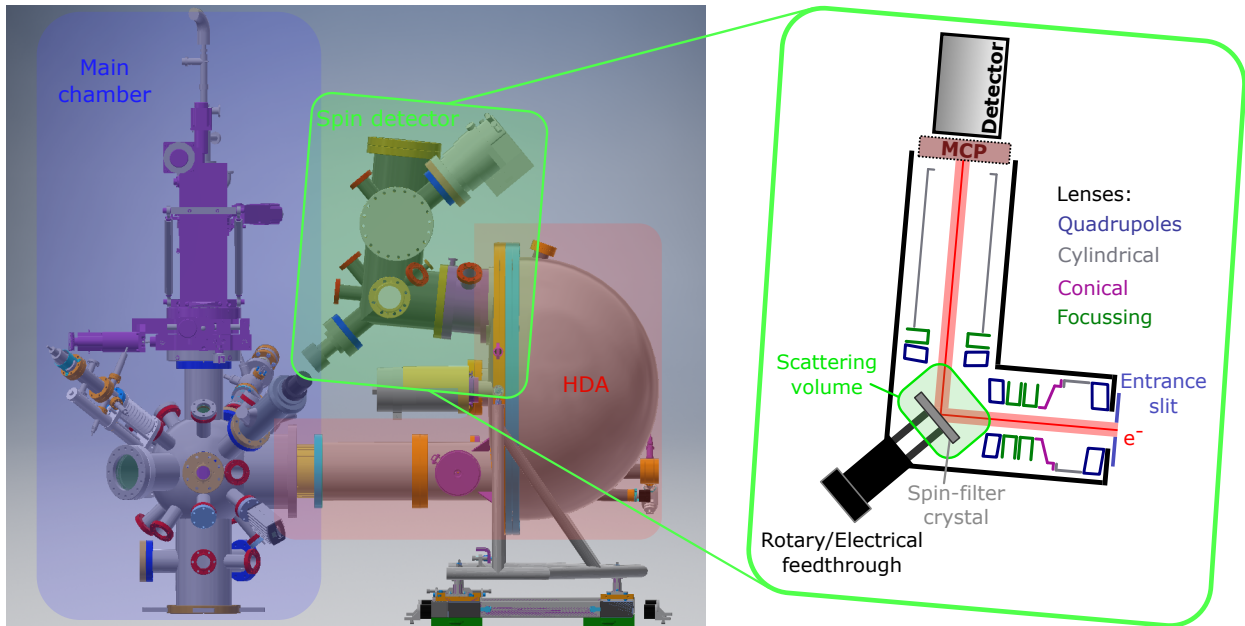


Figure 5.3: Schematic view of the experimental setup consisting of the main chamber, with the mounted sample, the HDA, and the connected spin detector. On the right side the design of the electrostatic lenses within the detector is shown.

W(001) spin-filter crystal, the energy dependent reflectivity (red), Sherman function (blue), and FoM (green) is shown in Fig. 5.5 [175]. There are two local maxima of the reflectivity visible at scattering energies of 25.2 eV and 30.5 eV. For the Sherman function only one maximum can be determined at $E_{\text{scatt}} = 26.5$ eV, which is slightly beside the first reflectivity maximum. For the second maximum of the reflectivity there is a local minimum in the Sherman function at $E_{\text{scatt}} = 30.5$ eV, defining the only suitable working point of the spin detector at a scattering energy of 26.3 eV, at which the FoM exhibits its maximum. Therefore, by setting the potentials of the scattering volume to $U_{\text{SV}} = E_{\text{scatt}} - E_{\text{pass}}$, the desired scattering energy of the photoelectrons can be adjusted. Here, for a given pass energy of 90 eV, this results in a nominal deceleration potential of $U_{\text{SV}} = 26.3 \text{ eV} - 90 \text{ eV} = -63.7 \text{ eV}$.

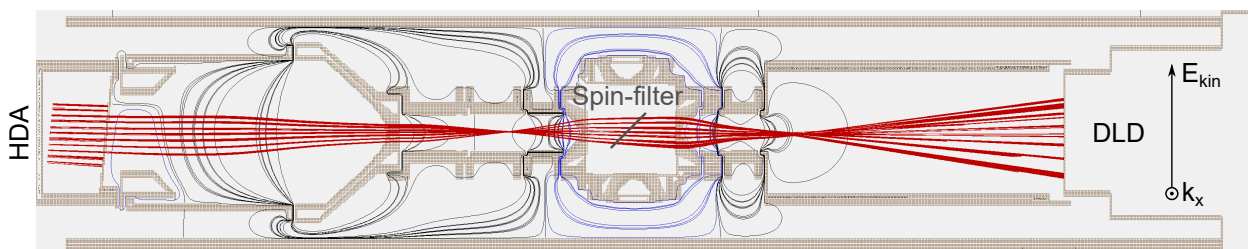


Figure 5.4: Electrostatic lens potentials of the spin detector in the dispersive direction, showing the equipotential lines (black(+)) and blue(-)), the electron trajectories (red) and the spin-filter crystal (gray).

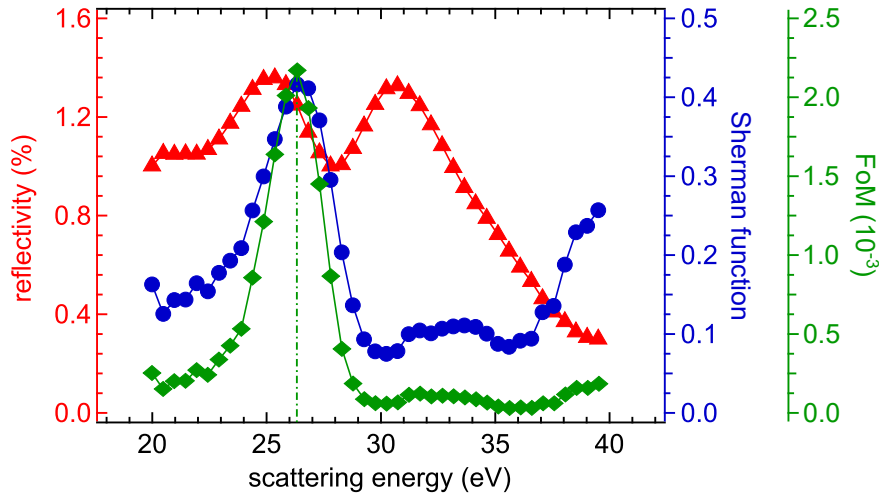


Figure 5.5: Energy dependent reflectivity (red), Sherman function (blue), and the resulting FoM (green) of a W(001) crystal for a 45° scattering angle, showing two maxima for the reflectivity at 25.2 eV and 30.5 eV, and one local maximum for the Sherman function at 26.5 eV, defining the suitable working point of the spin-filter crystal with the maximum FoM at about 26.3 eV (dashed line) [175].

While being scattered at the spin-filter crystal, the photoelectrons generate secondary electrons by inelastic scattering, whose kinetic energy is far below that of the photoelectrons. Due to the generally low count rates, originating from the low reflectivity of $\approx 1\%$, an inelastic background in the energy spectra can make spin-filtered photoemission even more complicated. Therefore, a grid is installed directly in front of the MCP, acting—by applying a negative voltage—as a suppressor for the low energy electrons, increasing the signal-to-noise ratio.

After introducing the fundamentals of spin-resolved HAXPES with an HDA using a W(001) spin-filter crystal in 45° scattering geometry, the following sections show the first measurements, to characterize this newly built spin detector.

5.1.2 Spin-Filter Surface Preparation

As the scattering energies of the photoelectrons in the spin detector are in the range of several 10 eV, as shown in Sec. 4.4.3, the scattering process at the spin-filter crystal is extremely surface sensitive, setting very high demands to a proper surface preparation [185]. Higher scattering energies are thereby not applicable since the reflectivity as well as the asymmetry of the spin-filter crystal strongly decrease for scattering energies higher than 50 eV. Therefore, a cleaning procedure has to be followed yielding an atomically clean crystal surface. Here, the two-step flashing procedure of Zakeri *et al.* [186] was adapted to our setup and will be further discussed in the following section. Although this procedure was introduced for the preparation of clean W crystal surfaces, it is also applicable for other refractory metals like Mo, Re, and Ir. The success of the preparation process is monitored by LEED and a residual gas analyzer (RGA).

5.1.2.1 Two-Step Flashing Procedure

The most common contaminations of tungsten surfaces are carbon and oxygen. The idea of this cleaning procedure is a two-step flashing process. The first step are a few cycles of low power flashes (LPF) where the heating—realized by electron bombardment from the back, which is integrated into the crystal holder—, illustrated in Fig. 5.6, is switched on for 15 s followed by a break of 100 s. Applying a high voltage of $U_{\text{HV}} = 1.2 \text{ kV}$ to the crystal and a filament current of $I_{\text{F}} = 5.6 \text{ A}$ realizes an emission current $I_{\text{E}} = 40 \text{ mA}$ ($P = 48 \text{ W}$), which leads to a crystal temperature—measured from the front via a pyrometer—of about $1000 \text{ }^\circ\text{C}$ at the end of each LPF. The idea of this step is the segregation of carbon from the bulk onto the crystal's surface [187–189]. Since these LPFs are performed at an oxygen partial pressure of $p_{\text{O}_2} = 5 \cdot 10^{-8} \text{ mbar}$, the segregated carbon shall react at the surface forming volatile CO [190, 191] and subsequently desorb.

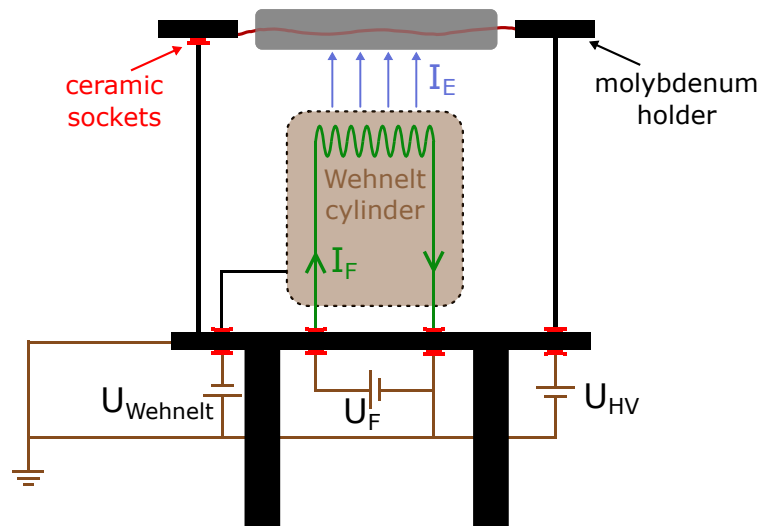


Figure 5.6: Schematic illustration of the crystal holder with integrated electron bombardment heating: The tungsten spin-filter crystal (gray) is held in place by tungsten wires (dark red). Below the crystal the filament is wrapped in a tantalum foil working as a Wehnelt cylinder. A high voltage U_{HV} can be applied to the crystal. With a filament current I_{F} of several Ampere the crystal temperature can rise up to $2500 \text{ }^\circ\text{C}$.

To monitor the effectiveness of the cleaning procedure, the ultrahigh vacuum (UHV) chamber in which the cleaning is performed, is equipped with an RGA, measuring the ion current of carbon monoxide and oxygen during the LPF cycles. On the left side of Fig. 5.7 the RGA spectrum of 8 LPF cycles is plotted, showing the relative intensities of CO (red) and O_2 (blue) during the cycles, respectively. A general decrease of the overall CO intensity can be seen from the beginning to the end. During each flash, a slight decrease of the O_2 intensity is visible when the filament current is switched on since a part of the molecules are cracked by the heat of the filament and reacts with carbon atoms to form the desorbing CO. On the right side of Fig. 5.7 the CO signals of the first, second, third, and sixth cycles

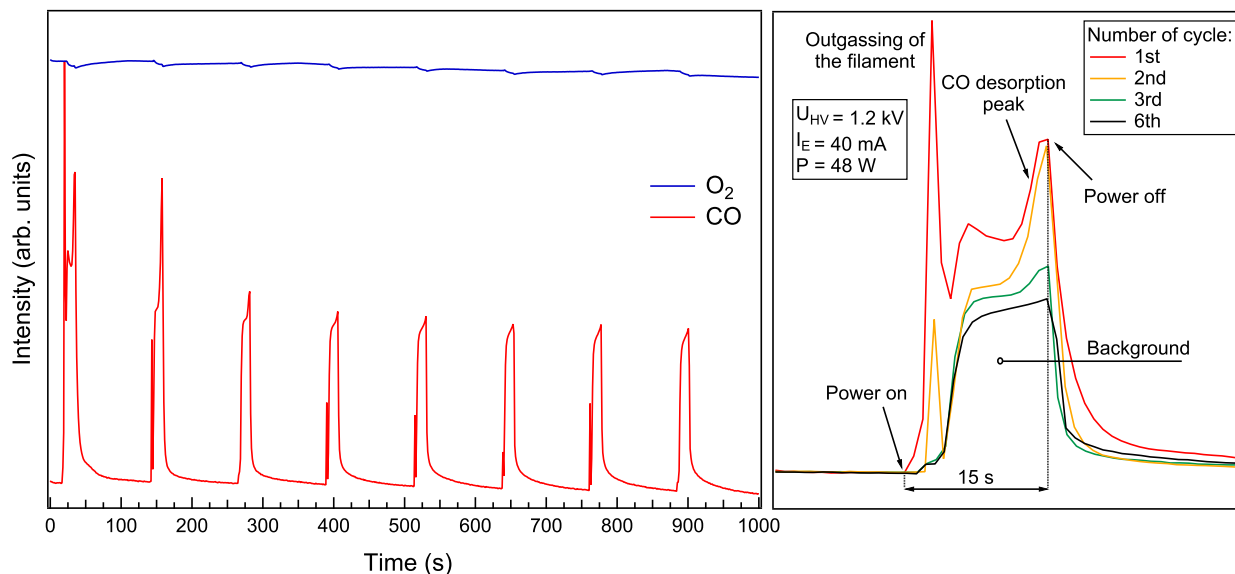


Figure 5.7: Left: RGA spectra of CO and O₂ during 8 LPFs. Right: Comparison between the first, second, third, and sixth flash. The intensity of the filament peak as well as of the CO peak from the surface is clearly decreasing with further flash cycles. The last one is completely vanished after the sixth flash.

are compared to each other in detail. For each flash, two peaks can be distinguished from a nearly flat background signal. The first sharp peak belongs to the outgassing filament since this is the first part to heat up. The second peak originates from CO desorbing from the crystal surface. Since also the temperature of the molybdenum holder slightly rises, there is also a nearly flat background during each LPF which decreases very fast after powering off the heater. While the first peak vanishes already after the first two LPFs, the second peak decreases more slowly and it needs about 6 flashes until the second peak has also completely vanished. After the LPF cycles the oxygen leak valve is closed and the system is pumping down to a base pressure of about $3 \cdot 10^{-10}$ mbar again.

During the first step, also a layer of tungsten oxide forms at the surface of the spin-filter crystal, which to remove needs higher temperatures of about 1200 °C [192–194]. To get also rid of the remaining atomic oxygen on the surface, a much higher temperature of up to 2000 °C must be reached [195, 196]. Therefore, a second step is necessary, which is a single high power flash (HPF) performed in the residual gas atmosphere. With an emission current of 240 mA ($P = 288 \text{ W}$) the crystal is heated up to 2000 °C within 10 s. Afterwards, the system cools down and remains at base pressure.

Note that this two-step procedure only works if the crystal has not been previously exposed to air. For the treatment in this case see Appendix for further information.

5.1.2.2 Electron Diffraction Study of the Surface

Although no carbon shoulder is visible after 6 LPFs, a small amount of carbon may still have remained on the surface, but below the detection limit of the RGA. To verify the atomic cleanliness of the spin-filter crystal's surface, LEED gives detailed information of a long

range order of the upper most atomic layers. Since tungsten crystallizes in a body-centered cubic (bcc) lattice structure, the unreconstructed surface of W(001) in reciprocal space is a cubic (1x1) pattern.

Ollis and Boudart [197] and later Benzinger *et al.* [198] studied the impact of surface carburization of W(001) single crystals by LEED. An overview of their findings is illustrated in Fig. 5.8. As mentioned above, a cubic (1x1) pattern is expected for the unreconstructed clean W(001) surface (a). A $1/2$ monolayer coverage with carbon produces a c(2x2) reconstruction with a carbon atom density of $5.0 \cdot 10^{14}$ atoms/cm² (b), while for a $2/3$ coverage a $\begin{pmatrix} 3 & 0 \\ 1 & -1 \end{pmatrix}$ ⁱ structure is expected, representing a carbon density of $6.7 \cdot 10^{14}$ atoms/cm² (c). For even higher carbon densities of $1.0 \cdot 10^{15}$ atoms/cm² a (6x1) reconstruction is observed (e) and for $1.2 \cdot 10^{15}$ atoms/cm² a (5x1). The latter can be interpreted as a (0001) ditungsten carbide W₂C overlayer on the W(001) surface [197, 200].

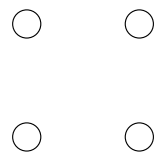
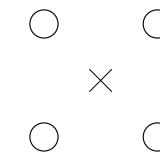
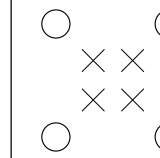
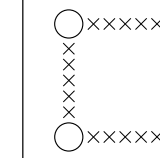
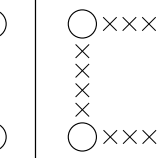
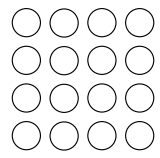
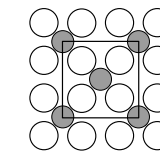
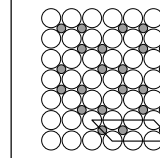
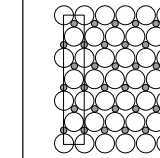
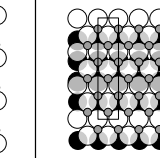
reconstruction	(a) (1 × 1)	(b) c(2 × 2)	(c) $\begin{pmatrix} 3 & 0 \\ 1 & -1 \end{pmatrix}$	(d) (6 × 1)	(e) (5 × 1)
LEED pattern					
real space					
carbon atom density	0	$5.0 \cdot 10^{14}$	$6.7 \cdot 10^{14}$	$1.0 \cdot 10^{15}$	$1.2 \cdot 10^{15}$

Figure 5.8: Overview of different LEED patterns and the corresponding real space lattice and carbon density in atoms/cm² for a W(001) surface. White: tungsten, grey: carbon, black: tungsten second layer. Adapted from Ref. [198].

After the first 10 LPFs at 950 °C in an oxygen atmosphere of $p_{O_2} = 5 \cdot 10^{-8}$ mbar and the subsequent HPF at 2000 °C, the LEED pattern at an energy of 120 eV is shown in Fig. 5.9(a). Surprisingly, the (1x1) reconstruction for the clean W(001) surface is not seen, but instead the (6x1) reconstruction is visible, indicating a high carbon density on the crystal's surface. This makes clear that the temperature during the LPFs was too low, since apparently not all carbon atoms have desorbed. On the other hand, the temperature should not be higher than needed to keep the pressure rise during a single LPF as low as possible and to prevent the heater surrounding to heat up. Thus, the LPF temperature is now increased by 50 °C—while all other parameters stay the same—and another LEED pattern is taken, which is shown in (b). The reconstruction can easily be identified as $\begin{pmatrix} 3 & 0 \\ 1 & -1 \end{pmatrix}$, indicating that the remaining

ⁱThe matrix notation suggested by Park and Madden [199] is employed here.

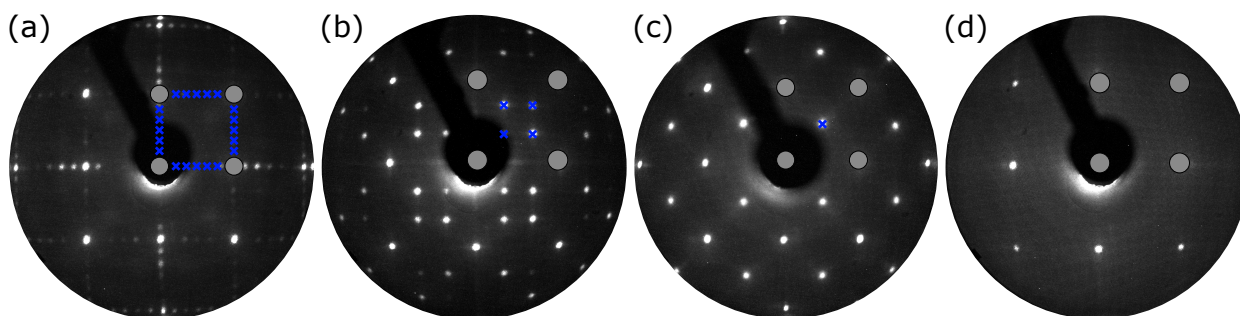


Figure 5.9: LEED patterns recorded after a full cleaning cycle (10 LPFs + 1 HPF) with different temperatures during the LPF: (a) 950 °C, (b) 1000 °C, (c) 1050 °C, and (d) 1100 °C. Temperature during HPF was 2000 °C for all LEED patterns, which were recorded at an energy of about 120 eV. The grey dots represent the (1x1) tungsten lattice, while the blue crosses indicate the surface reconstruction originating from different carbon atom densities.

carbon on the surface is now less than before, but still significant. A further increasing of the LPF temperature by 50 °C leads to the next LEED pattern shown in (c). The reconstruction changed to a $c(2 \times 2)$, representing the second least carbon coverage. Finally, after increasing the flash temperature to 1100 °, the (1x1) reconstruction of a pure and atomic clean W(001) surface can be seen (d).

Due to the lack of any characterization methods of the spin-filter surface when mounted in the experimental setup, it has to be ensured, that the determined parameters for a successful surface preparation can be easily reproduced.

5.1.3 First Measurements and Characterization

After the surface treatment of the crystal, it has to be characterized, in particular the exact working parameters have to be determined. First, the optimum working point with the maximum FoM will be evaluated followed by a study of the crystal's surface lifetime in order to get an estimate for how long single measurements can run before the crystal has to be flashed again. With these parameters, the imaging capabilities—mainly given by the lens potentials—will be optimized to finally proceed to the first spin-resolved measurements of the valence band of magnetite. Afterwards, possible sources of errors and further need for optimization will be discussed.

Determination of the Working Point

Although the reflectivity and asymmetry of W and Ir spin-filter crystals have already been investigated [146, 175], for each setup and single crystal the exact energetic position of the working point has to be determined individually prior to any photoemission experiment (the literature data only serve as good starting parameters). For this, a magnetite sample was transferred into the main chamber, irradiated with high-energy synchrotron light of several keV, and the intensity of the O 1s core level was measured while changing continuously the scattering energy. The maximum intensity of the core level (determined by Gauss fittings) was then plotted as a function of scattering energy in Fig 5.10 and compared to the literature

(see Fig. 5.5 and Ref. [175]). Both curves show two local maxima each, which are slightly shifted against each other. While the value from the literature for the first reflectivity maximum (here the one at lower scattering energies) is at about 25.2 eV, the experimentally determined value for the used W(001) spin-filter is shifted by about 0.4 eV to higher scattering energies. This can be explained by a different work function of the spin-filter crystal, as well as by small deviations between the set potential for the scattering volume and the actual applied voltages, which depends on the individual experimental setup. As already mentioned before, in the literature the favoured working point is at about 26.5 eV and therefore at the maximum of the FoM—1.3 eV above the maximum of the reflectivity (see Fig 5.5). Thus, in our experiment—with the reflectivity maximum shifted by 0.4 eV—the working point is also shifted by the same value and is therefore at about 26.9 eV. Despite the observed small shift compared to literature, the data are overall in good agreement.

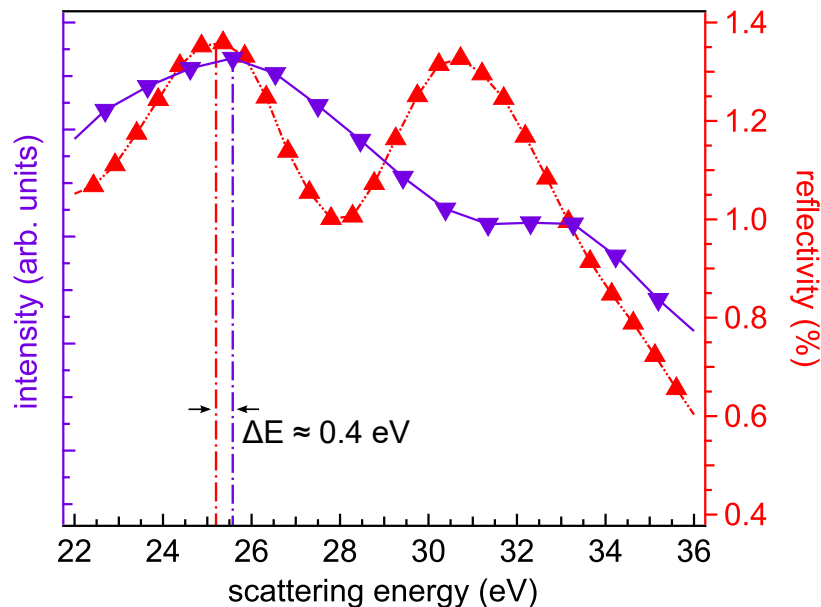


Figure 5.10: Measured intensity reflected from the W(001) spin-filter crystal as function of scattering energy (purple) in comparison with the determined reflectivity by Tusche *et al.* [175] (red).

Impact of Adsorbates on the Reflectivity

Due to the surface sensitive scattering, the adsorption of nitrogen and carbon compounds as well as the oxidation of the topmost tungsten layer play an important role, since these effects can have a significant impact on the temporal stability of the reflectivity and asymmetry of the spin-filter crystal—often referred to as lifetime of the surface. This lifetime determines the possible acquisition time of a measurement before the crystal has to be flashed again to restore its initial FoM. To characterize the lifetime, again the maximum of the O 1s core level was measured in equidistant time intervals for over three hours after the crystal surface had been freshly prepared. Figure 5.11 (a) depicts a selection of the acquired O 1s spectra, showing a decreasing intensity over time. The relative intensity I/I_0 of each core

level spectrum is shown as a function of time in Fig. 5.11 (b). Already during the first 30 minutes the reflected intensity decreases significantly and slowly stabilizes at about 90% after 90 minutes. Likewise, a significant decrease is to be expected for the asymmetry. These measurements reflect the extremely short lifetime of the W(001) crystal surface [146]. Individual measurements should last no longer than about 20 minutes to ensure that the reflected intensity and asymmetry do not change during the measurement due to a degrading crystal surface. Such intensity differences could later be misinterpreted as asymmetry effects during the evaluation of the acquired data.

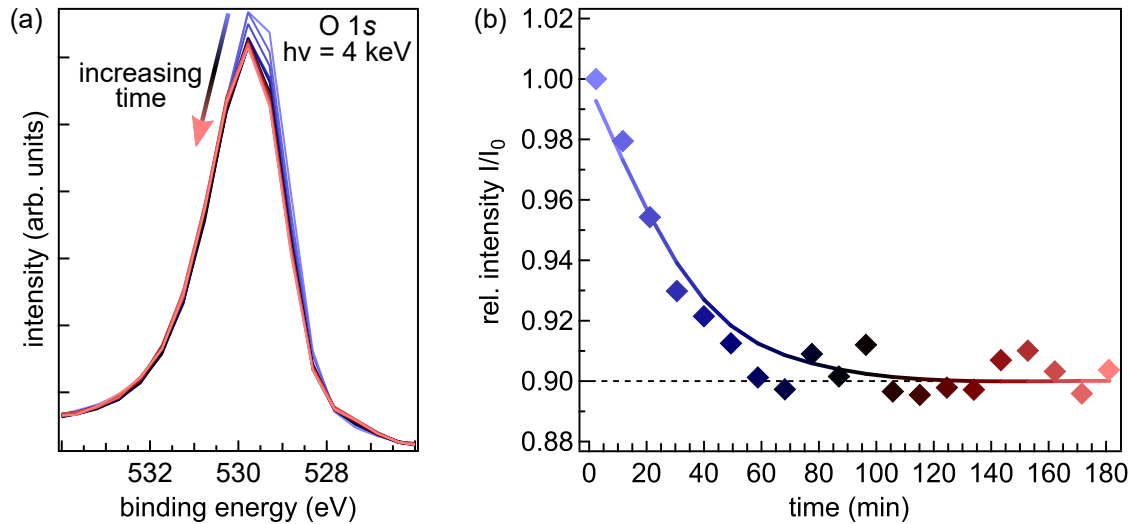


Figure 5.11: Stability of the reflectivity measured with the maximum intensity of the O 1s core level of magnetite over time.

A measure for the amount of adsorbates within a vacuum system is the unit Langmuir L :

$$1L = 1.33 \cdot 10^{-6} \text{ mbar} \cdot \text{s}. \quad (5.13)$$

This means, at a pressure of $1.33 \cdot 10^{-6}$ mbar a monolayer on the surface each second, if the sticking coefficient is 1. The measurements here were performed at a base pressure of about $4 \cdot 10^{-10}$ mbar and—taking into account the sticking coefficient for tungsten of about 0.7 [201]—the time for the adsorption of a single monolayer on the crystal’s surface is about 80 minutes. This is in good agreement with our findings since the reflectivity stabilizes after this period of time making clear, that the first monolayer has the most tremendous impact on the reflectivity of the tungsten spin-filter crystal.

Optimizing the Imaging Capabilities

After determining the best suitable working point of the spin detector, the two-dimensional imaging capabilities are being optimized by adjusting the different available deflector and focussing lenses. While the previous measurements were carried out using the scanning mode of the analyzer, during the first tests of the fixed mode it was found that the detector image of, e.g., the O 1s core level, shown in Fig. 5.12 (a), exhibits a strong reduced count

rate towards higher detection angles θ . The spectra show the intensity of the photoelectrons integrated over the kinetic energy (blue) and detection angle (green). Also, the overall count rate for such a bright core level is only moderate, even when considering the low reflectivity of the spin-filter crystal. This would become even worse when measuring the valence band. Furthermore, a slight asymmetry between the high and low energy side of the peak is visible, which can be referred to the transmission function of the analyzer.

To further optimize the imaging capabilities and count rates, first the pass energy of the HDA was raised to 150 eV, and also the lens potentials were adjusted in several iteration steps. By using a gold foil and measuring the $4f$ core level—shown in Fig. 5.12 (b)—, the now optimized detector image exhibits an essentially constant intensity in the non-dispersive direction. By the known spin-orbit splitting of this core level of 3.7 eV the usable energy window on the detector can be determined to be about 5 eV. Normally for a pass energy of 150 eV an energy window of about 15 eV can be expected, but due the fact that the area of the spin-filter is way smaller than the detector area, especially when seen under an angle of 45° , the energy window is significantly reduced.

With the new lens settings, the dispersive direction of the detector can now be calibrated by shifting the O $1s$ core level by 1 eV and measuring the distance the peak moved on the detector, which results in a relation between dispersive direction (in mm) and kinetic energy of $2.15 \frac{\text{mm}}{\text{eV}}$.

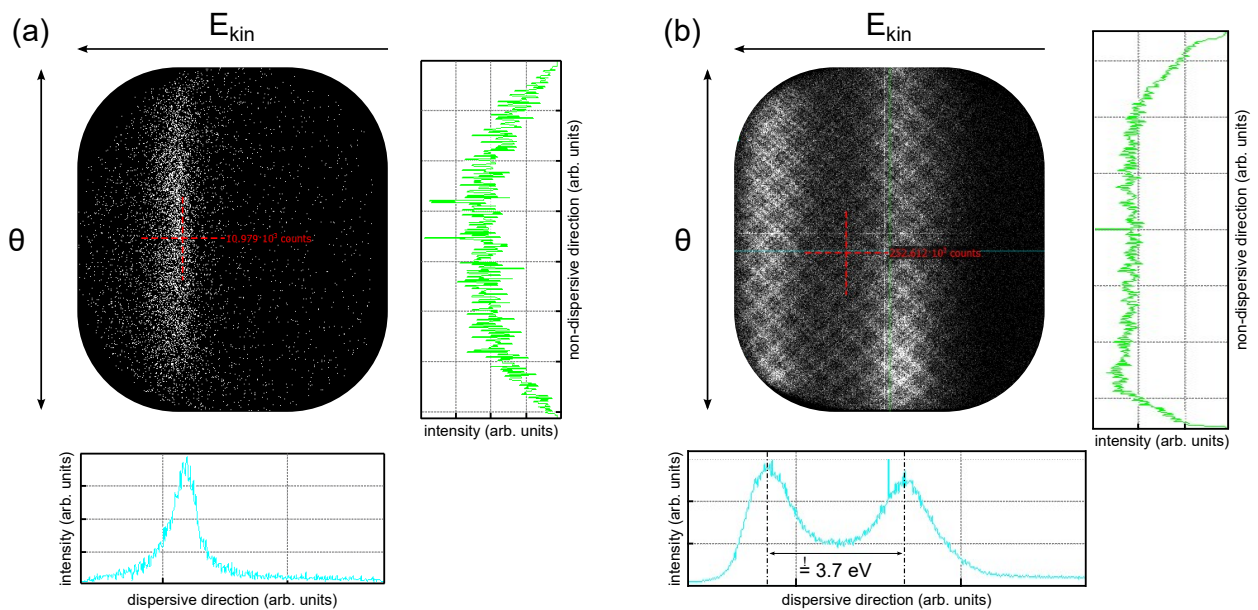


Figure 5.12: Detector image of the (a) O $1s$ core level prior to any optimization of the lens potentials and (b) Au $4f$ core level after a few adjustments. The integrated intensities in the dispersive and non-dispersive direction are shown as blue and green line, respectively.

Determination of the Detector Background

While the imaging mode allows for faster acquisition and higher count rates, the problem of a varying spatial sensitivity of the MCP as well as the changing transmission function of the analyzer at higher kinetic energies can have impact on the spectral line shape, especially within the valence-band range, since the signal-to-noise ratio is strongly reduced. To measure the influence of the MCP and the transmission function of the analyzer with the spin detector attached, the spectral region between two core levels exhibiting a constant background signal was measured, which is shown in Fig 5.13. The photoelectron intensity thereby covers a range of about 5 eV as mentioned before and shows a slightly decreased intensity on the high energy side. There is also a grid visible in the detector image which is rotated by 45° with respect to the dispersive direction and originates from the suppressor grid which is installed right in front of the MCP to reduce the secondary electron count rate.

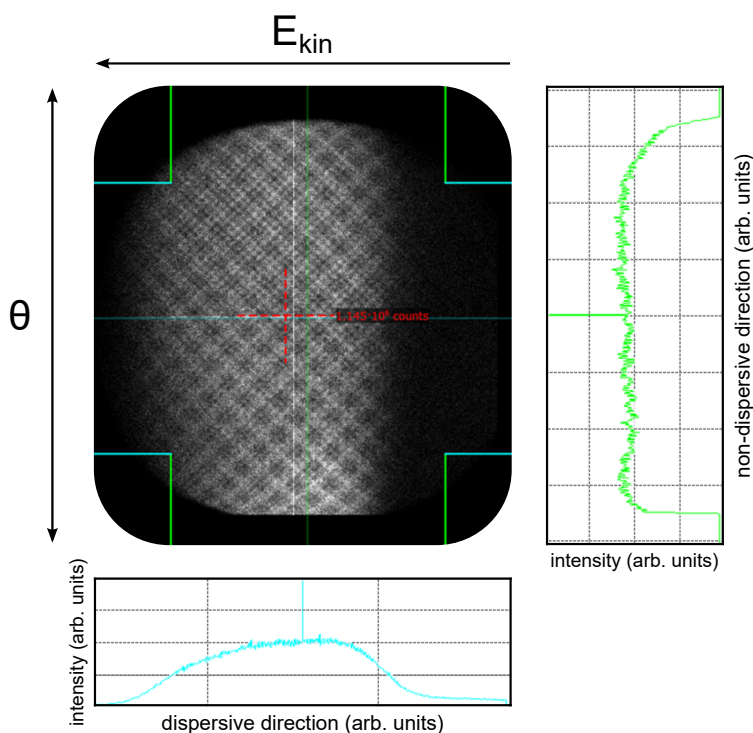


Figure 5.13: Detector image of a flat photoelectron background reflecting the inhomogeneities of the MCP and the transmissions function of the HDA.

Spin-resolved Valence Band of Magnetite

After characterizing the spin-filter crystal, determining the most suitable scattering parameters, and optimizing the imaging capabilities, the first spin-resolved measurements were performed on magnetite in imaging mode. A 30 nm $\text{Fe}_3\text{O}_4(001)$ thin film was epitaxially grown on MgO as described in Ref. [202]. The sample was magnetized using a strong permanent magnet and the valence band was measured with a fixed energy windows at different

kinetic energies to cover the whole valence band (about 10 eV wide)ⁱⁱ. Each data set consists of two measurements with the sample magnetized in-plane in opposite direction with respect to the quantization axis of the spin detector. Due to the short lifetime of the crystal's surface, the spin-filter was flashed prior to each single measurement. In total four data sets were acquired at binding energies (marking the center of the acquired detector image) of 2, 4, 6, and 8 eV. The results including the determined asymmetry (see Eq. 4.36) are shown in Fig. 5.14.

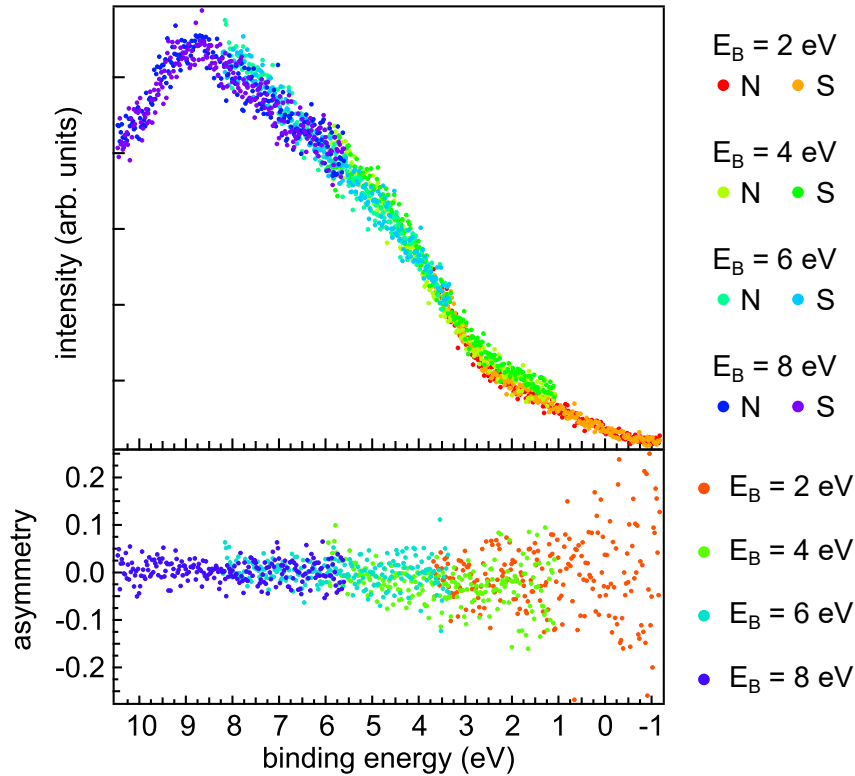


Figure 5.14: Different sets of two measurements—each with opposite magnetization directions— at different binding energies with the resulting asymmetry.

In view of the statistical errors—increasing towards E_F due to the decreasing signal-to-noise ratio—the overall asymmetry is zero, although the reflectivity of the crystal was thoroughly characterized for different scattering energies, and also the energy dependent Sherman function of the crystal and thus the FoM were determined according to the literature values. The same set of measurements was carried out also for slightly different scattering energies to take any energetic shift of the Sherman function of the used crystal into account, but no asymmetry could be measured. Another possible source of uncertainty is the azimuthal angle as described in Sec. 4.4.2. But also for measurements at slightly different azimuthal angles no asymmetry could be observed for the valence band of magnetite. The reason

ⁱⁱNote: Although the sweep mode can cover the whole acquired range in one measurement, the fixed mode grants for the first test measurements a more reliable result. This is because sweeping the analyzer voltages, and thus the detector voltages, can cause an inaccuracy—avoidable at this point in the detector's commissioning—if the potentials are not changed at exactly the same time.

for the lack of any observable asymmetry might be related to further problems of the spin detector like the reproducibility of consecutive measurements and the overall experimental resolution, which will be further discussed in the following.

Reproducibility of Consecutive Measurements

Since the crystal has to be flashed with a HPF before every single measurement and due to the fact that the voltage connections for the scattering volume and the electron bombardment heating are the same, the cables for applying U_{SV} have to be removed and the high voltage power supply for the flashing procedure has to be connected. After the HPF, the cables of the analyzer power supply have to be reconnected and the detector voltages ramped up again before the measurement can be startedⁱⁱⁱ. Figure 5.15 shows two consecutive measurements of the valence band for different magnetizations, which exhibit a significant intensity difference, which does not originate from a true asymmetry, since the valence band in this region is mainly O $2p$ -derived^{iv}.

When both measurements are not started at exactly the same time after the last HPF, the crystal's temperature during the acquisition can differ for both measurements. Kirschner and Feder [203] studied this impact on W(001) for SPLEED experiments and found the reflected intensity to decrease with increasing temperature according to $DW(T)$ (see also Eq. 3.17):

$$I_{\text{scatt}} = I_0 \cdot DW(T), \quad (5.14)$$

with the incoming and scattered intensity I_0 and I_{scatt} , respectively. They conclude that the three main causes for this temperature dependence—not only of the reflected intensity, but also of the measured polarization—are the reduction of the effective ion-core scattering amplitudes, and the lattice expansion in the bulk and at the surface. Since the temperature of a HPF is up to 2000 °C, temperature differences of several 100 °C are conceivable during the measurement, when not started exactly the same time after a HPF, resulting in different reflectivity values for the spin-filter crystal.

Thus, the time between the HPF and the start of the measurement is crucial and must be the same for each measurement, which otherwise introduces a severe uncertainty.

Overall Experimental Resolution of the Spin Detector

From Fig. 5.14 it can be seen that the spin-resolved HAXPES spectrum of the valence band of magnetite does not show pronounced spectral weight in the near- E_F region—reflecting the Fe $3d$ states—that should be clearly distinguishable from the mainly O $2p$ -derived valence band. To further clarify this issue, another valence-band spectrum was taken in sweep mode at a pass energy of 150 eV to acquire the whole energy range covered by the valence band from E_F up to 14 eV binding energy, which is shown in Fig. 5.16 as blue line (HDA+Spin).

ⁱⁱⁱDue to the fact that the used setup is a HAXPES endstation, for security and radiation protection regulations, the experimental hutch has to be searched and closed prior to any measurement. This procedure also takes several minutes each.

^{iv}The shown spectrum here is the complete acquired detector image with uncalibrated energy scale. Focus here lies on the intensity differences.

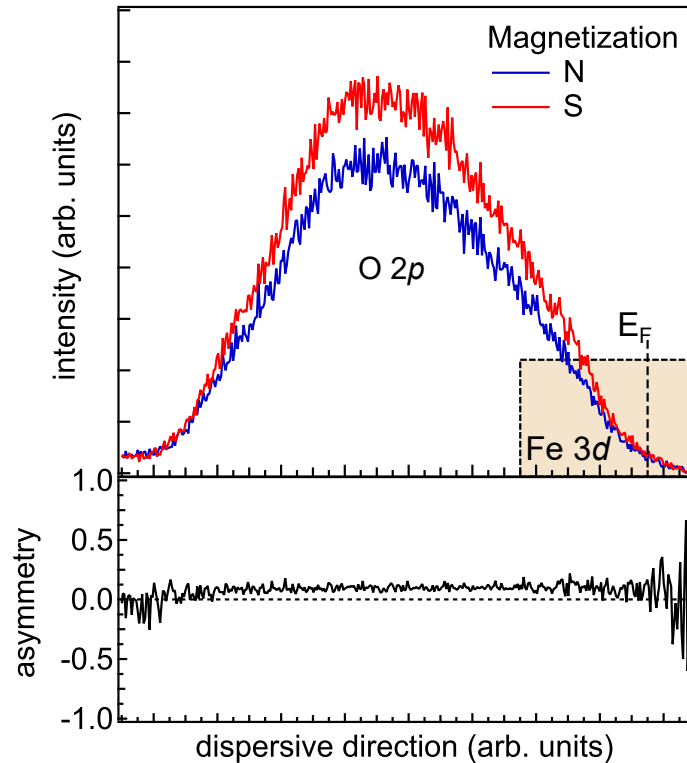


Figure 5.15: Two consecutive measurements with different magnetization exhibit a significant difference in intensity, which is not due to asymmetry effects but reflects a problem with reproducibility.

Also here, no pronounced, clearly distinguishable spectral weight is visible near E_F . For a comparison, the same measurement was carried out without the spin detector mounted (HDA only). The corresponding spectrum is shown as red line in very good agreement with the HDA+Spin measurement. The overall resolution of the HDA with $E_{\text{pass}} = 150$ eV and an entrance slit of $7 \times 30 \text{ mm}^2$ amounts to 1.3 eV [135], which is not good enough to resolve the Fe 3d states with a width of about 1.0 eV. Without the spin detector the pass energy can be decreased down to 50 eV and also a smaller entrance slit of only $3 \times 30 \text{ mm}^2$ is possible, which enhances the energy resolution to 200 meV. The corresponding measurement is shown as green line in Fig. 5.16. Not only did the line shape of the O 2p-derived valence band become more pronounced, but also the Fe 3d states at E_F are now clearly distinguishable. These findings show that the used sample exhibits distinct signal of Fe 3d states, when a decent energy resolution is granted. In contrast, due to the low count rates, a high pass energy and a relatively wide entrance slit, as have to be used for the spin-resolved measurements in order to obtain reasonable count rates, deteriorate the energy resolution tremendously, resulting in the Fe 3d to be significantly broadened and no longer resolvable.

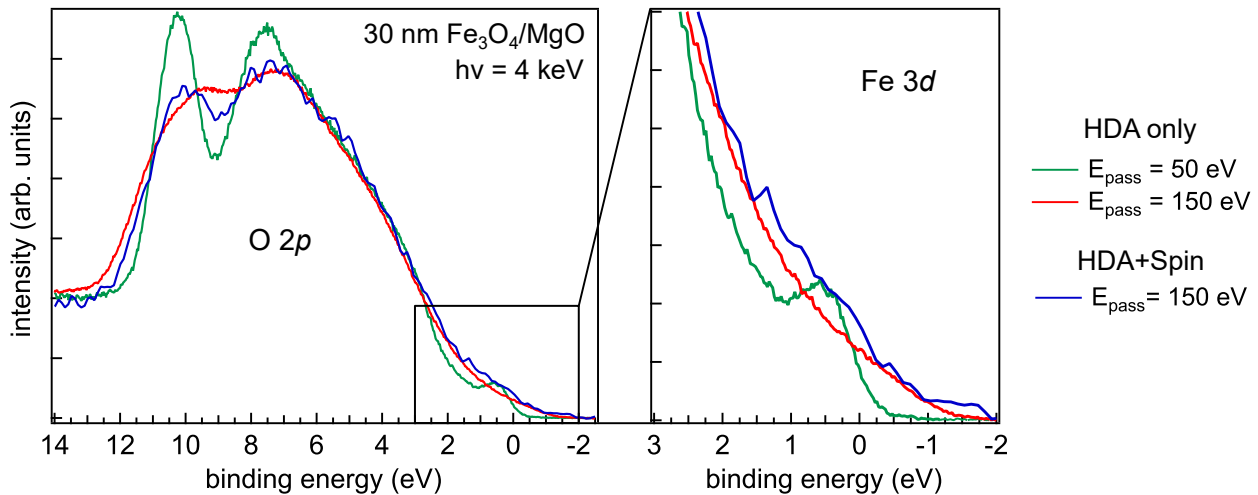


Figure 5.16: Comparison of magnetite’s valence band measured with and without the spin detector attached to the HDA and with different pass energies.

Short Summary

The upgraded setup of the HAXPES endstation at beamline P09 (PETRA III) with an imaging spin detector exhibit low count rates, which only allow for measurements with high pass energy and wide entrance slit. The energy resolution of the combined spin detector and HDA is not sufficient to resolve the investigated Fe 3d states of the test sample. Furthermore, technical obstacles like the electric wiring of the scattering volume, the issue with the crystal’s temperature and also its short lifetime make this setup not suitable for highly sophisticated spin-resolved HAXPES measurements and further development and optimization is needed.

Therefore, a new approach to a more efficient design must be developed, and it is more likely that such an instrument will be designed from scratch rather than adapting an existing system. The group of Prof. Schönense has therefore combined time-of-flight energy recording with a built-in spin-filter option and developed a new momentum-microscope especially optimized for the hard X-ray regime. After introducing the principles of this instrument, the effort of this thesis consists of commissioning and characterization this instrument at the hard X-ray beamline P22 (PETRA III), which is also discussed in the next section.

5.2 Time-of-Flight Microscope with Integrated Spin-Filter

As we have seen in the last section the use of a hemispherical analyzer—although established for photoemission experiments—, in combination with spin-filtering leads to low count rates—especially in the hard X-ray regime when investigating the valence band—, a tremendous decrease of the signal-to-noise ratio and therefore to an increase in measuring time. This chapter deals with a different approach which is based on the combination of TOF energy recording and a built-in spin-filter option. This instrument was developed by our co-operation partner, Prof. Schönense and his group in Mainz. Within this thesis I take part

in commissioning, characterization and performance checks of this instrument to establish its use for bulk-sensitive, spin-resolved HAXPES experiments.

The basic idea is instead of employing the 2D recording scheme of an HDA, which requires entrance and exit slits to obtain a decent energy resolution, the use of the TOF method featuring parallel energy recording allows for the discrimination of essentially all electrons emitted from the sample and furthermore increases the dimensionality of the recording scheme from 2D to 3D (E_{kin}, k_x, k_y)—or even 4D ($P_x, E_{\text{kin}}, k_x, k_y$) when measuring spin-resolved—with the information of the kinetic energy now encoded in the time-of-flight signal.

In the following sections, the basic concept of the developed microscope is shown in detail featuring spin- and momentum-resolution and compared to an HDA, especially with respect to the advantages and upcoming obstacles when performing photoemission experiments with the TOF recording scheme.

5.2.1 Basic Principles and Comparison to a Hemispherical Analyzer

While due to the comparatively high photo absorption cross sections in the soft X-ray and VUV regime the performance of ARPES setups is limited by the maximum count rate of the electron detector, in the hard X-ray regime the phase-space acceptance of the analyzer becomes the crucial criterion. This performance limit can be explained by the strong retardation of the high energetic photoelectrons to the required pass energy of about 50 – 200 eV. Liouville’s theorem describes the conservation of the phase-space volume in electron optics:

$$M \sin \alpha \sqrt{E_{\text{kin}}} = \text{const.}, \quad (5.15)$$

with the lateral size of the beam (quantified by the magnification M), the angular acceptance angle α with respect to the optical axis, and the electron velocity (proportional to $\sqrt{E_{\text{kin}}}$). So when decelerating the photoelectrons from, e.g., 6.4 keV to 100 eV, the square root of the retardation ratio yields a factor of 8 and therefore, to fulfill Eq. 5.15, the beam size has to be increased also by a factor 8. For a hemispherical analyzer typical pass energies and entrance slit widths are 50 eV/2 mm to 200 eV/0.25 mm. In this case, this would lead to an acceptance area on the sample surface which is an order of magnitude smaller than the width of the entrance slit [204].

Due to the fact that—for a TOF spectrometer—the kinetic energy is encoded in the time-of-flight τ , a pulsed photon source like the storage ring of PETRA III (in timing mode, see Sec. 3.4) is required, whereas an HDA can be operated with both, pulsed and continuous photon sources. The great advantage of this TOF spectrometer is, that it does not require any slits which already reduce the electron count rate significantly. More importantly here are sufficiently planar isochrone surfaces with narrow width Δt at the entrance of the field-free TOF section, which is also often referred to as drift tube of length L . Figure 5.17 shows the principal lens scheme of such a TOF-based microscope with the corresponding trajectories of the photoelectrons emitted by a single photon bunch.

The objective lens is designed specifically for the hard X-ray regime to minimize spherical lens aberration despite very large phase space volumes. In contrast to the field free entrance lens of the hemispherical analyzer, the TOF microscope usually operates with an electric

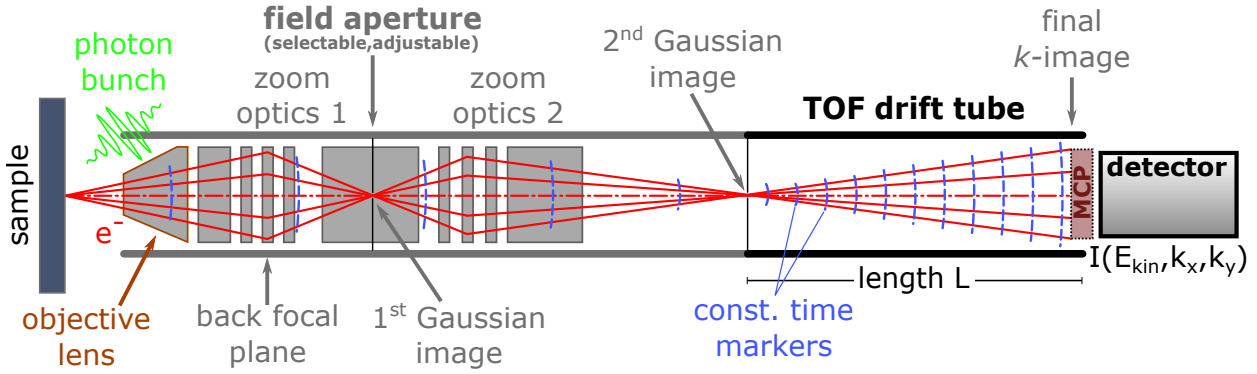


Figure 5.17: (a) Schematic view of the microscope's lens system: Objective lens optimized for low aberrations at high energies with an extractor field of about 1 kV mm^{-1} , two zoom optic columns for focus and deceleration, a field-free drift tube of length L and the DLD with MCP. Typical electron trajectories for photoelectrons excited by a single photon bunch are shown in red. Blue lines are time markers of equal spacing of typically a few ns. Adapted from Ref. [204].

field applied to the objective lens of about 1 kV mm^{-1} , actively extracting the photoelectrons from the sample^v. This allows for the discrimination of all photoelectrons covering an acceptance angle of up to $\pm 90^\circ$ at kinetic energies below 70 eV. In comparison, an HDA using a wide angle lens achieves only acceptance angles of up to $\pm 30^\circ$.

After the photoelectrons are sucked in from the sample by the extractor field the first k -image is built in the back focal or Fourier image plane of the objective lens. The following two lens groups form a first and a second real or Gaussian image by adjusting the beam energy, image size, and angular magnification. The second Gaussian image is built directly at the entrance to the drift tube. The advantage of the drift tube being a field-free section is that most of the electrons travel at constant velocity, which enables the direct conversion from the time-of-flight to the energy scale. In the microscope setup this leads to a large depth of focus with $\approx 8 \text{ eV}$ evaluable energy range [204, 205]. An adjustable field aperture in the first Gaussian image plane allows for the selection of the region of interest, which is not necessary here due to the small photon spot size of about $15 \mu\text{m} \times 15 \mu\text{m}$. Such small photon spots or the use of the aperture for bigger photon footprints on the sample enables microspectroscopy, which is called the *real-space imaging mode*. Imaging of the intermediate real-space allows for the investigation of the sample surface. On the other hand, real space imaging with a hemispherical analyzer is not possible as long as the analyzer is used as a dispersive element. Nevertheless, there are also momentum microscopes with real-space imaging using two HDAs connected to each other. For more information, the interested reader is referred to Ref. [179] and the references therein. Another difference between an HDA and the TOF recording is the fact that in the latter the sample is not grounded, but there is a bias voltage eU_{SA} applied.

^vActually there is a *zero extractor field mode* available, with the sample being grounded, but there are high demands to the photon spot size on the sample and the maximum distance between sample and objective lens. So in this study only the common mode with an extractor field and an applied bias voltage is being discussed.

When entering the drift section, the kinetic or drift energy of the photoelectrons E_d , which is the analogue to E_{pass} , is given by [204]:

$$\begin{aligned} E_d &= h\nu - \Phi_{\text{SA}} - E_B - eU_{\text{SA}} + eU_d + \Delta\Phi \\ &= eU_d + \Delta\Phi, \end{aligned} \quad (5.16)$$

with $U_{\text{SA}} = (h\nu - \Phi_{\text{SA}} - E_B)/e = E_{\text{kin}}^{\text{initial}}/e$ and $h\nu$ the photon energy, the sample work function Φ_{SA} , the binding energy E_B , the bias of the drift section eU_d , and the difference in the work function of the sample and the drift tube $\Delta\Phi$. Thus, only electrons in an energy band between E_F and $E_B = eU_d$ are being transmitted. Important is now that this energy band—translated to a time interval for a given drift energy—should not exceed the photon pulse period T . Otherwise the edges of the photoelectron bunches will overlap with each other [205].

Due to the parallel measurement of the k_x - and k_y -directions in combination with lens diameters of 100 mm and a DLD with 80 mm diameter, the acquired final k -image covers up to $\approx 25\text{\AA}^{-1}$ corresponding to many Brillouin zones (BZs) at the same time without moving the sample. When using an HDA, which only records two-dimensional $k_x - E_{\text{kin}}$ -maps, the sample either has to be tilted or rotated (azimuthal relation) to gradually change the k_y -direction or a deflector arrangement [206, 207] has to be used. In both cases time consuming sequential recording is needed and the acquired band maps then have to be put together to obtain the corresponding $k_x - k_y$ -maps.

As already mentioned the kinetic energy is encoded in the time-of-flight. Thereby, the selected drift energy only applies for the electrons being directly in the focus of the microscope. Electrons with higher or lower kinetic energies are accordingly faster or slower. Thus, while travelling through the drift section, the photoelectron bunch is being extended in direction of motion. This leads to a spatial dispersion of the energy distribution of the photoelectron beam along this direction. At the end of the drift tube the detector measures in intervals of $\Delta\tau$ [178, 208] the intensity of each $k_x - k_y$ -map covering a small energy interval ΔE . Therefore, these maps are often referred to as *constant energy maps*. The energy resolution $\Delta E/\Delta\tau$ and the time-of-flight τ can then be expressed by [209]:

$$\frac{\Delta E}{\Delta\tau} = \sqrt{\frac{8E_d^3}{m_e}} L^{-1} \quad \text{and} \quad \tau = L \sqrt{\frac{m_e}{2E_d}}, \quad (5.17)$$

Thus, a longer drift section leads to a larger spatial distribution of the photoelectron bunch and together with a fast measuring detector array the energy resolution of such a TOF instrument can be significantly enhanced.

The microscope used in this study has a drift tube length of $L = 900$ mm and together with the detector, granting a measuring interval of $\Delta\tau = 150$ ps, the energy resolution and time-of-flight can be calculated according to Eq. 5.17 as a function of the drift energy, which is shown in Fig. 5.18. With these instrumental parameters typical values for E_d are 20 – 80 eV, which result in an instrumental energy resolution of about 16 – 130 meV at a time-of-flight of about 180 – 370 ns. An experimental determination of the instrumental resolution is

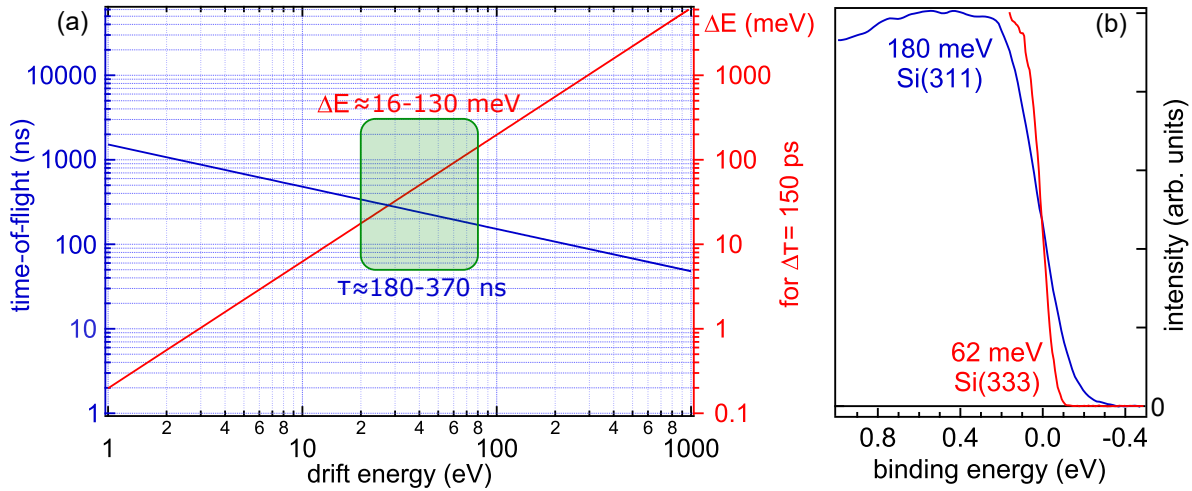


Figure 5.18: (a) Energy resolution ΔE and time-of-flight τ calculated with Eq. 5.17, considering a drift tube length of $L = 900$ mm and a measuring interval of $\Delta\tau = 150$ ps. The green marked area indicates the typical drift energy range of 20 – 80 eV used in the hard X-ray regime. (b) Measured Fermi edge of W(110) at 30 K and $h\nu = 5.977$ keV with two different monochromator crystals Si(311) and Si(333). Data for W(110) adapted from Ref. [204].

shown in Fig. 5.18 (b) based on measurements of the Fermi edge of a W(110) crystal at 30 K and with $h\nu = 5.977$ keV [204]. The measurements were performed with two different monochromator crystals Si(311) and Si(333) revealing a total energy resolution (including beam bandwidth and thermal broadening) of 180 meV and 62 meV, respectively. After deconvolution with the bandwidth of the X-ray beam and thermal broadening, the resulting instrumental resolution of the TOF spectrometer is about 40 meV [204]. Of course the drift energy can be set even far below 20 eV, but this would result in an overlap of the single bunches within the drift section which causes—due to the Coulomb repulsion—broadening effects of the order of 10 meV, energy shifts of up to 1 eV (in the hard X-ray regime, for soft X-ray shifts of one order of magnitude higher were recorded) and an increased background noise [210, 211]. Very high photon densities and thus photoelectron densities within a single bunch can also result in these effects, which are called *space-charge effects*. These reflect a natural limit to the achievable energy resolution in PES. Nevertheless, these effects can—but only up to a certain point—be corrected as described in Schönense *et al.* [210–212]. Since the microscope does not measure the energy of the electrons but the arrival time at the detector, the energy scale has to be calibrated. This is done by several measurements with slightly different bias voltages applied to the sample. By observing the shift of the Fermi cutoff, which reflects the zero reference for E_B , a time interval can be referred to an energy interval. This has to be performed for every different instrumental parameter set like extractor voltage or drift energy, since these quantities have impact on τ and therefore the energy scaling.

After an introduction to the basic idea of the microscope and its measuring principle, the next sections focus on how to perform k - and spin-resolved photoemission measurements, the possibility to obtain photoelectron diffraction patterns within minutes, but also some instrumental peculiarities to be aware of.

5.2.2 TOF-based Spin- and k-resolved Photoelectron Spectroscopy

This section is about the study of core levels and valence band with hard X-rays using TOF recording. First, there are some challenges one has to bear in mind when performing TOF-based spectroscopy. Since such instruments resemble high-pass filters, the investigation of core levels can be more difficult due to a possible overlap with other core levels, especially when considering contributions from higher order radiation. After presenting the potential for hard X-ray photoelectron diffraction (hXPD) and valence-band mapping, the instrumental realisation of an integrated spin-filter option is discussed.

Contribution of higher order radiation

As shown in Sec. 3.4 the storage ring is filled with several electron bunches with a specific width and distance between each other, which depends on the total number of bunches the ring is filled with. In multi bunch mode the ring is filled with up to 960 electron packages. In contrast, in timing mode only 40 bunches are orbiting. While the bunch separation in the multi bunch mode is only 8 ns, which is way too short to perform TOF-based spectroscopy, the timing mode grants a bunch separation of 192 ns, representing a pulsed photon source. As mentioned in Sec. 3.4, the undulator also generates higher harmonics with n -times the photon energy. Hence, depending on the chosen photon energy and mirror positions, these higher orders can also enter the microscope, excite photoelectrons, and because there is no energy filter between the sample and the detector—such high energetic electrons would not pass through an HDA due to the set pass energy—also these high energetic photoelectrons fly through the lens column and drift section and are recorded by the DLD. By coincidence, the time-of-flight of photoelectrons excited by higher order radiation (e.g. with $3h\nu$) can be exactly one bunch period shorter than the “true” signal from the first order. This would result in both electrons to arrive at the same time at the DLD, although excited by different energies. Thus, it is possible to get a signal of a core level in the spectrum of the valence band, which is shown as an example for Mo(110) in Fig. 5.19 [204]. The $k_x - k_y$ -map ($E_B = 3.2$ eV) in (a) was measured with a photon energy of $h\nu = 3.1$ keV. The confined bright spot is a high intensity signal excited by higher order radiation. In (b) the corresponding band map along the dashed line in (a) is shown and in (c) the resulting spectrum integrated over k_x and k_y . Here, it is clearly visible that this signal is not just background but reflects the two core levels Mo $2s$ ($E_B = 2866$ eV) and $2p$ ($E_B = 2625/2520$ eV) excited by the third order ($h\nu = 9.3$ keV). These electrons arrive at the same time as the slower valence band electrons excited by the first order of the previous bunch. This is called the *temporal aliasing effect*. There are different approaches to suppress these higher orders: Since the actual position of the photoelectrons depends on the drift energy, the contribution of a higher order ($-T$) can be shifted out of the spectrum by the variation of E_d . Also changing the photon energy has a different impact on τ for the different orders. Since the higher order electrons are much faster—passing the lens column nearly undeflected, resulting in the strong confinement—they remain essentially unfocused. This gives the possibility to block the high energetic electrons with a combination of apertures and deflectors, which also works for the slower electrons ($+T$). But in general, the dispersion for these low energetic electrons is very large

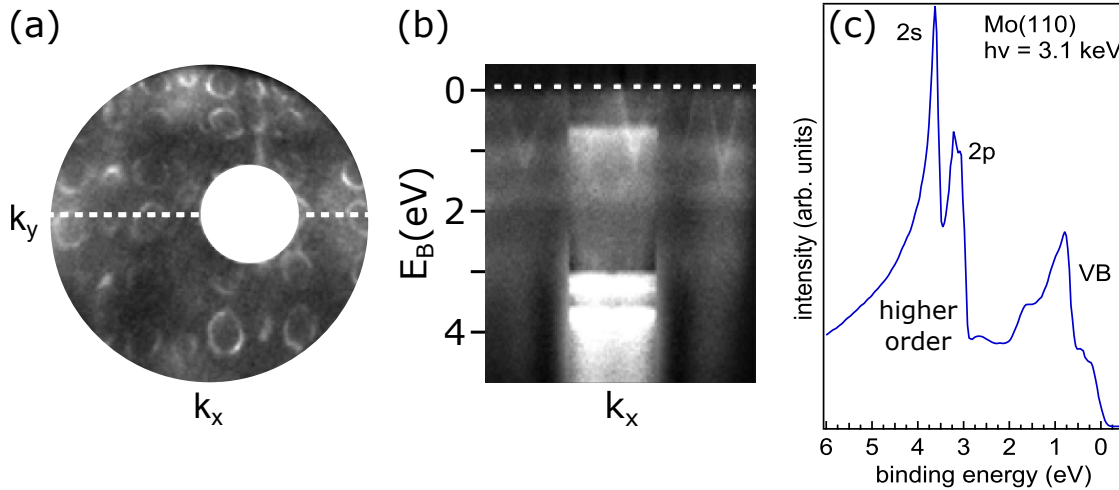


Figure 5.19: (a) $k_x - k_y$ -map of Mo(110) measured with the TOF microscope ($h\nu = 3.1$ keV) at a binding energy of 3.2 eV. The confined white area originates from the high intensity of the Mo $2s$ and $2p$ core levels excited by third order radiation ($h\nu = 9.3$ keV). (b) Corresponding band map along the dashed line in (a). (c) Valence-band spectrum (integrated over k_x and k_y) of Mo(110) showing the Mo $2s$ and $2p$ core levels within the valence-band region. The E_B scale corresponds to the valence band. Data taken and adapted from Ref. [204].

at low drift energies resulting in a strong broadening in time and therefore they are not visible as structures in the spectrum.

Survey TOF spectrum

Depending on the instrumental parameters, the depth of focus of the microscope is about several eV. This challenges the acquisition of survey spectra covering several 100 eV energy range. In Fig. 5.20 such a survey spectrum of a $\text{GaIn}_3\%\text{Mn}_{2.5\%}\text{As}$ sample is shown. The data were recorded over a large energy range of 550 eV in static mode without scanning, meaning that the lens potentials were fixed. This leads to the drift energy covering a large range from 150 eV on the high energy side of the spectrum to 700 eV at the Fermi edge, responsible for the non-linear energy scale. According to Eq. 5.17 this results in a strongly varying energy resolution throughout the spectrum from 0.7 eV up to 3 eV at E_F . Another important aspect visible here is the comparable intensity of the $3s$ and $3p$ core levels. At higher photon energies the photo absorption cross sections decrease significantly, as shown in Sec. 3.3, but weaker for the s -states than the p -states [124]. Also similar to an HDA the transmission of the TOF spectrometer increases for decreasing kinetic energies. This results in a significant spectral weight of In $3d$, despite the relative small content of only 2%, and also a very high signal from O $1s$, which originates only from surface contaminations. This illustrates that the acquisition of wide energy spectra is in principle possible, but is more challenging and complex to evaluate with TOF recording than with a conventional HDA.

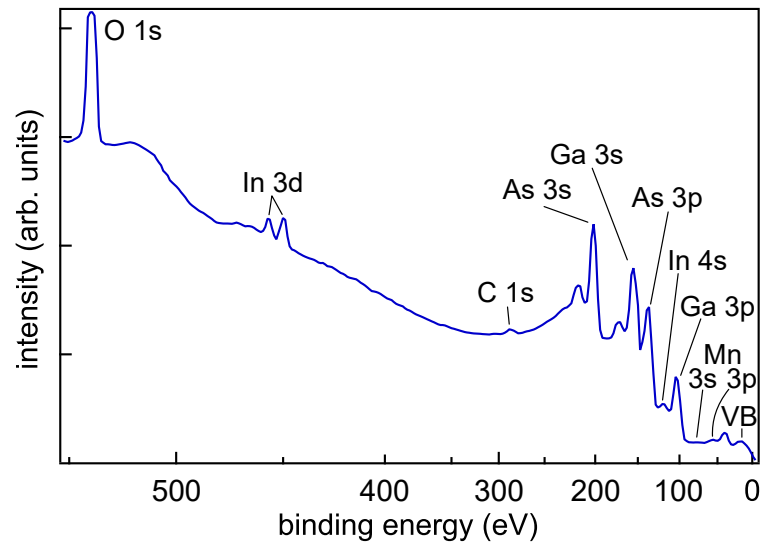


Figure 5.20: Survey spectrum of a $\text{GaIn}_{3\%}\text{Mn}_{2.5\%}\text{As}$ sample taken with a photon energy of $h\nu = 3 \text{ keV}$. Recorded in static mode without scanning. Data adapted from Ref. [204].

Hard X-ray Photoelectron Diffraction

Before proceeding with k -resolved valence-band mapping and the investigation of core levels by TOF recording, hard X-ray photoelectron diffraction (hXPD) has to be introduced since due to the parallel acquisition of k_x and k_y also diffraction patterns are simultaneously recorded and overlaying the detector image. Thus, they may hamper the interpretation especially of the valence band spectra since diffraction effects can be misunderstood as dispersions. Hence, the origin of hXPD will be shortly introduced.

In Fig. 5.21 a very simplified schematic view of the TOF-based hXPD recording is shown for the example of the C $1s$ core level of a graphite sample. Starting with the magnified area at the sample, where the photon bunch impinges, high energetic photoelectrons are locally excited at a given atomic site and then being forward scattered while travelling through the sample's lattice towards the surface. After extraction by the objective lens, the k -image, which contains the diffraction pattern, built in the back focal plane (BFP) of the lens is then magnified onto the DLD by the zoom optics. The resulting detector image taken at a photon energy of 7.2 keV is marked as A, while an image in the region of the electron-loss part of the core-level spectrum is shown in B. A general description of electron emission from sources inside a crystal lattice can be given using the dynamical theory of electron diffraction [213, 214]. Furthermore, the shown simulation of hXPD data A* is based on the many-beam dynamical theory for photoelectrons [215]. In particular, when using hard X-rays, due to the enhanced probing depth, the measurement is significantly more bulk sensitive and therefore the electrons are emitted from deeper atomic layers within the crystal. Thus, those electrons are scattered at more lattice planes before exiting the sample and the diffraction patterns are more pronounced [216, 217]. The field of view is about 16 \AA^{-1} at a k -resolution of 0.025 \AA^{-1} .

A detailed hXPD study performed with this instrument for graphite within the photon energy range from $2.8 - 7.3 \text{ keV}$ can be found in Ref. [218].

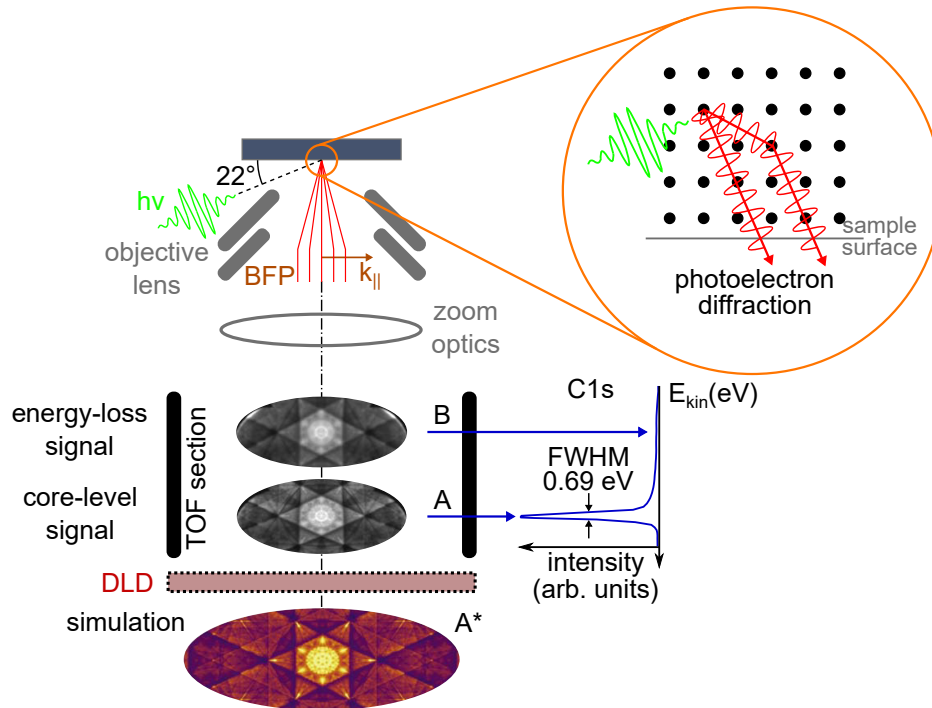


Figure 5.21: Simplified schematic view of the TOF-based hXPD recording of the C 1s core level. The k -image is formed in the back focal plane (BFP) of the objective lens and magnified to fit the size of the detector by the zoom optics. A and B are the recorded diffractograms for the core level and the inelastic-loss part of the spectrum, respectively. A^* shows the simulation of A carried out by the many-beam dynamical theory [215]. Figure adapted from Ref. [218].

Valence Band Mapping

Hard X-ray photoemission allows us to probe the valence band of bulk materials and heterostructures, especially buried interfaces. Although many valence-band studies were performed with high energy photons in the past, they all face various obstacles like decreasing cross sections and significantly increasing quasi-elastic electron-phonon scattering, which pose a major challenge for the investigation of band structures [126, 128, 131, 219–222]. Another point that has to be taken into account at high excitation energies is the transfer of the photon momentum $\mathbf{k}_{h\nu}$ to the photoelectron. This results in a shift of the k -pattern, which—in combination with the interplay with hXPD—has recently been studied by Schönhense *et al.* [223].

In Fig. 5.22 $k_x - k_y$ -maps of rhenium are shown, taken at different photon energies up to 6 keV and at a temperature of about 30 K. In (a) and (b) the Fermi surface map ($h\nu = 3830$ eV) covers up to 19 BZs (about 16 \AA^{-1} in k_x and k_y) in a single measurement with an acquisition time of only 15 min. The white arrows mark the center of each BZ and illustrate the curvature of the final state energy isosphere due to the large field of view. It is noticeable that the arrows lie on a ring with the same distance from the X marker, which represents the top of the sphere and is not in the middle of the detector image due to the photon momentum $\mathbf{k}_{h\nu}$, which shifts the whole image. The direction and magnitude of the shift

depends on the geometry of the measurement and the photon energy. This effect can also be seen in the corresponding band map (E_B vs. k_y) in Fig. 5.22 (c), resulting in only two of the downward-dispersing bands reaching the Fermi level next to the X marker. A weak Lorentzian deformation is also seen, which originates from space-charge effects. The already mentioned phonon scattering at high energies causes a background in the images, which was subtracted as described by Gray *et al.* [128] and the intensity modulations caused by diffraction of the photoelectrons was removed as described by Babenkov *et al.* [132].

In Fig. 5.22 (d) the k -space scheme of direct transitions from the valence band to free-electron-like final states leading to an energy isosphere with the center at $\mathbf{k} = (0, 0, 0)$ is shown. Here the curvature of the final state isosphere is depicted for different excitation energies. The measured $k_x - k_y$ -map therefore is not showing the expected full sixfold symmetry, since k_z decreases with increasing distance from the center of the isosphere. The used photon energies show the different final-state isospheres crossing the region between the 18th and 28th BZ along k_z . The transfer of the photon momentum $\mathbf{k}_{h\nu}$ to the photoelectron appears here as a shift in k_y -direction—increasing at higher photon energies—resulting in the center not being at $\mathbf{k} = (0, 0, 0)$ anymore. Considering an impact angle of 22° , the photoelectron shift in lateral, Δk_{\parallel} , and perpendicular, Δk_{\perp} , direction can be expressed by [204]:

$$\begin{aligned}\Delta k_{\parallel} &= |\mathbf{k}_{h\nu}| \cos 22^\circ = 1.24 G_{11\bar{2}0} = 2.82 \text{ \AA}^{-1} \\ \Delta k_{\perp} &= |\mathbf{k}_{h\nu}| \sin 22^\circ = 0.81 G_{0001} = 1.14 \text{ \AA}^{-1},\end{aligned}\tag{5.18}$$

with reciprocal lattice vectors $G_{0001} = 2.276 \text{ \AA}^{-1}$ along the $\Gamma - A$ -direction and $G_{11\bar{2}0} = 1.410 \text{ \AA}^{-1}$ along the $\Gamma - M$ -direction, and the photon momentum $|\mathbf{k}_{h\nu}| = 3.04 \text{ \AA}^{-1}$ at $h\nu = 6 \text{ keV}$.

The $k_x - k_y$ -maps for these higher energies are shown in Fig. 5.22 (e) and (f). Here, the curvature of the isosphere is decreased resulting in the small circles being shifted outwards, which can be seen when comparing the white and black arrows of (b) and (e).

Due to the parallel acquisition of three dimensional arrays $I(E_{\text{kin}}, k_x, k_y)$, it is easy to cover the four dimensional energy-momentum parameter space by measuring at about 20 different photon energies, thereby subsequently changing the measured k_z value and crossing a full BZ in this direction. By taking the individual Fermi surfaces of each measurement and concatenating them into a single array, this allows for the investigation of Fermi surfaces in 3D k -space. Figure 5.22 (g) shows such a 3D Fermi surface which illustrates the impressive diversity of the developed TOF instrument. For the interested reader, a detailed study on TOF-based 3D mapping of the Fermi surface can be found in Ref. [224] and another study of bulk band mapping in Ref. [132].

Core Level Spectroscopy

The taken k -images of core levels represent pure hXPD patterns—since no dispersion is to be expected—and give structural information of the sample, complementary to the information of the electronic structure when performing valence-band mapping. A major difference from

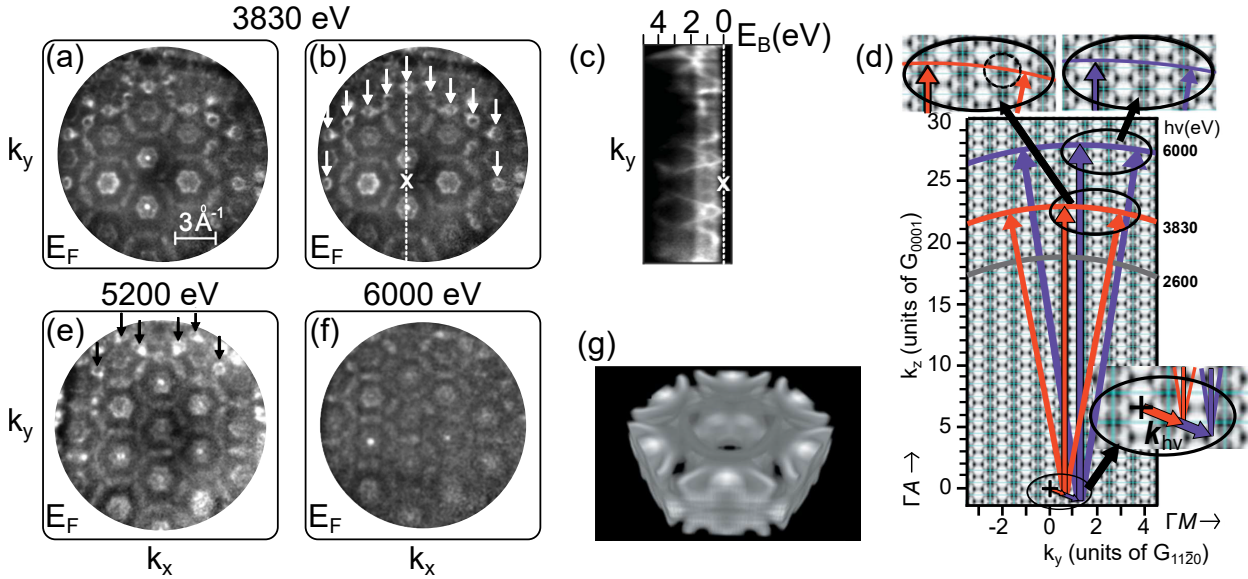


Figure 5.22: Hard X-ray mapping of the valence band of Re(0001) at a temperature of 30 K and different photon energies: (a) and (b) $k_x - k_y$ -map at E_F measured with $h\nu = 3.83$ keV showing up to 19 BZs (about 16 \AA^{-1} in both directions). Arrows indicate the center of several BZs showing the curvature of the final state energy isosphere in k -space. The X marks the top of the sphere. (c) $E_B - k_y$ -map along the dashed line in (b) showing the band dispersion of the Re d -bands. (d) Direct transitions viewed from the valence band to free-electron-like final states as a k -space scheme for the different photon energies used. (e)-(f) Further $k_x - k_y$ -maps taken at different photon energies. (g) Measured 3D Fermi surface at $h\nu = 3.83$ keV. Data adapted from Ref. [204].

the study of the valence bands is the significantly increased photo absorption cross sections for core levels, which allow k -images to be acquired in just a few minutes. According to Eq. 5.16, to change the energy window to the respective core level, the bias voltage of the sample eU_{SA} has to be adjusted. Only for significant changes of the sample potential also a slight refocusing of the objective lens becomes necessary.

Figure 5.23 shows different k -distributions of Re core levels and the corresponding (over k_x and k_y) integrated energy spectra [(a,b) Re $4f$, (c,d) Re $4d_{5/2}$, (e,f) Re $3d_{5/2}$] taken at $h\nu = 3.5$ keV showing an excellent signal-to-noise-ratio. The blue areas mark the spectral range over which the diffractograms were integrated. Note that for (c) and (e) the spin-orbit splitting of 13 eV and 66 eV is too large for the selected region and only the line with the higher angular momentum is recorded. Larger energy ranges can be recorded by using higher drift energies, as shown in Fig. 5.20. Also the effect of measuring signal from higher order radiation can be seen in core-level spectroscopy (see Re $4d$ in Fig. 5.23 (g,h)). While for the same core level recorded with $h\nu = 3.5$ keV in (c,d) no higher order is visible, by slightly shifting the photon energy to $h\nu = 3.75$ keV, a bright and confined spot in the diffraction pattern appears. In the corresponding spectrum clearly additional structures are visible. To identify this higher order radiation signal, one has to consider the different energies of the electrons at different stages within the microscope: For the given photon energy of 3.75 keV the photoelectrons excited from the Re $4d_{5/2}$ core levels have a kinetic energy of 3.48 keV. To obtain the required drift energy of 60 eV, the energy of these electrons has

to be decreased by 3.42 keV. The electrons being excited by the higher order from photon bunch $\#n$ arrive at the same time at the detector as the Re $4d$ electrons from the previous photon bunch $\#n - 1$. Consequently, the electrons from this higher order must have an initial kinetic energy of about 6 keV. Assuming a third order radiation energy of 11.25 keV, this high energetic electrons originate from the L_3MM Auger lines with kinetic energies of about 5.97 keV. Note that also here the energy scale does not refer to the Auger signal, but only to the electrons being excited from the first order radiation.

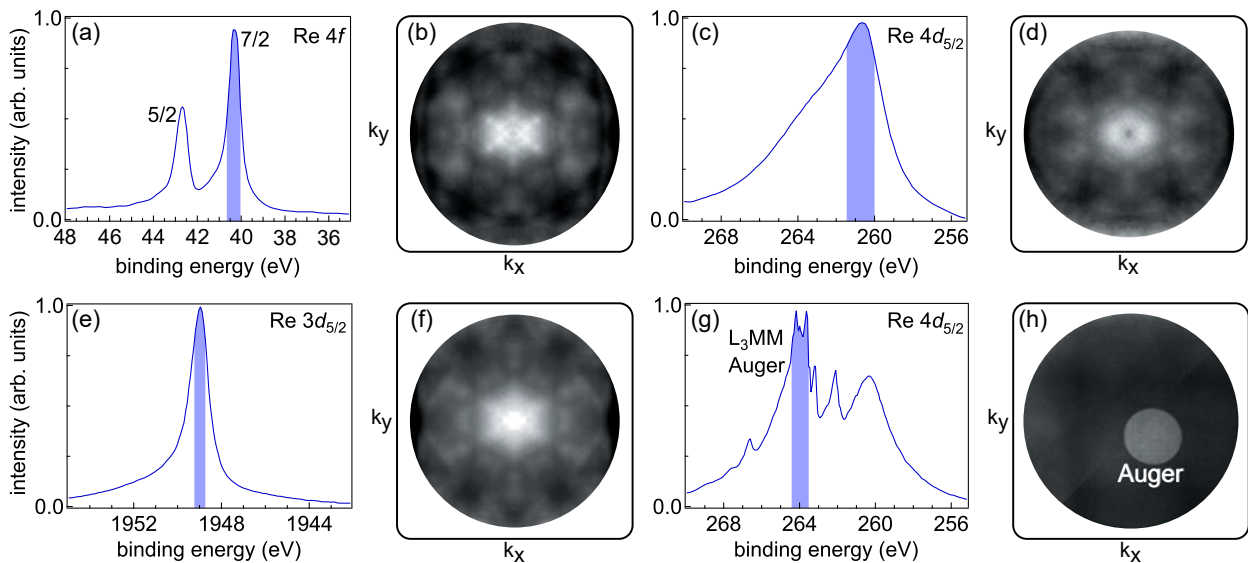


Figure 5.23: Different core-level spectra together with the corresponding $k_x - k_y$ -maps of Re $4f$ (a,b), $4d_{5/2}$ (c,d), and $3d_{5/2}$ (e,f) measured with $h\nu = 3.5$ keV. At $h\nu = 3.75$ keV third order radiation ($h\nu = 11.25$ keV) excites the L_3MM Auger transition and the resulting photoelectrons arrive in the same time window as those from the Re $4d$ core level (g,h). The blue marked areas indicate the energy range being integrated for the corresponding diffractograms. Data adapted from Ref. [204].

Integrated Imaging Spin-Filter

We have now introduced the principles of working with TOF recording and momentum-resolved imaging, the possibility to acquire survey scans and the obstacles one has to deal with, the fast acquisition of hXPD patterns, which information one can obtain with valence-band mapping especially without moving the sample, and the good signal-to-noise ratio when measuring core levels including the k -distributions in only a few minutes. Also the impact of the drift energy on the energy resolution and time-of-flight as well as the problem of higher order radiation were discussed. Now we focus on the built-in imaging spin-filter option to enable spin-resolved HAXPES.

Figure 5.24 shows the schematic view of the momentum microscope now with a second branch pointing upwards, equipped with its own drift tube and DLD. At the connection between the microscope column and the second branch is the position of the Ir(111) imaging spin-filter. What makes it special is that the spin-filter crystal is attached to a 5-axis

manipulator so that the crystal can be retracted and inserted into the electron trajectory as needed. With the crystal retracted, the electrons travel straight through the first branch and are recorded k -resolved and spin-integrated—with maximum intensity and k -resolution—at the detector (here greyed out). After moving the crystal into the plane of the second Gaussian image, the electrons are scattered into the spin branch and the four-dimensional k -resolved and spin-filtered $I(P_x, E_{\text{kin}}, k_x, k_y)$ -array is detected at the second DLD. Thereby, the scattering angle with respect to the crystal surface normal (green dashed line) amounts to 56° and the scattering energy is set by the second zoom optic right in front of the crystal (as shown in Fig. 5.17). The manipulator allows precise alignment of the crystal lattice with respect to the electron trajectories and is equipped with an electron bombardment heating stage (see also Sec. 5.1.2). When being retracted, the crystal has its own preparation chamber, which can be separated from the microscope via a gate valve. Therefore, one can switch between high k resolution photoelectron microscopy and spin-resolved photoemission within minutes, provided that the surface of the spin-filter crystal is well prepared.

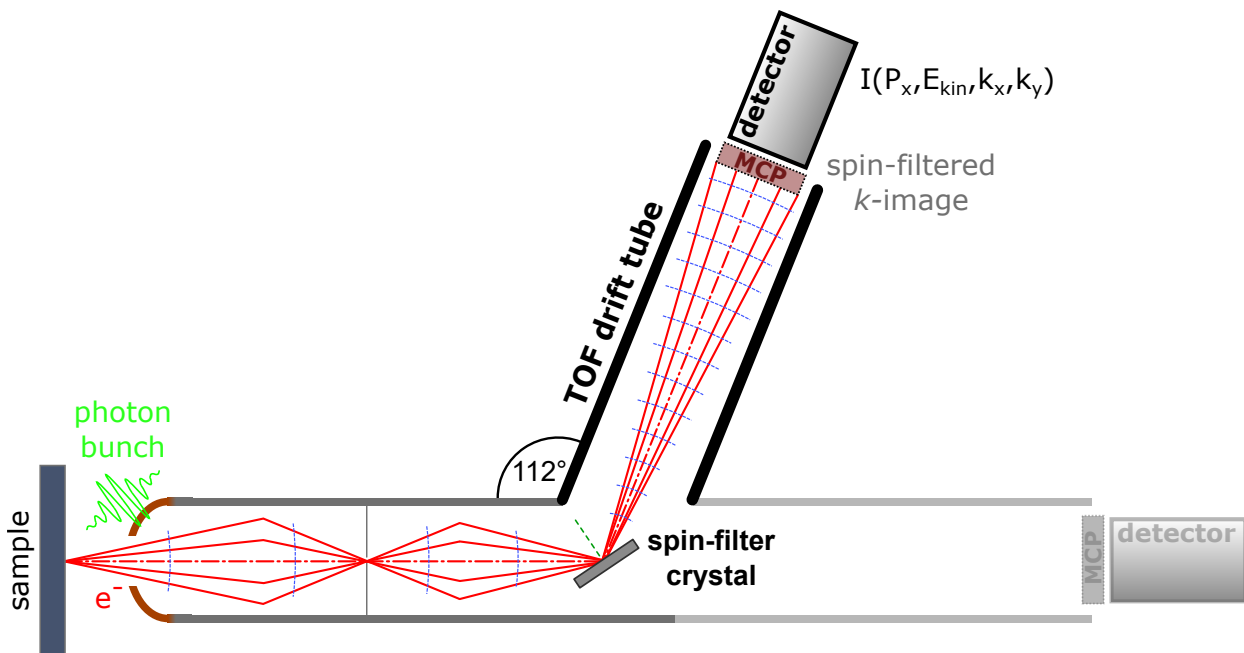


Figure 5.24: Momentum microscope with imaging spin-filter inserted: The spin-filter crystal is mounted to a manipulator that is inserted into the second Gaussian image plane. Photoelectrons scatter at the lattice when impinging on its surface and travel through the drift tube upwards to a second DLD.

5.2.3 Future Instrumental Developments

Although the k -space microscope sets new standards in hard X-ray photoemission spectroscopy, especially in the field of spin- and k -resolution, there is still room for advancements. First, the here used spin-filter crystals have disadvantages like, e.g., low reflectivities

and varying spin sensitivities for slightly different scattering energies, that demand for improvements. While the surface of tungsten is very easy to prepare, when using iridium there is a risk of facets forming on the surface that affect the scattering of photoelectrons, even though the surface has a much longer lifetime than that of tungsten. As shown, the calibration of the Sherman function of the crystal is crucial, since when TOF recording is employed, the explicit *energy dependence* of the Sherman function $S = S(E)$ is required (see also Sec. 7.2). When probing a wide energy range, this spin sensitivity can strongly vary. In this context, the perfect spin-filter crystal would have a high value of its Sherman function and reflectivity, being essentially constant over a wide range of several eV, and has an easy-to-prepare surface with a long lifetime.

A second aspect which can be optimized in future instrumental development is the suppression of higher order radiation. Two different approaches have been developed so far:

Built-in chicane

The group of Prof. Schönense is currently developing a momentum microscope with built-in chicane in vertical direction. This geometry separates the microscope column into three sections with two deflector lenses in between, resulting in an offset between incoming and outgoing photoelectron beam of about 5 mm, as it is shown in Fig. 5.25. Thereby, the first column with the extractor lens is identical to the one previously described. But now, at the end of column **I**, a deflector bends the beam down by about $3 - 5^\circ$. At the end of column **II** a selector aperture follows. Assuming that an electron beam with 60 eV (red) passes exactly through this aperture, a beam of electrons with higher energy, e.g., excited by higher order radiation (here 300 eV, green), is bent less by deflector 1 and therefore this beam is blocked by the selector. By positioning a reciprocal image exactly at the bending point between section **I** and **II**, aberrations caused by symmetry breaking effects are eliminated. A second deflector right after the selector aperture bends the beam back into the horizontal plane before entering the drift tube (**III**) and finally, the k -image reaches the detector. This adaption is also suitable for the combination of an optional spin-filter being inserted right before entering the drift tube, which requires another spin-branch and detector as shown in Fig. 5.24.

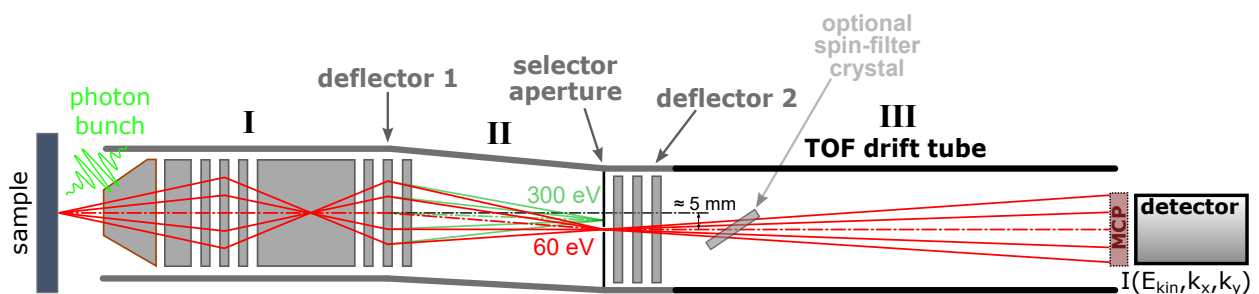


Figure 5.25: Realization of a momentum microscope with built-in chicane to suppress higher order radiation by a 5 mm offset that blocks all beams that are deflected more or less than the “true” beam (60 eV, red).

Combination of an imaging HDA with TOF-based energy recording

Another approach is to combine the energy filtering capability of an HDA with TOF energy recording as shown in Fig. 5.26 [225]. Thereby, again the entrance optics do not differ from the one described in Sec. 5.2. But here, the second Gaussian image (GI2) is formed at the entrance of a large hemisphere equipped with an entrance and exit slit. The electrons with $\alpha_0^* = 0$ travel on a circular trajectory with radius R_0 and pass the exit aperture (trajectory 1). Electrons that deviate with $\alpha_0^* \neq 0$ travel on Kepler ellipses (trajectories 2 and 3) and—depending on whether they travel closer to the inner (2) or outer (3) hemisphere—do not pass the exit slit and fall short^{vi} with a Radius of $R_\pi = R_0 - K \cos^2 \alpha$ with K being a prefactor depending on details of the so-called *fringe-field corrections* [179, 226, 227]. While in an ideal spherical field perfect first order focusing is achieved after 180° , the spherical field is terminated here by the electrodes to which the slits are attached [228]. The correction of these fringe-fields is crucial for a momentum microscope since they affect the energy as well as k -resolution^{vii}. Here, the correction of the fringe-field is made by four *Jost-plates* installed next to the slits, enhancing the field in the fringe region to compensate field termination [229, 230]. By treating the potentials of the four plates as free parameters, the correction can be maximally optimized [226, 227].

Another effect that has to be considered is the *time spread* of electrons passing the HDA. For the electrons on a circular trajectory the transit time can be calculated analogously to Eq. 5.17:

$$t_0 = \pi R_0 \sqrt{\frac{m_e}{2E_{\text{pass}}}}. \quad (5.19)$$

Assuming a given analyzer radius of 225 mm and a typical pass energy for this setup of 660 eV, the transit time is $t_0 = 46$ ns. For $\alpha_0^* > 0$ ($\alpha_0^* < 0$) the path is shorter (longer) and therefore also the transit time. The full width at half maximum of the time spread profile can be approximated by [231]:

$$\frac{\Delta t_{\text{FWHM}}}{t_0} \approx 0.6 \left(\frac{W}{R_0} \right) + 2.23 \left(1 - 2.79 \frac{W}{R_0} \right) \alpha_{0,\text{max}}^*. \quad (5.20)$$

For a slit width W of 2 mm and $\alpha_{0,\text{max}}^* = 1^\circ$ one gets $\Delta t_{\text{FWHM}} = 2.0$ ns. To correct this time spread numerically, also the transit time for the Kepler orbits t_π is needed, which depends on α_0^* and can be approximated by [232]:

$$t_\pi(\alpha_0^*) \approx t_0 \left(1 + 4 \frac{\alpha_0^*}{\pi} - 10 \frac{\alpha_0^{*3}}{3\pi} \right). \quad (5.21)$$

For the given parameters and an angle of $\alpha_0^* = 1^\circ$, this results in a transit time of $t_\pi(1^\circ) = 47$ ns and thus a change of 1 ns with respect to t_0 , which equals 2.1%. This time spread can further be minimized by several instrumental approaches like using paracentric entry con-

^{vi}Only for low pass energies these electrons can travel through the exit slit, which is often referred to as the *non-isochromaticity*.

^{vii}Note that the energy resolution of an HDA given by Eq. 5.11 does not apply here since the HDA is working in an imaging mode and not as a dispersive element.

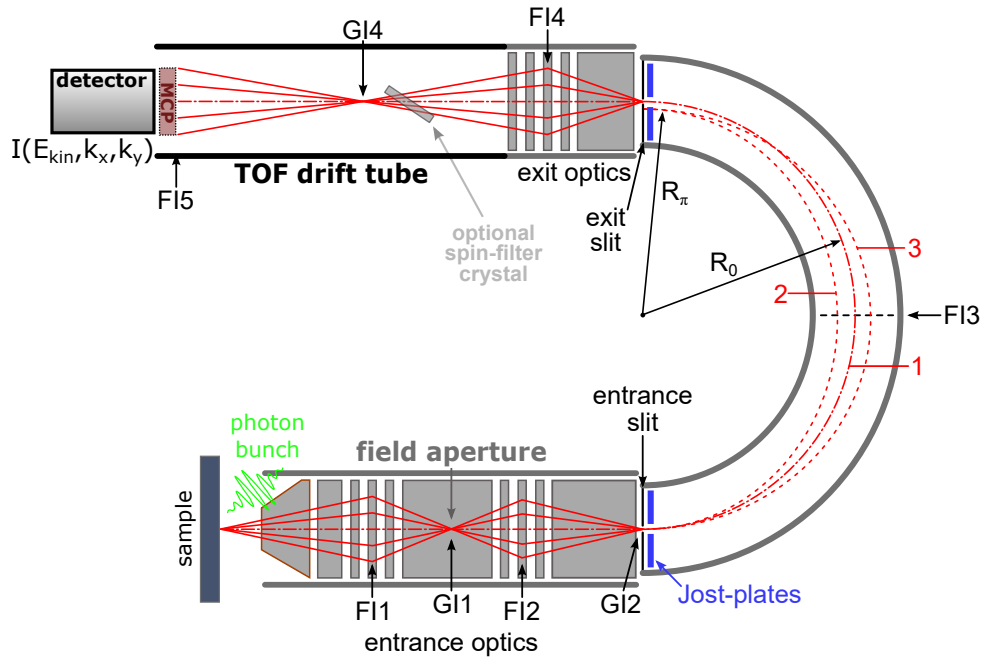


Figure 5.26: Illustration of the concept of a single hemisphere TOF-based momentum microscope as adapted from Ref. [225]: The entrance optics as described in Sec. 5.2 forms a Gaussian image at the entrance slit of a large HDA. Only electrons with $\alpha_0^* = 0$ (trajectory 1) travel through the hemisphere with the radius R_0 and pass through the exit slit. Other electrons with $\alpha_0^* \neq 0$ fall too short with a reduced radius of R_π (trajectories 2 and 3). After the hemisphere the electrons enter the TOF section and are recorded in the Fourier image (FI5) at the DLD.

ditions [232–234], a tandem combination of two HDAs connected to each other with an inverting lens in between [235] or the use of a tilted orientation of the detector [236].

After exiting the hemisphere, the photoelectrons enter the TOF section and a Fourier image (FI5) is detected by an ultrafast measuring DLD. This specially adapted detector has a measuring frequency of about 70 ps, allowing this setup to be used with high pulse rates such as synchrotrons with a 500 MHz time structure [237]. By adding the spin-filter behind the hemisphere, this setup is also applicable for spin-resolved experiments.

5.3 Summary

This chapter was about the introduction of two different approaches to realize spin- and k -resolved photoemission within the hard X-ray regime. The first was to extend an already existing HAXPES setup equipped with an HDA for energy dispersion by an external spin detector, which is shown in Fig. 5.27 (a). This spin detector includes a W(001) single crystal as spin-filter and its own DLD. The first test measurements and commissioning studies revealed very low count rates due to the low reflectivity of the crystal and the necessity of using slits for the hemisphere. To counteract this, high pass energy is used, reducing the energy resolution significantly, hampering the measurement of the Fe 3d states of a magnetite reference sample. Furthermore, the short lifetime of the tungsten crystal

combined with poor reproducibility of subsequent measurements with a preparation cycle in between represent a further obstacle that has to be solved. This makes clear that spin-resolved photoemission is way more challenging in the hard X-ray regime than when using low excitation energies. Accordingly, although the combination of an HDA with a Mott detector has generated exciting studies over the past decades, for the hard X-ray regime the use of an HDA—even with the combination of the promising imaging spin-filter technique with multichannel electron detection—is quite cumbersome and turned out to be not feasible within the project of this thesis. Therefore, new routes have to be followed to enable bulk-sensitive, spin-resolved photoemission experiments.

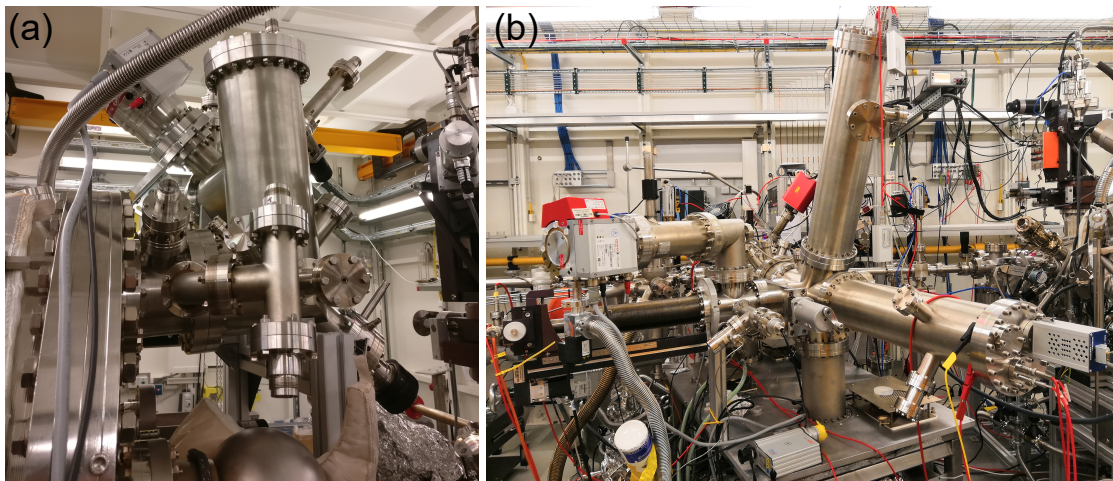


Figure 5.27: (a) External spin detector attached to the HDA of the HAXPES endstation of P22, DESY. (b) Momentum microscope with the k -resolved branch in the horizontal plane and the spin- and k -resolved branch pointing upwards. On the left is the manipulator to retract the spin-filter crystal.

In Fig. 5.27 (b) the second approach—the momentum microscope—is shown with the manipulator on the left side carrying the optional Ir(100) spin-filter crystal. Using the time-of-flight of the photoelectrons for energy recording, allowing for the acquisition of $I(E_{\text{kin}}, k_x, k_y)$ -arrays, grants much higher count rates due to the lack of any slits and the discrimination of essentially *all* electrons from the sample. It has been demonstrated that valence-band mapping as well as the study of core levels and hXPD patterns can be done in very short time with an astonishing efficiency and energy as well as momentum resolution. Future instrumental developments like the discussed built-in chicane or the combination of both, an HDA and TOF recording, can further optimize aberrations and the obstacle of higher order contribution to the measured k -images and spectra.

For spin-resolved measurements, the necessary spin-filter surface preparation was introduced for the example of the W(001) crystal, and the cleanliness of the crystal was verified by LEED. It has been shown that the temperature during the LPF is crucial as for too low temperatures carbon remains on the crystal’s surface.

The momentum-microscope is used to investigate the buried q2DES at the dLAO/KTO interface and to determine the bulk spin polarization of $\text{Fe}_3\text{O}_4(111)$ on $\text{ZnO}(0001)$ with synchrotron-based hard X-ray radiation.

6 Buried Electron System in the $\text{LaAlO}_3/\text{KTaO}_3$ Heterostructure

This chapter is about the investigation of the buried quasi two-dimensional electron system at the heterostructure interface of disordered LaAlO_3 (dLAO) and KTaO_3 (KTO). The sample was prepared by pulsed laser deposition within a UHV system. By depositing dLAO on a KTO single crystal substrate, which was held at room temperature during growth, the oxygen deficient dLAO is generating oxygen vacancies at the interface forming the q2DES. A detailed study of the sample fabrication can be found in Ref. [23, 31].

In the following, the focus lies on the characterization of the electronic properties of the interface by means of HAXPES and afterwards, the q2DES is studied by angle-resolved hard X-ray TOF-based photoemission (HARPES).

6.1 Electronic Properties of the LAO/KTO-Interface

To proof the formation of the q2DES at the interface of dLAO/KTO, Fig. 6.1 (a) shows the Ta $4f$ core level of a pure KTO substrate (red) and one with 1.6 nm dLAO on top (blue), both measured with an excitation energy of 5 keV. While the spectra of the KTO substrate exhibit only Ta^{5+} signal, there is a small spectral weight at the lower binding energy side of the $4f_{7/2}$ peak in the spectrum of the dLAO/KTO sample, reflecting a partial reduction of Ta^{5+} to Ta^{4+} . This reduction transforms the original $5d^0$ system into a partially $5d^1$ system. These $5d$ carriers can be seen in Fig. 6.1 (b) directly at the Fermi edge E_F . That these $5d$ carriers are only originating from the interface of the dLAO/KTO heterostructure and not from the bulk of KTO, and also a detailed investigation of the electron transport properties of the q2DES, was already part of a previous study [23, 31]. In summary, the dLAO/KTO sample used here is well characterized and of high quality and clearly shows the characteristic lineshape of the Ta $4f$ core level as well as significant Ta $5d$ spectral weight at E_F , as expected for the q2DES formed at the interface.

6.2 Momentum-Resolved Hard X-ray Time-of-Flight Photoemission of the 2DES

As described in Sec. 5.2.2, the big advantage of the TOF method is the parallel acquisition of the k_x - and k_y -direction over an energy range of several eV. This allows for ultra fast measuring of many constant energy maps of the q2DES. Here, especially the Fermi surface

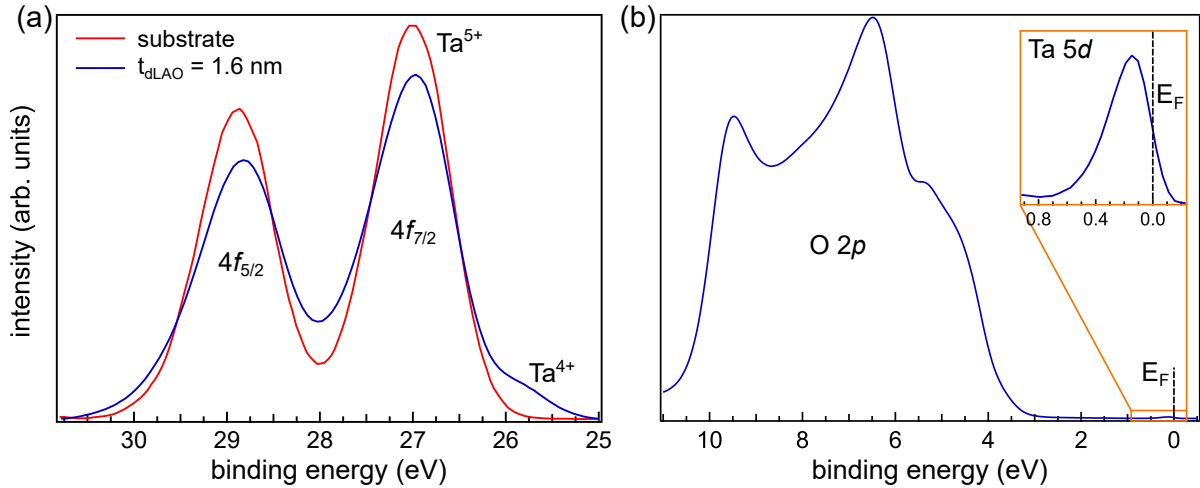


Figure 6.1: (a) Ta $4f$ core-level spectra of a bare KTO substrate (red) and one with a 1.6 nm thick disordered LAO capping layer (blue). The latter shows a shoulder at the $4f_{7/2}$ peak, representing the formation of Ta^{4+} by oxygen vacancies. (b) The valence-band spectrum of dLAO/KTO shows spectral weight at E_F originating from Ta $5d$ carriers. All spectra were taken at a photon energy of $h\nu = 5.0$ keV and the higher resolution Si(311) monochromator crystal pair.

is investigated, where the Ta $5d$ -derived carriers are centered around and concentrated close to the Γ -point. Therefore, a suitable photon energy has to be used so that the k_z value cuts the BZ at the Γ -point. With Eqs. 3.4 and 3.5 the k -scaling of the measurement can be calculated—assuming a negligible work function compared to the photon energy, an incident angle of the photon beam of 21° and an inner potential of 12 eV [23, 31]. Still, the calculated photon energy necessary to measure a certain BZ is just an approximate value, since the photon energy has not been previously calibrated and can deviate from the setpoint by several eV. In addition, high background intensity due to contribution of higher order radiation can also have an impact on the measurement and can force the use of a different photon energy. After cooling the sample down to ≈ 30 K to minimize the Debye-Waller factor, an energy range from slightly above E_F down to about 10 eV binding energy was acquired at a photon energy of 4458 eV—suitable for measuring the 23rd BZ with respect to the k_z -direction. The resulting Fermi surface map, for which all data points of the corresponding spectra were integrated over a binding energy range from -0.2 to 0.5 eV, i.e., essentially the full Ta $5d$ band width, is shown in Fig. 6.2 (a). In the right half of the detector image several Γ -points can be seen with slightly different intensities, while on the left side no spots are detectable. Furthermore, there is a bright confined spot in the image, originating from higher order radiation. A uniform distribution of Γ -points over the entire detector is not observed. This can be due to a minor deviation of the photon energy resulting in the final state sphere cutting slightly above or below the Γ -points. Although the photon energy was varied by a few eV in both directions, the detector image could not be improved. Also, attempts to measure the 24th BZ at a photon energy of 4857 eV as shown in Fig. 6.2 (b) only solved the problem of the higher order radiation. At a slightly higher photon energy of 4892 eV as shown in (c) the detector image slightly improved and more spots on the left side of the detector appeared, but still no homogeneous distribution

of the Γ -points is observed. This behaviour could also be related to a misalignment of the electrostatic electron lenses within the microscope column. Indeed, after optimizing the deflector lenses and further energy scanning a uniform distribution of about 26 Γ -points could be measured at an energy of 5177 eV—originating from the 25th BZ—which can be seen in Fig. 6.2 (d). Although there is a higher order contribution here as well, it is rather weak and can be easily corrected later. A slight counterclockwise rotation of the entire spot array is also visible and stems from the fact that the sample was also rotated slightly about its surface normal. Such a misalignment is not crucial in our case, but could be avoided, e.g., by performing LEED prior to the measurements, which allows a very accurate alignment of the crystal lattice relative to the microscope optics. Figure 6.2 (e) shows the calculated reciprocal space as a $k_x - k_z$ -map. At the center of each BZ (shown as blue squares) is the Γ -point (green), while in blue are the M -points at the corners and the X -points at the edges to an adjacent BZ. The red area represents the measured reciprocal space covered by the different k_z -values depending on the used photon energy. The acceptance angle of the microscope is hereby about $\pm 8^\circ$, allowing for the acquisition of up to 6 BZs in both directions. The photon momentum is taken into account with an incident angle of 21° with respect to the sample surface normal. Since the k -image at 5177 eV has the best quality and shows the most Γ -points, it is taken for further evaluation.

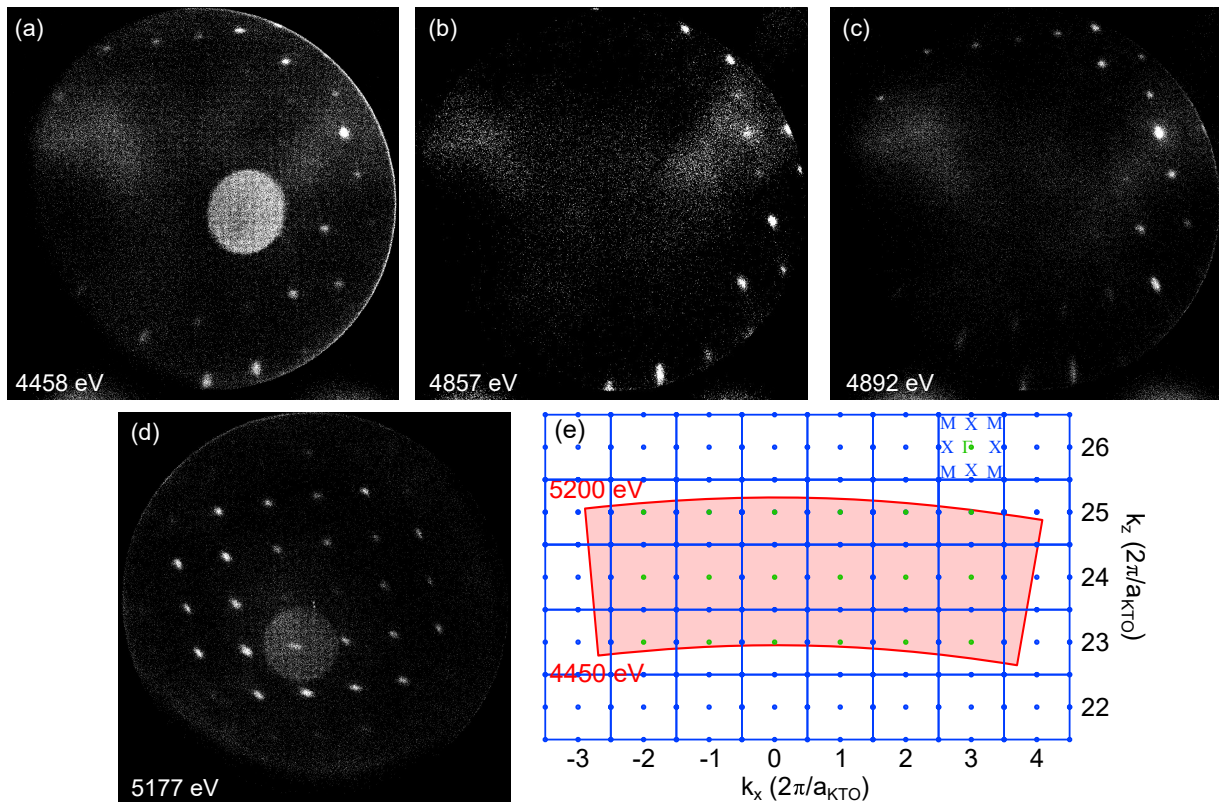


Figure 6.2: (a)-(d): Fermi surface maps taken at photon energies of 4458 (a), 4857 (b), 4892 (c), and 5177 eV (d). For the latter the lens potentials were further optimized. (e) Calculated with Eqs. 3.4 and 3.5 sketch of the $k_x - k_z$ -map. The used photon energies cover the Γ -points of the 23rd, 24th, and 25th BZ in k_z -direction.

First, the second order was corrected and afterwards, the image was slightly rotated clockwise, the cushion distortion was corrected by a nonlinear radial transformation and also some shearing effects were removed. Finally, for better clarity the color scheme was adjusted. The result is shown in Fig. 6.3 (a). As discussed in Sec. 5.2.2, the k -image has on the one hand an intensity difference between the center and the edges, originating from the measured final state sphere with a specific curvature, which indicates a distinct k_z -dependence of the electronic structure, i.e., a three-dimensional nature. On the other hand the left side of the Fermi map has a higher intensity than the right, since the sphere does not cut through the BZ at the same k_z -values on the left and right side due to the photon momentum. Also matrix element effects may play a role. The former leads to a better or worse overlap between the sphere—with a certain width due to the finite energy resolution of the incoming photon beam—and the Γ -points. Nevertheless, the Γ -points are clearly visible and exhibit a square-like arrangement, matching the cubic KTO lattice. In Fig. 6.3 (b) (i) the band map along the k_x -direction is plotted together with calculations based on the tight-binding model from Ref. [20], on the left side for bulk KTO, and on the right side for a confining wedge potential at the surface of KTO. Although for these measurements the higher resolution Si(311) monochromator crystal pair was used, granting an energy resolution of about 150 meV (at about 5.2 keV, see also Fig. 3.5), the individual bands cannot be resolved. Nevertheless, the heavy d_{yz} -band for bulk KTO is not visible towards the BZ boundary, supporting the claim of Ref. [31] that the electronic structure of the buried electron system is not that of an n -doped KTO crystal, but rather reflects that of a q2DES confined to the interface. This claim can be corroborated further by the data recorded with the momentum microscope, when also the band map in k_y -direction is taken into account, which is shown in Fig. 6.3 (b) (ii). Also in this direction—perpendicular to the k_x direction—the symmetry equivalent heavy d_{xz} -band is not visible. Thus, the absence of a spectral signal of a heavy d_{yz} -band is not ascribed to matrix element effects [23], but is likely due to the fact that the corresponding states indeed steeply disperse towards E_F , supporting the claim that the band structure of the buried electron system does not resemble the one of an n -doped, bulk-like KTO crystal. The observed electronic band structure in the $k_x - k_z$ -map of Fig. 4 (c) in Ref. [23] with a three-dimensional symmetry in momentum space suggests a finite spread of the conduction channels into the KTO substrate, which at first glance seems to contradict the conclusions drawn above and also those from depth-profiling of the q2DES by angle-dependent HAXPES in Ref. [23] that the Ta $5d$ electrons are indeed confined to the interface.

To reconcile these seemingly inconsistent findings we analyze the k -resolved data with respect to the dimensional character of the interfacial charge carriers. The underlying idea is that, according to the Heisenberg principle, spatial confinement of a particle in z -direction converts to an uncertainty in k_z , i.e., k_z is no longer a good quantum number for the quantum state of an electron whose motion is confined in z -direction. Instead, its quantum state in k -space is characterized by a probability amplitude $\Phi(k_z)$ which is the Fourier transform of the electron's wave function $\Psi(z)$. To estimate the dimensional character of the charge carriers along these lines, we compare—as described in Ref. [238]—in the following the Fermi surface broadening in k_x -direction to those in k_z from Ref. [23]. To determine the k_x -broadening, the photoemission intensity map of BZ $(-1\ 1)$ at $k_z = 25 \cdot 2\pi/a_{\text{KTO}}$

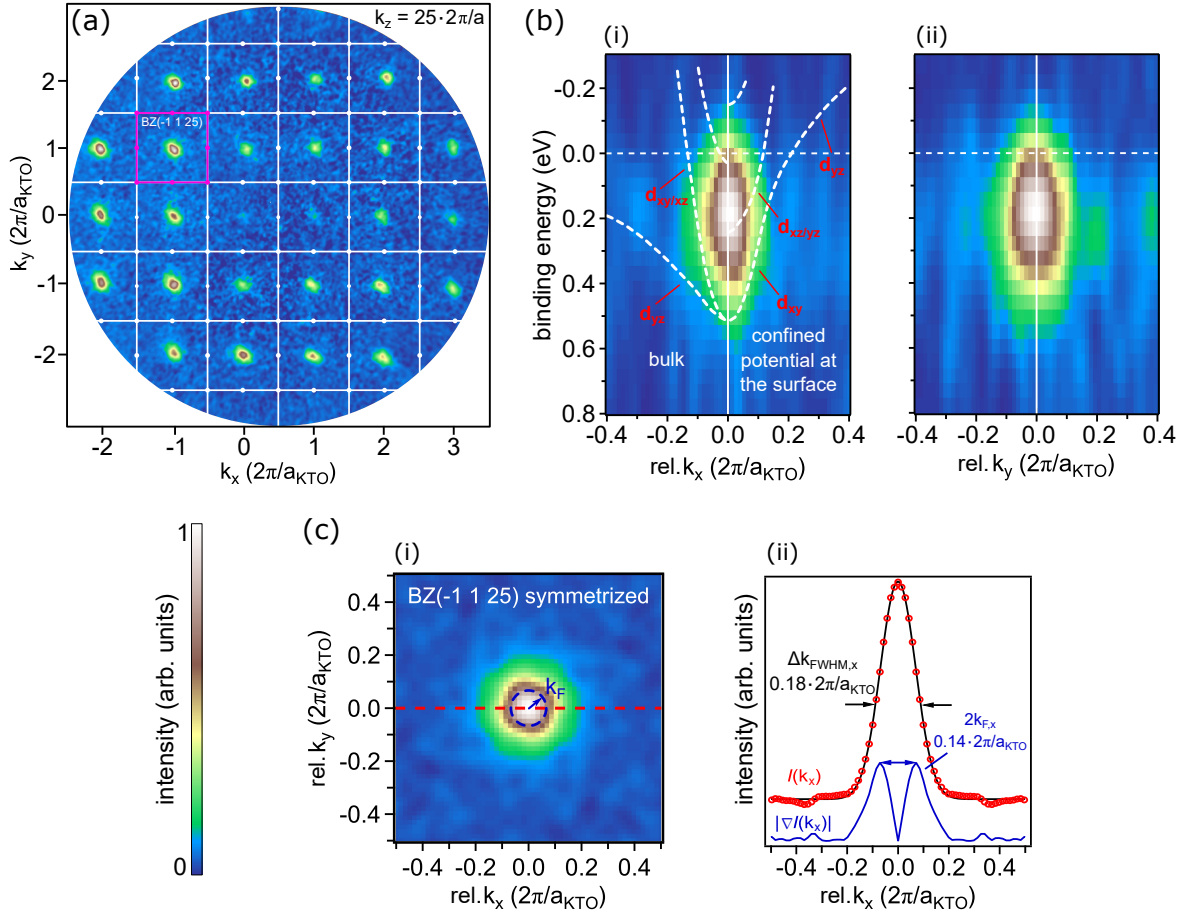


Figure 6.3: (a) Fermi surface map taken at a photon energy of 5177 eV after correcting minor distortions and removing the second order. In purple the BZ(-1 1 25) is denoted. (b): (i) Band map of the Γ -point of BZ(-1 1 25) along the k_x -direction. Calculations from Ref. [20] are shown for bulk KTO (left side) and for a confined wedge potential at the surface of KTO (right side). (ii) Band map in k_y -direction, perpendicular to the k_x -direction. (c): (i) $k_x - k_y$ -map of the symmetrized Γ -point from BZ(-1 1 25). (ii) Corresponding line profile (red circles) along the red dashed line in (a). The Gaussian fit in black shows a FWHM of $0.18 \cdot 2\pi/a_{\text{KTO}}$. The blue line denotes the derivative of the line profile and yields a value for k_F of $0.07 \cdot 2\pi/a_{\text{KTO}}$.

[see Fig. 6.3 (a)] was symmetrized according to the four-fold rotational symmetry of the KTO substrate to eliminate the influence of geometrical matrix element effects. The result is displayed in Fig. 6.3 (c) (i). Since we do not resolve the Fermi surface contours, we take the entire extension of the Fermi surface as the benchmark, defined by the full width at half maximum (FWHM) of the cross section profile along the red line, which is shown in Fig. 6.3 (c) (ii). A comparison with that along k_z (taken from Ref. [23]) reveals that they are essentially equal, viz., $\Delta k_{\text{FWHM},x} \approx \Delta k_{\text{FWHM},z} = 0.17 \cdot 2\pi/a_{\text{KTO}}$. Thus, no confinement induced broadening of the perpendicular wavevector is deducible from the measurements. Inversely, for a broadening to be deducible from the measurements it had to be larger than the experimental k -resolution. Hence, since no additional broadening along k_z can be resolved, it must be smaller than the experimental resolution, which sets a lower limit of

$1/\Delta k_{\text{res}} \approx 10 \text{ \AA}$ on the extension of the wavefunctions of the electrons, forming the q2DES, along the z -direction.

Taking therefore this value as granted, there is another independent way to estimate the dimensional character of the interface electron system using a simple argument. The dimensionality of an electron system is not solely determined by its extension in the confinement direction, L_z , but rather by the ratio of the extension and the Fermi wavelength of the electrons, $\lambda_{\text{F},z}$ —derived from the modulus of the derivative of the Gaussian fit to be $0.07 \cdot 2\pi/a_{\text{KTO}}$ —, with the dimensional character becoming three-dimensional if $L_z \gg \lambda_{\text{F},z}$ and two-dimensional for $L_z \ll \lambda_{\text{F}}$ [239–241]. Thus $\lambda_{\text{F},z} = \frac{2\pi}{k_{\text{F},z}} \approx \frac{2\pi}{k_{\text{F},x}} \approx 57 \text{ \AA}$ and $L_z \approx \frac{2\pi}{\Delta k_{\text{FWHM},z}} \approx \frac{2\pi}{\Delta k_{\text{FWHM},x}} \approx 22 \text{ \AA}$, which gives a ratio of ≈ 0.39 , placing the q2DES somewhere between the pure 2D and 3D limits. For the determination of $k_{\text{F},z}$, we set—based on the findings above— $k_{\text{F},z} = k_{\text{F},x}$, and take the modulus of the gradient of the photoemission intensity map as measure for $k_{\text{F},x}$ [see Fig. 6.3 (c)]. This method was shown in Ref. [242] to give accurate results for the Fermi vector even if large energy intervals are used for integration to generate a Fermi surface map.

6.3 Summary

It has been shown that metallicity can be induced in the KTO surface by depositing disordered LAO on top of it. The formed buried electron system can be inferred from the emergent Ta^{4+} shoulder in the Ta $4f$ spectrum of a dLAO/KTO sample. The generated Ta $5d$ carriers granting metallicity can be seen directly at E_{F} . Performing HARPES at cryogenic temperatures indeed allows for the momentum-resolved study of this electron system and exhibits the expected square-like arrangement of the Γ -points within the repeated BZ scheme. From the study of the bands around these Γ -points, occupied heavy bulk-like d_{yz} - and d_{xz} -bands cannot be resolved, concluding that they are indeed strongly dispersing towards E_{F} and the electron system is confined to the surface of KTO. By evaluating the width of the Fermi surface around the Γ -points, the extension of the wave function of the electrons at the interface in k_z -direction can be deduced to be $\approx 22 \text{ \AA}$ and the Fermi wavevector to be 57 \AA , yielding a ratio of the two quantities of ≈ 0.39 . This is in good agreement with previous findings acquired with an HDA and conclude that the electron system is indeed *quasi* two-dimensional. These results demonstrate that with the TOF-microscope commissioned within this thesis the momentum-resolved electron structure of a *buried electron system only 2 nm thick* can be successfully studied using HARPES.

7 Determination of the Valence-Band Spin Polarization of Magnetite

In Sec. 2.2.4 the necessity of using high excitation energies for the determination of the bulk spin polarization of magnetite was already discussed. In the following, the detailed characterization of the studied sample using a variety of different methods including electron diffraction, laboratory-based spin- and k -integrated photoemission, as well as X-ray magnetic circular dichroism is presented. Finally, using the TOF-based microscope with integrated spin-filter, within a spin-resolved photoemission study of the valence band of magnetite, its polarization and spin-resolved density of states (spin-DOS) near the Fermi edge are determined and compared with previous theoretical and experimental studies that were discussed in Sec. 2.2.2.

7.1 Thin Film Growth and Characterization of $\text{Fe}_3\text{O}_4(111)$ on $\text{ZnO}(0001)$

High quality $\text{Fe}_3\text{O}_4(111)$ films of 30 nm thickness were grown on $\text{ZnO}(0001)$ substrates by molecular beam epitaxy as described in Ref. [243]. Iron was evaporated from a high temperature effusion cell in an oxygen atmosphere of about $3.5 \cdot 10^{-6} - 7.0 \cdot 10^{-7}$ mbar while the substrate was kept at a temperature of 400 °C. These growth parameters are crucial because of the many stable iron oxide compounds that exist besides magnetite. [244].

In a previous study we have already shown by measuring with a superconducting quantum interference device (SQUID) that our magnetite films show a spin-reorientation transition at 128 K, which is known to lie approximately 10 K above the actual Verwey transition temperature and is comparable to those observed in bulk single crystals [243]. Furthermore, X-ray diffraction (XRD) ω - 2θ scans and rocking curves exhibit nearly completely relaxed growth on ZnO and single crystal quality, as indicated by a full width at half maximum of the rocking curves of only 0.04° [243, 245].

7.1.1 Low and High Energy Electron Diffraction

To further check the crystalline quality of the films, *in situ* LEED was performed [see Fig. 7.1 (a)]. The sharp hexagonal 2×2 LEED pattern, showing the reciprocal primitive cells of the oxygen (red) and iron (blue) sublattices, confirms the formation of an atomically long-range ordered $\text{Fe}_3\text{O}_4(111)$ surface [246].

While LEED essentially yields information on the structural quality and symmetry of the very surface, hXPD, being based on the forward scattering of photoelectrons, gives detailed information about the geometrical structure of subsurface atomic layers reaching far into the bulk [218].

Figure 7.1 (b) displays on the left side the measured hXPD patterns for the Fe 3*p* and O 2*p* core levels along with simulations on the right side, based on the many-beam dynamical theory of electron diffraction [215]. The hXPD patterns of Fe 3*p* and O 2*p* were measured with excitation energies of 5204 eV ($E_{\text{kin}} = 5150$ eV) and 5000 eV ($E_{\text{kin}} = 4993$ eV), respectively. The simulations were carried out at the same energies. The good agreement of theory and experiment confirms the good structural quality of the sample also in the bulk and supports the claim of a truly bulk-sensitive measurement at these photon energies.

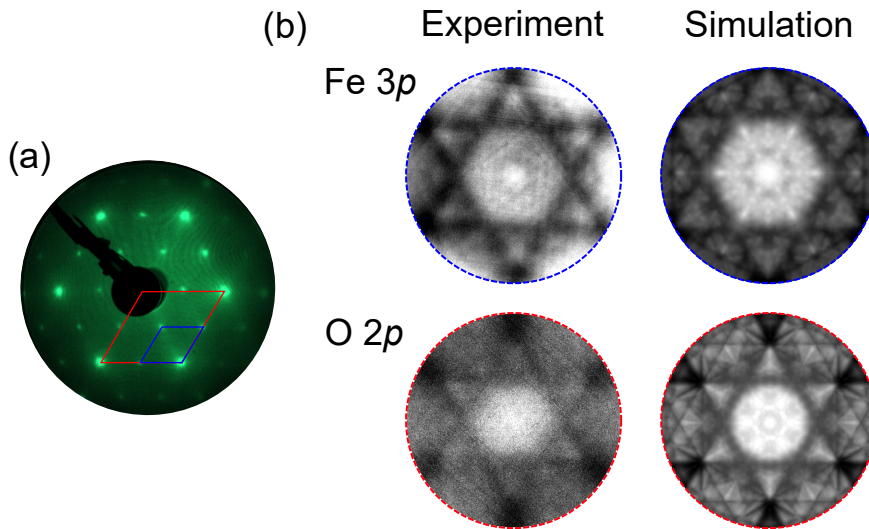


Figure 7.1: (a) LEED pattern (98.5 eV) of a freshly grown magnetite film, showing the reciprocal primitive cells of the oxygen (red) and iron (blue) sublattices. (b) hXPD patterns of the Fe 3*p* ($E_{\text{kin}} = 5150$ eV) and O 2*p* ($E_{\text{kin}} = 4993$ eV) core levels: experimental data on the left and calculated diffraction patterns on the right are in good agreement, confirming the excellent structural quality of the film and also supporting the claim of bulk sensitivity of the measurements. The hXPD patterns cover an angle range of $\pm 9^\circ$.

7.1.2 X-ray Photoelectron Spectroscopy

In addition, immediately after epitaxial growth within the same vacuum system XPS using Al K_α radiation and an Omicron EA 125 HDA was performed. In Fig. 7.2 (a) the Fe 2*p* core-level spectrum is shown, exhibiting the characteristic line shape of magnetite as originating from the Fe²⁺ and Fe³⁺ ions of this mixed-valency compound including corresponding charge-transfer (CT) satellites and is markedly distinct from other iron oxides [244]. In (b) the XPS spectrum of the valence band is compared to an *ex situ* spin-integrated photoemission spectrum of the same sample recorded with the TOF microscope at the hard X-ray beamline P22 at the synchrotron PETRA III, DESY (Hamburg, Germany) [247]. Due to the better energy resolution of the TOF instrument in combination with the highly brilliant

synchrotron radiation, the Fe $3d$ states at E_F are less broadened and hence appear more pronounced than in the spectrum taken with the laboratory-based XPS setup. Otherwise, the different spectral lineshapes can be explained by the relative change in the photoionization cross sections of the O $2p$ and Fe $3d$ states (see Sec. 3.3) that are hybridized with each other. Nevertheless, for both photon energies the predominant contribution of the Fe $3d$ states at the Fermi level remains clearly distinguishable from the mainly O $2p$ -derived valence-band spectral weight at higher binding energies.

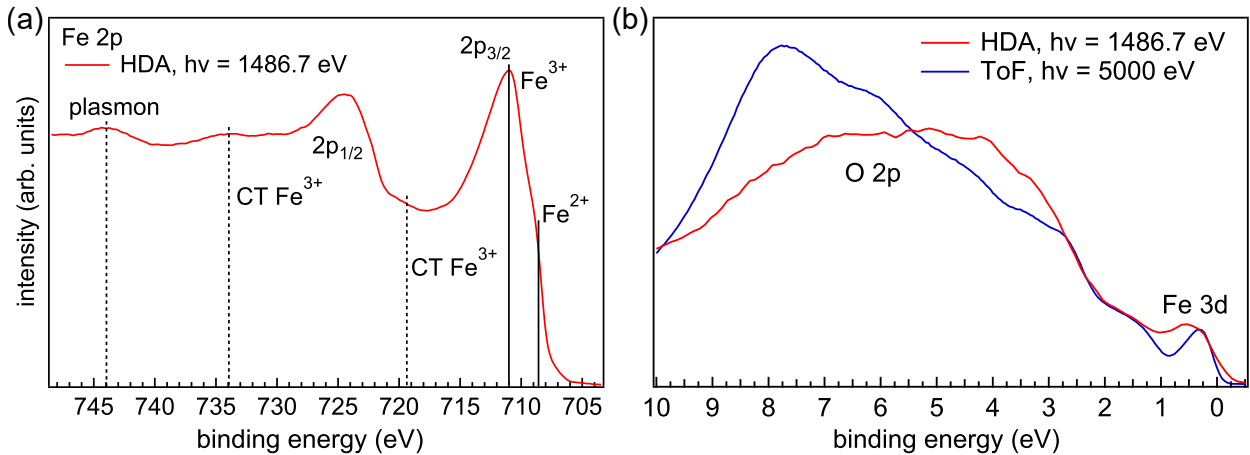


Figure 7.2: (a) Fe $2p$ core-level spectrum measured with Al K_α radiation, showing Fe^{2+} and Fe^{3+} contributions due to the mixed valency of magnetite as well as charge-transfer (CT) satellites. (b) Hard X-ray (blue) and laboratory-based (red) valence-band spectra of the same magnetite film. The Fe $3d$ states at E_F are clearly distinguishable from the O $2p$ valence band.

7.1.3 X-ray Magnetic Circular Dichroism

Furthermore, XMCD has been measured on an LN_2 cooled film in total electron yield mode at the TEMPO beamline (SOLEIL, France) to establish magnetic ordering. The blue and red spectra in Fig. 7.3 reflect the absorption measured at the Fe $L_{2,3}$ edge ($2p \rightarrow 3d$ transition) with different helicity (parallel σ_+ and antiparallel σ_- with respect to the in-plane magnetization). Both curves were normalized by the mirror current I_0 , which is a measure for the incident photon flux. The absorption spectra and the resulting XMCD signal $[(\sigma_+ - \sigma_-) \cdot 2]$, corrected for the experimental geometry with the beam incidence under 45° relative to the surface normal], which is shown as green dashed line in Fig. 7.3^{viii}, are in very good agreement with other theoretical and experimental studies on magnetite thin films [248–252]. The three peaks in the XMCD signal thereby represent the Fe ions on the Fe_{oct} sublattice (a and c) and the Fe^{3+} ions on the Fe_{tet} sublattice (b).

^{viii}Note that the sample could not be fully magnetized *ex situ* and had to be measured in remanence due to technical limitations. Hence, the XMCD signal is weaker compared to previously published absorption spectra. Nevertheless, the lineshape of the XMCD signal is in very good agreement with those data.

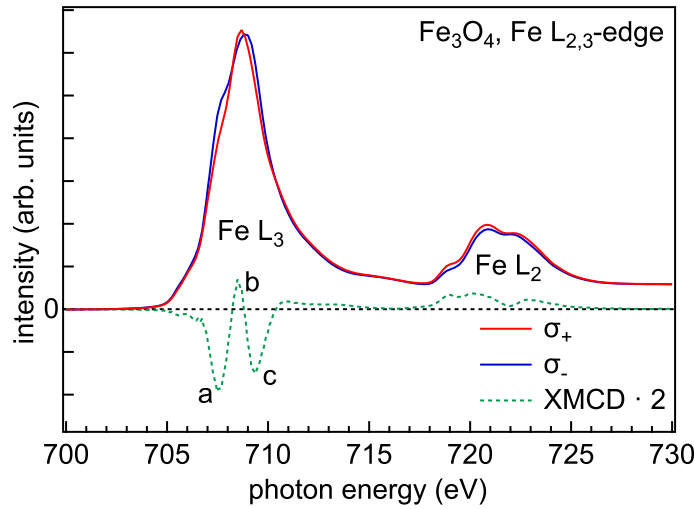


Figure 7.3: XMCD measured at the Fe $L_{2,3}$ absorption edge. The blue and red curves reflect the absorption for different helicity σ_+ and σ_- , respectively. Both curves were normalized by the mirror current I_0 . The resulting XMCD signal is shown as green dashed line (multiplied by 2).

Summary

To summarize this section, SQUID and XRD measurements from a previous study done by our group [243, 245] as well as LEED, hXPD, XPS, and XMCD establish the high quality of the Fe_3O_4 films in terms of bulk and surface crystallinity, magnetic ordering, and stoichiometric composition. They hence can be regarded as representative for bulk properties similar to single crystals.

7.2 Spin-Resolved Photoemission of the Valence Band

For this photoemission experiment the spin-dependent reflectivity at the surface of an iridium single crystal was used as described in Sec. 5.2 to gain information on the photoelectron spin. For the here used instrumental geometry, the strongest spin-sensitivity is achieved if the photoelectrons are decelerated to a kinetic energy of about 12.5 eV when impinging on the spin-filter crystal, making the spin-dependent scattering extremely surface sensitive. Therefore, prior to the spin-resolved measurements the surface of the iridium spin-filter crystal was freshly prepared as described in Sec. 5.1.2.1.

Although the microscope allows for simultaneous spin- and k -resolved mapping of the photoelectrons, due to the weak dispersion of the Fe $3d$ bands, their momentum dependence cannot be resolved [253]. Therefore, the spin-resolved data are integrated over the area covered by the spin-filter crystal ($\approx 7 \text{ \AA}^{-1}$ in k_x - and $\approx 4 \text{ \AA}^{-1}$ in k_y -direction), which can be seen in the detector image in Fig. 7.4 (a) as orange dashed oval, granting a higher signal-to-noise ratio due to higher count rates. The sample was cooled down to a temperature of $\approx 30 \text{ K}$ in order to avoid magnetic fluctuations and—as a positive side effect—to reduce the Debye-Waller factor that determines the strength of direct transitions in relation to phonon-

induced thermal scattering contributions. The cooled sample was then magnetized in-plane (I^+) with a permanent magnet. The applied field amounted to 1 Tesla parallel to the film and to the quantization axis of the spin detector, large enough to drive the sample into saturation. The valence band was then measured in remanence with an excitation energy of $h\nu = 5.0 \text{ keV}$ ^{ix}, leading to a photoelectron inelastic mean free path of $\approx 70 \text{ \AA}$ (see Sec. 3.3) and an energy resolution of $\approx 620 \text{ meV}$ —using the Si(111) monochromator crystal pair for maximum photon flux (see Sec. 3.4). Then the sample was magnetized in the opposite direction (I^-) and measured again. Figure 7.4 (b) shows the spectra for the two opposite in-plane magnetization directions—as extracted from the measured $I(P_x, E_{\text{kin}}, k_x, k_y)$ data set—for the relevant energy range from E_F up to 5 eV. The inset shows the entire acquired range up to 10 eV with no visible difference in the spectral shape for binding energies above 3 eV.

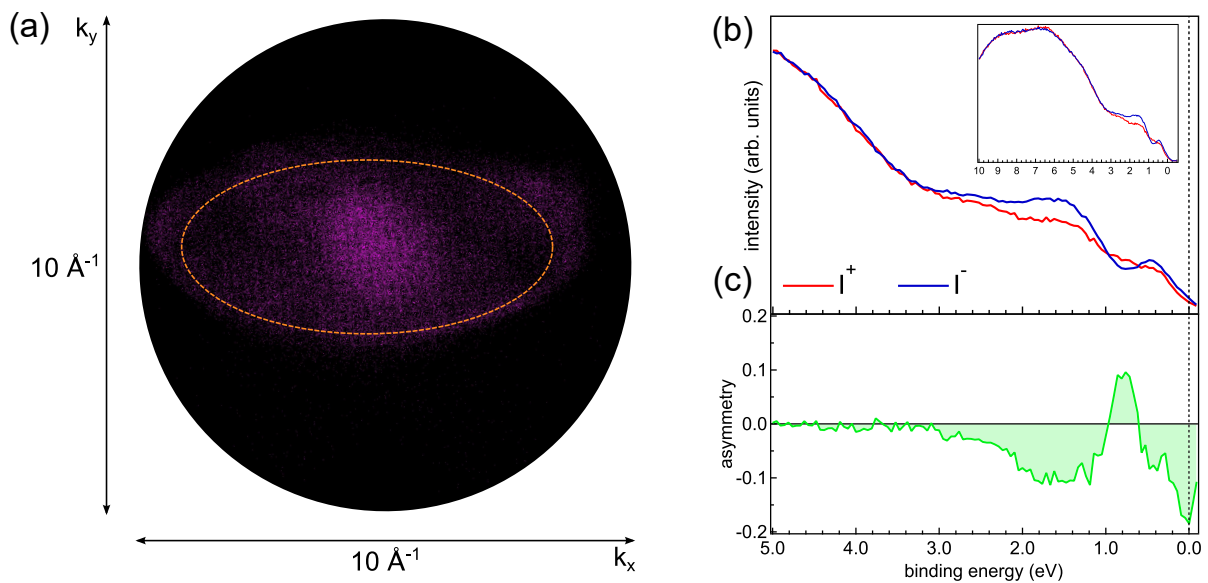


Figure 7.4: (a) Detector image of the spin-branch: While the detector covers an reciprocal space of 10 \AA^{-1} in both directions, the photoelectron intensity is concentrated in an oval area, reflecting the surface of the crystal as seen from the detector under an angle of 56° (image has been colorized for better visibility). (b) Extracted valence-band spectra of magnetite integrated over the orange dashed oval ($\approx 7 \text{ \AA}^{-1}$ in k_x - and $\approx 4 \text{ \AA}^{-1}$ in k_y -direction) for both magnetizations I^+ and I^- . Both spectra were normalized by the same O $2p$ spectral weight, since no asymmetry is expected here. (c) Resulting asymmetry calculated with Eq. 4.36.

In contrast, clear differences between the two magnetizations are seen for smaller binding energies. The resulting intensity asymmetry A , defined by Eq. 4.36, is plotted in Fig. 7.4 (c). It is zero above 3 eV where the O $2p$ valence band dominates. For smaller binding energies and with predominantly Fe $3d$ states contributing, the asymmetry first becomes negative and switches sign between 0.95 and 0.60 eV with a maximum at 0.80 eV. Closer to the Fermi level the asymmetry turns negative again and assumes a maximum negative value at E_F .

^{ix}The photon energy of 5 keV was chosen as a good compromise between the dropping cross section at higher photon energies and the increase of third-order radiation from the undulator at lower energies.

The conversion of the measured asymmetry A into an actual spin polarization P involves the Sherman function, as described by Eqs. 4.7 and 4.36. It is important to realize that in our specific experimental approach the explicit *energy dependence* of the Sherman function $S = S(E)$ is required, in contrast to conventional spin-detectors operated at a fixed energy only. Employing TOF energy recording, all photoelectrons in the measured energy window are reflected off the spin-filter crystal essentially simultaneously, i.e., at different scattering energies. For the data in Fig. 7.4 the electron optics was set in such a way that photoelectrons originating from the maximum of the Fe $3d$ peak at ≈ 0.5 eV reach the spin-filter crystal at a kinetic energy where its Sherman function assumes its maximum (≈ 12.5 eV) [146]. Consequently, electrons at higher (lower) binding energy get scattered at lower (higher) kinetic energy, with subsequently different spin efficiency as captured by $S(E)$ and hence necessitating a careful calibration of the Sherman function.

Such a calibration is best achieved on a material system with known spin polarization. Here we chose EuO whose Eu $4f$ states have been demonstrated to display a spin polarization of 100% [254, 255]. Based on this value the experimental spin asymmetry of the $4f$ states of a thin EuO film [255] for scattering energies between 9.5 and 13.2 eV was measured, and the associated values of the Sherman function were calculated. Figure 7.5 depicts the corresponding data points together with a spline interpolation. The Sherman function assumes its maximum around 12.5 eV while at lower kinetic energies, i.e., higher binding energies, $S(E)$ is significantly decreasing and even changes its sign at about 10.9 eV.

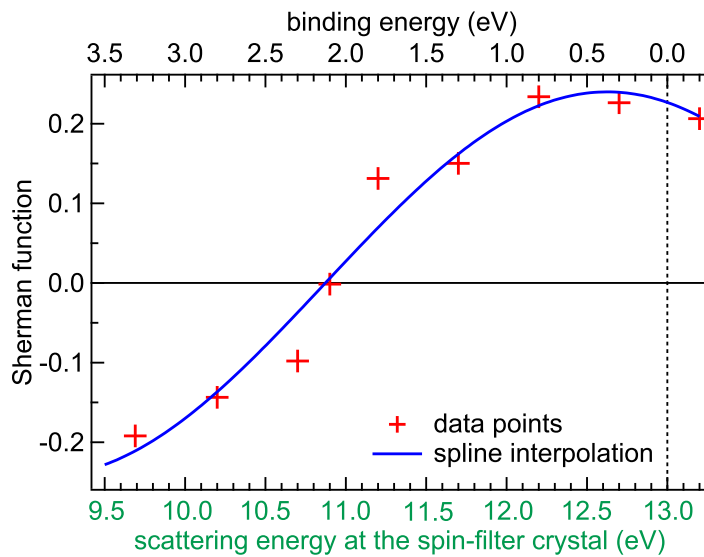


Figure 7.5: Energy dependent Sherman function $S(E)$, calibrated using the known 100% spin polarization of the Eu $4f$ states of an EuO thin film. The bottom axis refers to the actual scattering energy at the spin-filter crystal. In the top axis these values are converted to a binding energy scale, as adapted to the spin-resolved magnetite spectra of Fig. 7.4 (b).

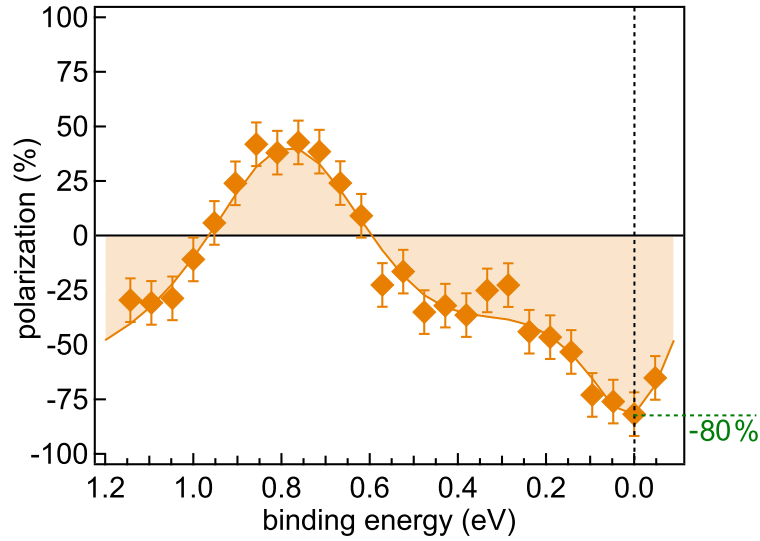


Figure 7.6: Spin polarization of the magnetite film, calculated with Eq. 4.36 (the line serves as guide to the eye). It is negative at $E_F = 0$ eV with a value of -80% . Between 0.60 eV and 0.95 eV, there is a sign change of the polarization. The error bars denote the statistical error.

Based on this calibration of the Sherman function, the energy-dependent spin polarization $P(E)$ of the magnetite film can finally be determined from Eqs. 4.7 and 4.36. The result is shown in Fig. 7.6. As predicted by theory, the spin polarization at E_F is negative. With higher binding energies, the absolute value of the spin polarization decreases and switches sign at 0.60 eV. It exhibits a maximum with further increasing binding energies and becomes negative again at 0.95 eV. Since the Sherman function has a zero at about 10.9 eV, corresponding to a binding energy of 2.1 eV in this study, the spin polarization unphysically diverges around this energy, and hence the focus in Fig. 7.6 is on smaller binding energies from 1.2 eV up to the Fermi level, where the Sherman function does not vary strongly and the polarization is not affected by the zero in S . For binding energies above 3 eV the polarization becomes zero (see Fig. 7.4 (c)).

To give a quantitative estimate of the spin polarization at E_F from the measured asymmetry, it must be mentioned that the measurements were performed at ≈ 30 K, i.e., below the Verwey temperature, at which a metal-insulator transition takes place and a small gap of about 50 meV with respect to E_F opens [95]. So, strictly speaking, there are no states at E_F and thus no defined spin polarization. However, the finite energy resolution of about 600 meV in this experiment transfers detectable spectral weight to the Fermi level, resulting in a finite polarization signal. The experimental spin polarization at the Fermi level $P(E_F)$ can now be determined from Fig. 7.6 to be -80% (dashed green line).

The statistical error for the asymmetry shown in Fig. 7.4 (c) is estimated from Eq. 4.39 with the count rates I^+ and I^- in a 50 meV energy interval near E_F for both magnetization directions, $\Delta A = \sqrt{4I^+I^-}/I^3 = 0.012$. The statistical error of the Sherman function related to the calibration measurement is in the same order of magnitude, $\Delta S = 0.013$ (see Fig. 7.5). The statistical error of the polarization value results from the sum of the relative errors, $\Delta P/P = \Delta A/A + \Delta S/S$. Near the Fermi energy the statistical error amounts

to $\Delta P/P = 0.13$ and $\Delta P = 0.104$. As additional systematic errors, it has to be taken into account (i) a reduced remnant magnetization compared to the intrinsic magnetization, and (ii) the finite energy resolution. (i) As the sample was measured in remanence, the magnetization M_r and thereby the spin polarization could be lower than the intrinsic magnetization M_s . Previous SQUID magnetometry on similarly prepared samples result in $M_r/M_s = 0.64$ [243]. Therefore, the intrinsic spin polarization could be larger than the measured value. (ii) Due to the specific shape of the energy-dependent polarization data in Fig. 7.6 (with a maximal positive spin polarization at 0.8 eV, a sign change at 0.6 eV, and a maximal negative spin polarization at the Fermi energy), a finite energy resolution tends to reduce the measured spin polarization at E_F . Therefore, the measured spin polarization at E_F represents a *lower limit* of its true absolute value and strongly points to a full spin polarization at E_F of -100% , supporting the assumption of magnetite being a half-metallic ferromagnet. Considering both statistical and systematic errors, the spin polarization value at E_F amounts to $P(E_F) = -80_{-20}^{+10}\%$.

Finally, the spin-resolved density of states (spin-DOS) can be calculated from Eq. 4.37. The resulting majority and minority spin-densities are shown in Fig. 7.7 (red and blue triangles). Also shown are the results of DFT calculations by Piekarz *et al.* [79]—performed explicitly for the low temperature phase of magnetite with the monoclinic P2/c symmetry [92, 93] and including strong correlation effects on the GGA+U level—, without (solid lines) and with (dashed lines) the experimental broadening taken into account. While the experimental spin-densities overall resemble the theoretical ones, there are also notable quantitative differences. It has been argued that, in general, magnetite should be considered a correlated electron system, casting a description by DFT and its findings of half-metallicity into doubt [106]. Furthermore, the excitation of spin waves [103, 109, 256, 257] and the formation of polarons [84], which both are not captured by DFT calculations, were put forward in previous experimental studies to explain a smaller spin polarization observed in experiment than predicted by DFT. Such effects also will affect the detailed experimental lineshapes in the near- E_F region.

7.3 Summary and Discussion

The bulk spin polarization of magnetite has been measured by spin-resolved hard X-ray photoelectron spectroscopy. For these experiments, a new generation of photoemission instrumentation has been utilized—the TOF-based momentum microscope with built-in imaging spin-filter. With this setup, it has become possible to overcome the notorious problem of ill-defined magnetite surfaces from which previous low-energy spin-resolved photoemission studies suffered. The measured spin polarization of $-80_{-20}^{+10}\%$ strongly points to a full bulk spin polarization at E_F , fully compatible with theoretical predictions from DFT that magnetite is a half-metallic ferromagnet.

From an experimental view, further advancements in instrumentation, regarding both electron and photon energy resolution, will make it possible to narrow down the experimental

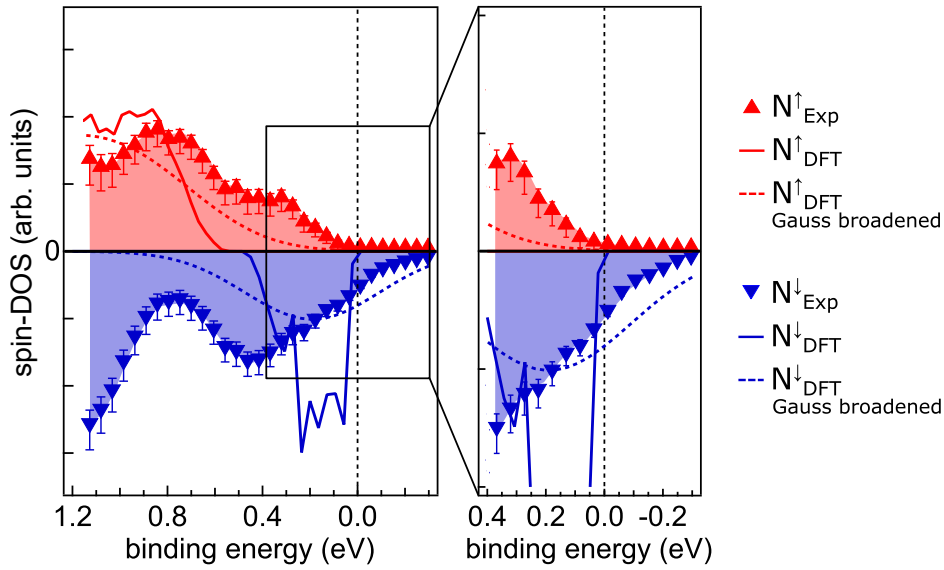


Figure 7.7: Majority and minority spin-DOS (red and blue triangles, respectively) for Fe_3O_4 , calculated from the results of Fig. 7.4 using Eq. 4.37 with error bars denoting the statistical error. Mostly minority spin states are located at E_F . The spin-DOS overall resembles those from DFT calculations (solid lines) in Ref. [79], especially upon convolution with the instrumental resolution (dashed lines).

uncertainty for the spin polarization of magnetite further^x. This will become possible by, e.g., an upgrade of the storage ring of PETRA III [258] granting a photon flux gain at the beamline P22 of about a factor of 1400 [259]. The higher intensity allows the use of the higher resolution monochromator crystal Si(311) for spin-resolved measurements, which improves the photon bandwidth at 5 keV to about 130 meV, and even better with the post-monochromator crystal Si(333)—for a given photon energy of more than 6 keV—of only 30 meV (see Sec. 3.4). In combination with faster energy recording, possible by an ultrafast DLD, the energy resolution of the microscope can also be further enhanced.

These improvements will have to be matched by improved theoretical approaches, taking properly into account both the itinerancy of the minority charge carriers at the Fermi energy as well as their correlations and coupling to the lattice degrees of freedom. Nevertheless, the results presented here point to a full bulk spin polarization near E_F , that originates from spin-down charge carriers, and thereby provide strong experimental support to the theoretical view of magnetite as a half-metallic ferromagnet.

^xNote that recently a total energy resolution (photon band width plus analyzer resolution) as good as 60 meV has been demonstrated for *spin-integrated* HAXPES operation of the same momentum microscope used here [204]. Although, the additional use of the spin-filter crystal results in a significant count rate reduction, this result represents an encouraging prospect for future *spin-resolved* HAXPES experiments.

8 Conclusion

The aim of this thesis was to push the frontiers of *hard X-ray* photoelectron spectroscopy, to enable spin- and k -resolved studies of complex oxides. To accomplish this goal, two instrumental concepts were pursued in collaboration with Prof. Schönhense's group in Mainz, which developed these concepts, and which were commissioned and characterized as part of this thesis. The first concept was to upgrade an existing hard X-ray photoemission endstation at P09, DESY, equipped with a hemispherical deflection analyzer (HDA), with an external spin detector chamber. Second, a completely newly developed k -space microscope with time-of-flight (TOF) energy recording and built-in spin filter was used for spin- and k -resolved hard X-ray photoemission.

For the upgrade of the existing endstation an external spin detector chamber with a W(001) spin-filter crystal was attached to the exit of the HDA. The spin detector is equipped with its own delayline detector (DLD) measuring the spin-filtered $I(E_{\text{kin}}, k_x)$ -array. The surface preparation of the spin-filter crystal was successfully established, the optimal scattering parameters were determined, the lifetime of the crystal surface was found to be about 30 minutes, and the imaging capabilities of the detector were optimized. However, the first spin-resolved measurements on a magnetite thin film sample were not successful. Although the sample is studied thoroughly at different energy positions within the valence band, slightly different scattering energies and azimuthal angles, a spin asymmetry of the Fe $3d$ states near the Fermi level (E_F) could not be observed. The main reason is the extremely low efficiency of the instrumental concept, since an HDA discriminates only a small fraction of all excited photoelectrons. In combination with the low reflectivity of the spin-filter, very low count rates force the use of high pass energies, which significantly deteriorates the experimental resolution. Another reason is the short lifetime of the crystal surface, which is why the crystal had to be flashed before each measurement, resulting in poor reproducibility of two consecutive measurements because the crystal temperatures were different for each measurement. Although the commissioning and characterization of the upgraded HDA-based endstation worked quite well, the low efficiency of the setup and the short lifetime of the crystal surface prevent its successful implementation for spin-resolved hard X-ray photoemission.

Hence, the concept of TOF energy recording was pursued, again in collaboration with Prof. Schönhense's group. This TOF method integrated in a momentum microscope allows for much higher count rates due to the absence of entrance and exit slits. Compared to tungsten, the use of an Ir(100) spin filter crystal is characterized by a significantly longer surface lifetime of several weeks, which eliminates the need for regular crystal flashing and thus ensures high reproducibility of successive measurements. Due to the increased dimensionality of the recording scheme the set up k -space TOF microscope was found to cover

up to 16 Brilluoin zones (BZs) at 6 keV photon energy. The high count rates allow for the acquisition of valence-band maps within several 10 mins, and core levels and corresponding X-ray diffraction pattern even within minutes. In this way, the low reflectivity of the crystal and the low electron discrimination of the HDA-based concept are compensated, making the TOF concept clearly superior. Although a problem with higher order radiation was encountered during commissioning, several approaches to the existing setup were found to suppress such signals, and further two different instrumental advancements were discussed involving a chicane or a combination of TOF energy recording with the energy filtering capabilities of an HDA.

Having identified the second instrumental concept as pioneering, the electron system (q2DES) on the *buried* surface of KTaO_3 (KTO) was studied in terms of its dimensional character. Furthermore, the *bulk* spin polarization of magnetite (Fe_3O_4) was determined. Both experiments using the newly established spin- and k -resolved TOF momentum microscope.

The appearance of a Ta^{4+} shoulder in the Ta $4f$ core-level spectrum, as well as the Ta $5d$ spectral weight at the Fermi level (E_F) obtained by measuring a KTO substrate covered with a 1.6 nm thick disordered LaAlO_3 (dLAO) film, prove the formation of a q2DES at the KTO surface. Its investigation by means of k - or *angle-resolved hard X-ray* photoelectron spectroscopy (ARPES) at 5177 eV photon energy revealed up to 26 BZs with a square-like arrangement of the Γ -points. From the evaluation of the band maps in k_x - and k_y -direction neither the heavy d_{yz} - nor d_{xz} -band could be resolved towards the BZ boundary indicating a confinement of the q2DES to the surface of KTO. By further evaluation of the Fermi vector in the x -direction, $k_{F,x}$, which is related to the expansion in the confinement direction, L_z , yielding a factor of ≈ 0.39 and with the results of a previous study that places the q2DES in the regime of bulk KTO based on their results from measured $k_x - k_z$ -maps, the dimensional character of this q2DES consequently lies somewhere between the pure 2D and 3D limits.

The excellent quality of the magnetite sample was shown by means of electron diffraction and laboratory-based spin- and k -integrated photoemission. Overcoming the problem of low efficiencies of previous experimental approaches by using TOF energy recording, imaging spin-filtering and multichannel electron detection, it was possible for the first time ever to measure the valence band of magnetite by *spin-resolved hard X-ray* photoelectron spectroscopy (spin-HARPES) and its true *bulk* spin polarization was determined in the near- E_F region with a maximum negative value of $-80_{-20}^{+10}\%$ directly at E_F . These findings—reflecting the statistical and systematic errors of the measurement—are in good agreement with theoretical predictions based on density-functional theory of magnetite being a half-metallic ferromagnet with a spin polarization at E_F of -100% and therefore just minority charge carriers contribute to the metallic behaviour of magnetite.

Both results show that in the hard X-ray regime TOF-based energy recording has tremendous advantages compared to the use of an HDA especially in combination with an imaging spin-filter in terms of maximizing electron count rates. With future developments also the obstacles of higher order radiation can be solved and with the new generation of diffraction limited electron synchrotrons and new ways for nano-focussing of the photon beam, the power of TOF-based spin- and k -resolved microscopy will reach a new level for photoemission experiments.

Bibliography

- [1] P. Debye and A. Sommerfeld, *Physikalische Zeitschrift* **17**, 507 (1916).
- [2] O. Stern, *Zeitschrift für Physik* **7**, 249 (1921).
- [3] G. E. Uhlenbeck and S. Goudsmit, *Naturwissenschaften* **13**, 953 (1925).
- [4] W. Pauli, *Zeitschrift für Physik* **31**, 765 (1925).
- [5] P. Dirac, *Proceedings of the Royal Society A* **117**, 610 (1928).
- [6] J. Kessler, *Polarized Electrons* (Springer-Verlag Berlin, 1985).
- [7] J. Kirschner and R. Feder, *Physical Review Letters* **42**, 1008 (1979).
- [8] J. van Klinken, *Nuclear Physics* **75**, 161 (1966).
- [9] C. Liu, X. Yan, D. Jin, Y. Ma, H.-W. Hsiao, Y. Lin, T. M. Bretz-Sullivan, X. Zhou, J. Pearson, B. Fisher, J. S. Jiang, W. Han, J.-M. Zuo, J. Wen, D. D. Fong, J. Sun, H. Zhou, and A. Bhattacharya, *Science* **371**, 716 (2021).
- [10] J. B. Goodenough, *Progress in Solid State Chemistry* **5**, 145 (1971).
- [11] C. N. R. Rao, *Annual Review of Physical Chemistry* **40**, 291 (1989).
- [12] J. Mannhart and D. G. Schlom, *Science* **327**, 1607 (2010).
- [13] A. Ohtomo and H. Y. Hwang, *Nature* **427**, 423 (2004).
- [14] Y. Chen, N. Pryds, J. E. Kleibeuker, G. Koster, J. Sun, E. Stamate, B. Shen, G. Rijnders, and S. Linderoth, *Nano Letters* **11**, 3774 (2011).
- [15] W. Meevasana, P. D. C. King, R. H. He, S.-K. Mo, M. Hashimoto, A. Tamai, P. Songsiriritthigul, F. Baumberger, and Z.-X. Shen, *Nature Materials* **10**, 114 (2011).
- [16] J. Gabel, M. Zapf, P. Scheiderer, P. Schütz, L. Dudy, M. Stübinger, C. Schlueter, T.-L. Lee, M. Sing, and R. Claessen, *Physical Review B* **95**, 195109 (2017).
- [17] N. Wadehra, R. Tomar, R. M. Varma, R. K. Gopal, Y. Singh, S. Dattagupta, and S. Chakraverty, *Nature Communications* **11**, 874 (2020).
- [18] H. Zhang, Y. Yun, X. Zhang, H. Zhang, Y. Ma, X. Yan, F. Wang, G. Li, R. Li, T. Khan, Y. Chen, W. Liu, F. Hu, B. Liu, B. Shen, W. Han, and J. Sun, *Physical Review Letters* **121**, 116803 (2018).
- [19] F. Trier, P. Noël, J.-V. Kim, J.-P. Attané, L. Vila, and M. Bibes, *Nature Reviews Materials* (2021).
- [20] A. F. Santander-Syro, C. Bareille, F. Fortuna, O. Copie, M. Gabay, F. Bertran, A. Taleb-Ibrahimi, P. Le Fèvre, G. Herranz, N. Reyren, M. Bibes, A. Barthélémy, P. Lecoeur, J. Guevara, and M. J. Rozenberg, *Physical Review B* **86**, 121107(R) (2012).

- [21] P. D. C. King, R. H. He, T. Eknapakul, P. Buaphet, S.-K. Mo, Y. Kaneko, S. Harashima, Y. Hikita, M. S. Bahramy, C. Bell, Z. Hussain, Y. Tokura, Z.-X. Shen, H. Y. Hwang, F. Baumberger, and W. Meevasana, *Physical Review Letters* **108**, 117602 (2012).
- [22] C. Bareille, F. Fortuna, T. C. Rödel, F. Bertran, M. Gabay, O. H. Cubelos, A. Taleb-Ibrahimi, P. Le Fèvre, M. Bibes, A. Barthélémy, T. Maroutian, P. Lecoeur, M. J. Rozenberg, and A. F. Santander-Syro, *Scientific Reports* **4**, 3586 (2014).
- [23] M. Zapf, M. Schmitt, J. Gabel, P. Scheiderer, M. Stübinger, G. Sangiovanni, L. Dudy, S. Chernov, S. Babenkov, D. Vasilyev, O. Fedchenko, K. Medjanik, Y. Matveyev, A. Gloskovskii, C. Schlueter, T.-L. Lee, H.-J. Elmers, G. Schönhense, M. Sing, and R. Claessen, Hard X-ray angle-resolved photoemission from a buried high mobility electron system in the disordered-crystalline LAO/KTO heterostructure, submitted to *Physical Review B*, arXiv:2110.15158 (2021).
- [24] V. M. Goldschmidt, *Die Naturwissenschaften* **14**, 477 (1926).
- [25] R. Shannon, *Acta Crystallographica Section A* **32**, 751 (1976).
- [26] D. A. MacLean, H.-N. Ng, and J. Greedan, *Journal of Solid State Chemistry* **30**, 35 (1979).
- [27] W. Knafo, C. Meingast, A. V. Boris, P. Popovich, N. N. Kovaleva, P. Yordanov, A. Maljuk, R. K. Kremer, H. v. Löhneysen, and B. Keimer, *Physical Review B* **79**, 054431 (2009).
- [28] K. Momma and F. Izumi, *Journal of Applied Crystallography* **44**, 1272 (2011).
- [29] M. Setvin, M. Reticcioli, F. Poelzleitner, J. Hulva, M. Schmid, L. A. Boatner, C. Franchini, and U. Diebold, *Science* **359**, 572 (2018).
- [30] G. E. Jellison, I. Paulauskas, L. A. Boatner, and D. J. Singh, *Physical Review B* **74**, 155130 (2006).
- [31] M. Zapf, “High-Z perovskite oxides: Thin film deposition and spectroscopic investigations”, Doctoral Thesis (Würzburg, 2019).
- [32] R. M. Cornell and U. Schwertmann, *The iron oxides: structure, properties, reactions, occurrences, and uses*, 2nd, completely rev. and extended ed (Wiley-VCH, Weinheim, 2003).
- [33] S. A. Wolf, *Science* **294**, 1488 (2001).
- [34] I. Žutić, J. Fabian, and S. Das Sarma, *Reviews of Modern Physics* **76**, 323 (2004).
- [35] S. Datta and B. Das, *Applied Physics Letters* **56**, 665 (1990).
- [36] R. Winkler and M. Oestreich, *Physik Journal* **6**, 39 (2004).
- [37] R. Winkler, *Spin-orbit coupling effects in two-dimensional electron and hole systems*, Vol. 191, Springer Tracts in Modern Physics (Springer, Berlin ; New York, 2003).
- [38] G. S. Parkinson, U. Diebold, J. Tang, and L. Malkinski, INTECH Open Access Publisher (Advanced Magnetic Materials) (2012).

- [39] G. Schmidt, D. Ferrand, L. W. Molenkamp, A. T. Filip, and B. J. van Wees, *Physical Review B* **62**, R4790 (2000).
- [40] G. Schmidt, *Journal of Physics D: Applied Physics* **38**, R107 (2005).
- [41] P. R. Hammar, B. R. Bennett, M. J. Yang, and M. Johnson, *Physical Review Letters* **83**, 203 (1999).
- [42] W. Y. Lee, S. Gardelis, B.-C. Choi, Y. B. Xu, C. G. Smith, C. H. W. Barnes, D. A. Ritchie, E. H. Linfield, and J. A. C. Bland, *Journal of Applied Physics* **85**, 6682 (1999).
- [43] F. Monzon and M. Roukes, *Journal of Magnetism and Magnetic Materials* **198–199**, 632 (1999).
- [44] S. G. Bhat and P. S. Anil Kumar, *AIP Advances* **6**, 056308 (2016).
- [45] W. H. Bragg, *Nature* **95**, 561 (1915).
- [46] C. G. Shull, E. O. Wollan, and W. A. Strauser, *Physical Review* **81**, 483 (1951).
- [47] R. J. Hill, J. R. Craig, and G. V. Gibbs, *Physics and Chemistry of Minerals* **4**, 317 (1979).
- [48] M. E. Fleet, *Acta Crystallographica Section B* **37**, 917 (1981).
- [49] P. W. Tasker, *Journal of Physics C: Solid State Physics* **12**, 4977 (1979).
- [50] C. Noguera, *Journal of Physics: Condensed Matter* **12**, R367 (2000).
- [51] T. Pohlmann, T. Kuschel, J. Rodewald, J. Thien, K. Ruwisch, F. Bertram, E. Weschke, P. Shafer, J. Wollschläger, and K. Küpper, *Physical Review B* **102**, 220411(R) (2020).
- [52] R. Pentcheva, F. Wendler, H. L. Meyerheim, W. Moritz, N. Jedrecy, and M. Scheffler, *Physical Review Letters* **94**, 126101 (2005).
- [53] L. Zhu, K. L. Yao, and Z. L. Liu, *Physical Review B* **74**, 035409 (2006).
- [54] M. Paul, M. Sing, R. Claessen, D. Schrupp, and V. A. M. Brabers, *Physical Review B* **76**, 075412 (2007).
- [55] B. D. Cullity and C. D. Graham, *Introduction to magnetic materials*, 2nd ed (IEEE/Wiley, Hoboken, N.J., 2009).
- [56] V. Melfos, B. Helly, and P. Voudouris, *Archaeological and Anthropological Sciences* **3**, 165 (2011).
- [57] M. L. Néel, *Annales de Physique* **12**, 137 (1948).
- [58] E. J. W. Verwey, *Nature* **144**, 327 (1939).
- [59] E. J. W. Verwey and P. Haayman, *Physica* **8**, 979 (1941).
- [60] E. J. Verwey, P. W. Haayman, and F. C. Romeijn, *The Journal of Chemical Physics* **15**, 181 (1947).
- [61] M. Iizumi, T. F. Koetzle, G. Shirane, S. Chikazumi, M. Matsui, and S. Todo, *Acta Crystallographica Section B* **38**, 2121 (1982).

- [62] J. M. Zuo, J. C. H. Spence, and W. Petuskey, *Physical Review B* **42**, 8451 (1990).
- [63] A. Yanase and K. Siratori, *Journal of the Physical Society of Japan* **53**, 312 (1984).
- [64] R. A. de Groot and K. H. J. Buschow, *Journal of Magnetism and Magnetic Materials* **54–57**, 1377 (1986).
- [65] Z. Zhang and S. Satpathy, *Physical Review B* **44**, 13319 (1991).
- [66] M. Pénicaud, B. Siberchicot, C. B. Sommers, and J. Kübler, *Journal of Magnetism and Magnetic Materials* **103**, 212 (1992).
- [67] V. I. Anisimov, I. S. Elfimov, N. Hamada, and K. Terakura, *Physical Review B* **54**, 4387 (1996).
- [68] A. Yanase and N. Hamada, *Journal of the Physical Society of Japan* **68**, 1607 (1999).
- [69] V. N. Antonov, B. N. Harmon, V. P. Antropov, A. Y. Perlov, and A. N. Yaresko, *Physical Review B* **64**, 134410 (2001).
- [70] V. N. Antonov, B. N. Harmon, and A. N. Yaresko, *Physical Review B* **67**, 024417 (2003).
- [71] H.-T. Jeng and G. Y. Guo, *Physical Review B* **65**, 094429 (2002).
- [72] H.-T. Jeng, G. Y. Guo, and D. J. Huang, *Physical Review Letters* **93**, 156403 (2004).
- [73] H.-T. Jeng, G. Y. Guo, and D. J. Huang, *Physical Review B* **74**, 195115 (2006).
- [74] Z. Szotek, W. M. Temmerman, A. Svane, L. Petit, G. M. Stocks, and H. Winter, *Physical Review B* **68**, 054415 (2003).
- [75] I. Leonov, A. N. Yaresko, V. N. Antonov, M. A. Korotin, and V. I. Anisimov, *Physical Review Letters* **93**, 146404 (2004).
- [76] G. K. H. Madsen and P. Novák, *Europhysics Letters* **69**, 777 (2005).
- [77] H. P. Pinto and S. D. Elliott, *Journal of Physics: Condensed Matter* **18**, 10427 (2006).
- [78] Z. Łodziana, *Physical Review Letters* **99**, 206402 (2007).
- [79] P. Piekarczyk, K. Parlinski, and A. M. Oleś, *Physical Review B* **76**, 165124 (2007).
- [80] P. Piekarczyk, A. Oleś, and K. Parlinski, *Acta Physica Polonica A* **118**, 307 (2010).
- [81] A. D. Rowan, C. H. Patterson, and L. V. Gasparov, *Physical Review B* **79**, 205103 (2009).
- [82] X. Yu, C.-F. Huo, Y.-W. Li, J. Wang, and H. Jiao, *Surface Science* **606**, 872 (2012).
- [83] R. Arras, B. Warot-Fonrose, and L. Calmels, *Journal of Physics: Condensed Matter* **25**, 256002 (2013).
- [84] W. Wang, J.-M. Mariot, M. C. Richter, O. Heckmann, W. Ndiaye, P. De Padova, A. Taleb-Ibrahimi, P. Le Fèvre, F. Bertran, F. Bondino, E. Magnano, J. Krempaský, P. Blaha, C. Cacho, F. Parmigiani, and K. Hricovini, *Physical Review B* **87**, 085118 (2013).

-
- [85] J. Noh, O. I. Osman, S. G. Aziz, P. Winget, and J.-L. Brédas, *Science and Technology of Advanced Materials* **15**, 044202 (2014).
- [86] D. Schmitz, C. Schmitz-Antoniak, A. Warland, M. Darbandi, S. Haldar, S. Bhandary, O. Eriksson, B. Sanyal, and H. Wende, *Scientific Reports* **4**, 5760 (2014).
- [87] H. Liu and C. Di Valentin, *The Journal of Physical Chemistry C* **121**, 25736 (2017).
- [88] H. Liu, G. Seifert, and C. Di Valentin, *The Journal of Chemical Physics* **150**, 094703 (2019).
- [89] O. Mounkachi, R. Lamouri, M. Hamedoun, H. Ez-Zahraouy, E. Salmani, and A. Benyoussef, *Journal of Superconductivity and Novel Magnetism* **30**, 3221 (2017).
- [90] J. Chen, H.-S. Hsu, Y.-H. Huang, and D.-J. Huang, *Physical Review B* **98**, 085141 (2018).
- [91] G. Sai Gautam and E. A. Carter, *Physical Review Materials* **2**, 095401 (2018).
- [92] J. P. Wright, J. P. Attfield, and P. G. Radaelli, *Physical Review Letters* **87**, 266401 (2001).
- [93] J. P. Wright, J. P. Attfield, and P. G. Radaelli, *Physical Review B* **66**, 214422 (2002).
- [94] S. K. Park, T. Ishikawa, and Y. Tokura, *Physical Review B* **58**, 3717 (1998).
- [95] D. Schrupp, M. Sing, M. Tsunekawa, H. Fujiwara, S. Kasai, A. Sekiyama, S. Suga, T. Muro, V. A. M. Brabers, and R. Claessen, *Europhysics Letters* **70**, 789 (2005).
- [96] S. F. Alvarado and P. S. Bagus, *Physics Letters A* **67**, 397 (1978).
- [97] J. Slater, *Quantum theory of atomic structure*, Vol. 2 (McGraw-Hill, New York, 1960).
- [98] S. F. Alvarado, W. Eib, F. Meier, D. T. Pierce, K. Sattler, H. C. Siegmann, and J. P. Remeika, *Physical Review Letters* **34**, 319 (1975).
- [99] E. Kay, R. A. Sigsbee, G. L. Bona, M. Taborelli, and H. C. Siegmann, *Applied Physics Letters* **47**, 533 (1985).
- [100] H.-J. Kim, J.-H. Park, and E. Vescovo, *Physical Review B* **61**, 15288 (2000).
- [101] S. A. Morton, G. D. Waddill, S. Kim, I. K. Schuller, S. A. Chambers, and J. G. Tobin, *Surface Science Letters* **513**, L451 (2002).
- [102] E. Vescovo, H.-J. Kim, J. M. Ablett, and S. A. Chambers, *Journal of Applied Physics* **98**, 084507 (2005).
- [103] M. Fonin, Y. S. Dedkov, R. Pentcheva, U. Rüdiger, and G. Güntherodt, *Journal of Physics: Condensed Matter* **19**, 315217 (2007).
- [104] M. Fonin, R. Pentcheva, Y. S. Dedkov, M. Sperlich, D. V. Vyalikh, M. Scheffler, U. Rüdiger, and G. Güntherodt, *Physical Review B* **72**, 104436 (2005).
- [105] M. Fonin, Y. S. Dedkov, R. Pentcheva, U. Rüdiger, and G. Güntherodt, *Journal of Physics: Condensed Matter* **20**, 142201 (2008).

- [106] D. J. Huang, C. F. Chang, J. Chen, L. H. Tjeng, A. D. Rata, W. P. Wu, S. C. Chung, H. J. Lin, T. Hibma, and C. T. Chen, *Journal of Magnetism and Magnetic Materials* **239**, 261 (2002).
- [107] S. F. Alvarado, W. Eib, H. C. Siegmann, and J. P. Remeika, *Journal of Magnetism and Magnetic Materials* **3**, 121 (1976).
- [108] J. G. Tobin, S. A. Morton, S. W. Yu, G. D. Waddill, I. K. Schuller, and S. A. Chambers, *Journal of Physics: Condensed Matter* **19**, 315218 (2007).
- [109] Y. S. Dedkov, U. Rüdiger, and G. Güntherodt, *Physical Review B* **65**, 064417 (2002).
- [110] T. Kiss, T. Shimojima, F. Kanetaka, K. Kanai, T. Yokoya, S. Shin, Y. Onuki, T. Togashi, C. Zhang, C. Chen, and S. Watanabe, *Journal of Electron Spectroscopy and Related Phenomena* **144–147**, 953 (2005).
- [111] S. Suga and A. Sekiyama, *Photoelectron Spectroscopy: Bulk and Surface Electronic Structure* (Springer, Heidelberg, 2014).
- [112] H. Hertz, *Annalen der Physik* **267**, 983 (1887).
- [113] A. Einstein, *Annalen der Physik* **14**, 164 (1905).
- [114] S. Hüfner, *Photoelectron Spectroscopy: Principles and Applications*, Third (Springer, 2003).
- [115] A. Damascelli, *Physica Scripta* **T109**, 61 (2004).
- [116] R. Claessen, *Photoelectron spectroscopy: The joys and pitfalls of the photoelectric effect*, Les Houches, 2017.
- [117] S. Moser, *Journal of Electron Spectroscopy and Related Phenomena* **214**, 29 (2017).
- [118] L. Hedin and J. Lee, *Journal of Electron Spectroscopy and Related Phenomena* **124**, 289 (2002).
- [119] S. Tanuma, C. J. Powell, and D. R. Penn, *Surface and Interface Analysis* **21**, 165 (1993).
- [120] S. Tanuma, C. J. Powell, and D. R. Penn, *Surface and Interface Analysis* **36**, 1 (2004).
- [121] C. J. Powell and S. Tanuma, *Hard X-ray Photoelectron Spectroscopy (HAXPES)*, edited by J. C. Woicik, Vol. 59 (Springer, 2016).
- [122] M. P. Seah and W. A. Dench, *Surface and Interface Analysis* **1**, 2 (1979).
- [123] J. Yeh and I. Lindau, *Atomic Data and Nuclear Data Tables* **32**, 1 (1985).
- [124] M. Trzhaskovskaya and V. Yarzhemsky, *Atomic Data and Nuclear Data Tables* **119**, 99 (2018).
- [125] Z. Hussain, C. S. Fadley, S. Kono, and L. F. Wagner, *Physical Review B* **22**, 3750 (1980).
- [126] L. Plucinski, J. Minár, B. C. Sell, J. Braun, H. Ebert, C. M. Schneider, and C. S. Fadley, *Physical Review B* **78**, 035108 (2008).

- [127] C. Kittel and C. Y. Fong, *Quantum theory of solids*, 2nd rev. print (Wiley, New York, 1987).
- [128] A. X. Gray, C. Papp, S. Ueda, B. Balke, Y. Yamashita, L. Plucinski, J. Minár, J. Braun, E. R. Ylvisaker, C. M. Schneider, W. E. Pickett, H. Ebert, K. Kobayashi, and C. S. Fadley, *Nature Materials* **10**, 759 (2011).
- [129] R. C. White, C. S. Fadley, M. Sagurton, and Z. Hussain, *Physical Review B* **34**, 5226 (1986).
- [130] A. X. Gray, J. Minár, S. Ueda, P. R. Stone, Y. Yamashita, J. Fujii, J. Braun, L. Plucinski, C. M. Schneider, G. Panaccione, H. Ebert, O. D. Dubon, K. Kobayashi, and C. S. Fadley, *Nature Materials* **11**, 957 (2012).
- [131] A. Keqi, M. Gehlmann, G. Conti, S. Nemšák, A. Rattanachata, J. Minár, L. Plucinski, J. E. Rault, J. P. Rueff, M. Scarpulla, M. Hategan, G. K. Pálsson, C. Conlon, D. Eiteneer, A. Y. Saw, A. X. Gray, K. Kobayashi, S. Ueda, O. D. Dubon, C. M. Schneider, and C. S. Fadley, *Physical Review B* **97**, 155149 (2018).
- [132] S. Babenkov, K. Medjanik, D. Vasilyev, S. Chernov, C. Schlueter, A. Gloskovskii, Y. Matveyev, W. Drube, B. Schönhense, K. Rossnagel, H.-J. Elmers, and G. Schönhense, *Communications Physics* **2**, 107 (2019).
- [133] A. Rattanachata, L. C. Nicolai, H. P. Martins, G. Conti, M. J. Verstraete, M. Gehlmann, S. Ueda, K. Kobayashi, I. Vishik, C. M. Schneider, C. S. Fadley, A. X. Gray, J. Minár, and S. Nemšák, *Physical Review Materials* **5**, 055002 (2021).
- [134] ScientaOmicron, *HAXPES Lab - A window to the bulk* - <https://scientaomicron.com/en/system-solutions/electron-spectroscopy/HAXPES-Lab>, 2018.
- [135] DESY, *X-ray spectroscopy beamline P22 - Technical Design Report*, 2014.
- [136] E. Beaurepaire, ed., *Magnetism: a synchrotron radiation approach*, Lecture Notes in Physics 697 (Springer, Berlin, 2006).
- [137] DESY, *PETRA III - Facility Information*, https://photon-science.desy.de/facilities/petra_iii/facility_information/index_eng.html.
- [138] N. Bohr, *The London, Edinburgh, and Dublin Philosophical Magazine and Journal of Science* **26**, 1 (1913).
- [139] Tatoute, *Licensed under Creative Commons BY-SA 4.0*, https://commons.wikimedia.org/wiki/File:Stern-Gerlach_experiment_svg.svg, 2014.
- [140] J. Kirschner, *Polarized Electrons at Surfaces* (Springer-Verlag Berlin, 1985).
- [141] N. Mott and H. Massey, *The theory of atomic collision*, 3rd Edition (Oxford Clarendon Press, 1965).
- [142] T. Okuda, *Journal of Physics: Condensed Matter* **29**, 483001 (2017).
- [143] G.-C. Wang, R. J. Celotta, and D. T. Pierce, *Physical Review B* **23**, 1761 (1981).
- [144] J. Unguris, D. T. Pierce, and R. J. Celotta, *Review of Scientific Instruments* **57**, 1314 (1986).

- [145] C. Tusche, M. Ellguth, A. A. Ünal, C.-T. Chiang, A. Winkelmann, A. Krasnyuk, M. Hahn, G. Schönhense, and J. Kirschner, *Applied Physics Letters* **99**, 032505 (2011).
- [146] D. Kutnyakhov, P. Lushchyk, A. Fognini, D. Perriard, M. Kolbe, K. Medjanik, E. Fedchenko, S. A. Nepijko, H.-J. Elmers, G. Salvatella, C. Stieger, R. Gort, T. Bähler, T. Michlmayer, Y. Acremann, A. Vaterlaus, F. Giebels, H. Gollisch, R. Feder, C. Tusche, A. Krasnyuk, J. Kirschner, and G. Schönhense, *Ultramicroscopy* **130**, 63 (2013).
- [147] D. Vasilyev, C. Tusche, F. Giebels, H. Gollisch, R. Feder, and J. Kirschner, *Journal of Electron Spectroscopy and Related Phenomena* **199**, 10 (2015).
- [148] G. Stryganyuk, X. Kozina, G. H. Fecher, S. Ouardi, S. Chadov, C. Felser, G. Schönhense, P. Lushchyk, A. Oelsner, P. Bernhard, E. Ikenaga, T. Sugiyama, H. Sukegawa, Z. Wen, K. Inomata, and K. Kobayashi, *Japanese Journal of Applied Physics* **51**, 016602 (2012).
- [149] X. Kozina, E. Ikenaga, C. E. Viol Barbosa, S. Ouardi, J. Karel, M. Yamamoto, K. Kobayashi, H. J. Elmers, G. Schönhense, and C. Felser, *Journal of Electron Spectroscopy and Related Phenomena* **211**, 12 (2016).
- [150] S.-R. Lin, *Physical Review* **133**, A965 (1964).
- [151] M. Getzlaff, B. Heidemann, J. Bansmann, C. Westphal, and G. Schönhense, *Review of Scientific Instruments* **69**, 3913 (1998).
- [152] R. Gauvin and D. Drouin, *Scanning* **15**, 140 (1993).
- [153] G. Ghiringhelli, K. Larsson, and N. B. Brookes, *Review of Scientific Instruments* **70**, 4225 (1999).
- [154] V. N. Strocov, V. N. Petrov, and J. H. Dil, *Journal of Synchrotron Radiation* **22**, 708 (2015).
- [155] R. Feder, *Physica Status Solidi B* **49**, 699 (1972).
- [156] R. Feder, *Physica Status Solidi B* **62**, 135 (1974).
- [157] R. Feder, *Physical Review Letters* **36**, 598 (1976).
- [158] M. Kolbe, P. Lushchyk, B. Petereit, H.-J. Elmers, G. Schönhense, A. Oelsner, C. Tusche, and J. Kirschner, *Physical Review Letters* **107**, 207601 (2011).
- [159] M. Schmitt, O. Kirilmaz, S. Chernov, S. Babenkov, D. Vasilyev, O. Fedchenko, K. Medjanik, Y. Matveyev, A. Gloskovskii, C. Schlueter, A. Winkelmann, L. Dudy, H.-J. Elmers, G. Schönhense, M. Sing, and R. Claessen, *Physical Review B* **104**, 045129 (2021).
- [160] C. Tusche, A. Krasnyuk, and J. Kirschner, *Ultramicroscopy* **159**, 520 (2015).
- [161] E. D. Schaefer, S. Borek, J. Braun, J. Minár, H. Ebert, K. Medjanik, D. Kutnyakhov, G. Schönhense, and H.-J. Elmers, *Physical Review B* **95**, 104423 (2017).
- [162] J. Kirschner, F. Giebels, H. Gollisch, and R. Feder, *Physical Review B* **88**, 125419 (2013).

- [163] D. Kutnyakhov, “Imaging spin-filter efficiency of W(001) and Ir(001) single crystals”, Doctoral Thesis (Mainz, 2014).
- [164] U. Heinzmann, *Journal of Physics B: Atomic and Molecular Physics* **11**, 399 (1978).
- [165] E. Kisker, R. Clauberg, and W. Gudat, *Review of Scientific Instruments* **53**, 1137 (1982).
- [166] L. G. Gray, M. W. Hart, F. B. Dunning, and G. K. Walters, *Review of Scientific Instruments* **55**, 88 (1984).
- [167] D. Tillmann, R. Thiel, and E. Kisker, *Zeitschrift für Physik B Condensed Matter* **77**, 1 (1989).
- [168] S. Qiao, A. Kimura, A. Harasawa, M. Sawada, J.-G. Chung, and A. Kakizaki, *Review of Scientific Instruments* **68**, 4390 (1997).
- [169] F. U. Hillebrecht, R. M. Jungblut, L. Wiebusch, C. Roth, H. B. Rose, D. Knabben, C. Bethke, N. B. Weber, S. Manderla, U. Rosowski, and E. Kisker, *Review of Scientific Instruments* **73**, 1229 (2002).
- [170] V. N. Petrov, V. V. Grebenshikov, A. N. Andronov, P. G. Gabdullin, and A. V. Maslevtcov, *Review of Scientific Instruments* **78**, 025102 (2007).
- [171] A. Winkelmann, D. Hartung, H. Engelhard, C.-T. Chiang, and J. Kirschner, *Review of Scientific Instruments* **79**, 083303 (2008).
- [172] T. Okuda, Y. Takeichi, Y. Maeda, A. Harasawa, I. Matsuda, T. Kinoshita, and A. Kakizaki, *Review of Scientific Instruments* **79**, 123117 (2008).
- [173] C. M. Cacho, S. Vlais, M. Malvestuto, B. Ressel, E. A. Seddon, and F. Parmigiani, *Review of Scientific Instruments* **80**, 043904 (2009).
- [174] C. Jozwiak, J. Graf, G. Lebedev, N. Andresen, A. K. Schmid, A. V. Fedorov, F. El Gabaly, W. Wan, A. Lanzara, and Z. Hussain, *Review of Scientific Instruments* **81**, 053904 (2010).
- [175] C. Tusche, M. Ellguth, A. Krasnyuk, A. Winkelmann, D. Kutnyakhov, P. Lushchyk, K. Medjanik, G. Schönhense, and J. Kirschner, *Ultramicroscopy* **130**, 70 (2013).
- [176] S. Suga and C. Tusche, *Journal of Electron Spectroscopy and Related Phenomena* **200**, 119 (2015).
- [177] U. Gelius, E. Basilier, S. Svensson, T. Bergmark, and K. Siegbahn, *Journal of Electron Spectroscopy and Related Phenomena* **2**, 405 (1974).
- [178] A. Oelsner, O. Schmidt, M. Schicketanz, M. Klais, G. Schönhense, V. Mergel, O. Jagutzki, and H. Schmidt-Böcking, *Review of Scientific Instruments* **72**, 3968 (2001).
- [179] C. Tusche, Y.-J. Chen, C. M. Schneider, and J. Kirschner, *Ultramicroscopy* **206**, 112815 (2019).
- [180] C. E. Kuyatt and J. A. Simpson, *Review of Scientific Instruments* **38**, 103 (1967).
- [181] B. Tonner, *Nuclear Instruments and Methods in Physics Research Section A: Accelerators, Spectrometers, Detectors and Associated Equipment* **291**, 60 (1990).

- [182] J. C. Vickerman, *Surface Analysis: The Principal Techniques*, First Edition (John Wiley & Sons Ltd, 1997).
- [183] M. Escher, N. Weber, M. Merkel, C. Ziethen, P. Bernhard, G. Schönhense, S. Schmidt, F. Forster, F. Reinert, B. Krömker, and D. Funnemann, *Journal of Physics: Condensed Matter* **17**, S1329 (2005).
- [184] L. Weng, G. Vereecke, M. Genet, P. Bertrand, and W. Stone, *Surface and Interface Analysis* **20**, 179 (1993).
- [185] D. Yu, C. Math, M. Meier, M. Escher, G. Rangelov, and M. Donath, *Surface Science* **601**, 5803 (2007).
- [186] K. Zakeri, T. R. F. Peixoto, Y. Zhang, and J. Kirschner, *Surface Science* **604**, L1 (2010).
- [187] J.-M. Chen and C. A. Papageorgopoulos, *Surface Science* **20**, 195 (1970).
- [188] H.-W. Fink and G. Ehrlich, *Surface Science Letters* **110**, L611 (1987).
- [189] K. J. Rawlings, S. D. Foulis, and B. J. Hopkins, *Journal of Physics C: Solid State Physics* **14**, 5411 (1987).
- [190] J. A. Becker, E. J. Becker, and R. G. Brandes, *Journal of Applied Physics* **32**, 411 (1961).
- [191] Y. Viswanath and L. D. Schmidt, *The Journal of Chemical Physics* **59**, 4184 (1973).
- [192] N. Avery, *Surface Science* **33**, 107 (1972).
- [193] J. C. Buchholz, G.-C. Wang, and M. G. Lagally, *Surface Science* **49**, 508 (1975).
- [194] B. J. Hopkins, G. D. Watts, and A. R. Jones, *Surface Science* **52**, 715 (1975).
- [195] Y. Ptushinskii and B. A. Chuikov, *Surface Science* **6**, 42 (1967).
- [196] N. Vas'ko, Y. Ptushinskii, and B. A. Chuikov, *Surface Science* **14**, 448 (1969).
- [197] D. Ollis and M. Boudart, *Surface Science* **23**, 320 (1970).
- [198] J. B. Benzinger, E. I. Ko, and R. J. Madix, *Journal of Catalysis* **54**, 414 (1978).
- [199] R. L. Park and H. H. Madden, *Surface Science* **11**, 188 (1968).
- [200] E. Bauer, *Surface Science* **7**, 351 (1967).
- [201] H.-W. Wassmuth, *Annalen der Physik* **481**, 326 (1971).
- [202] D. M. Lind, S. D. Berry, G. Chern, H. Mathias, and L. R. Testardi, *Physical Review B* **45**, 1838 (1992).
- [203] J. Kirschner and R. Feder, *Surface Science* **104**, 448 (1981).
- [204] K. Medjanik, S. V. Babenkov, S. Chernov, D. Vasilyev, B. Schönhense, C. Schlueter, A. Gloskovskii, Y. Matveyev, W. Drube, H.-J. Elmers, and G. Schönhense, *Journal of Synchrotron Radiation* **26**, 1996 (2019).

- [205] C. Tusche, P. Goslawski, D. Kutnyakhov, M. Ellguth, K. Medjanik, H. J. Elmers, S. Chernov, R. Wallauer, D. Engel, A. Jankowiak, and G. Schönhense, *Applied Physics Letters* **108**, 261602 (2016).
- [206] ScientaOmicron, *DA30-L - First Deflector Analyser Preserving Measurement Geometry* - <https://scientaomicron.com/en/Components/Electron-Analysers/DA30-L>.
- [207] MBSscientific, *MBS A-1 Analyser - Extremely High Energy Resolution Photoelectron Analyser* - <https://mbscientific.se/products.php?ca=36&pr=64&m=109>.
- [208] G. Schönhense, A. Oelsner, O. Schmidt, G. H. Fecher, V. Mergel, O. Jagutzki, and H. Schmidt-Böcking, *Surface Science* **480**, 180 (2001).
- [209] Y. Uehara, T. Ushiroku, S. Ushioda, and Y. Murata, *Japanese Journal of Applied Physics* **29**, 2858 (1990).
- [210] B. Schönhense, K. Medjanik, O. Fedchenko, S. Chernov, M. Ellguth, D. Vasilyev, A. Oelsner, J. Viefhaus, D. Kutnyakhov, W. Wurth, H. J. Elmers, and G. Schönhense, *New Journal of Physics* **20**, 033004 (2018).
- [211] G. Schönhense, D. Kutnyakhov, F. Pressacco, M. Heber, N. Wind, S. Y. Agustsson, S. Babenkov, D. Vasilyev, O. Fedchenko, S. Chernov, L. Rettig, B. Schönhense, L. Wenthaus, G. Brenner, S. Dziarzhyski, S. Palutke, S. K. Mahatha, N. Schirmel, H. Redlin, B. Manschwetus, I. Hartl, Y. Matveyev, A. Gloskovskii, C. Schlueter, V. Shokeen, H. Duerr, T. K. Allison, M. Beye, K. Rossnagel, H. J. Elmers, and K. Medjanik, *Review of Scientific Instruments* **92**, 053703 (2021).
- [212] G. Schönhense, K. Medjanik, C. Tusche, M. de Loos, B. van der Geer, M. Scholz, F. Hieke, N. Gerken, J. Kirschner, and W. Wurth, *Ultramicroscopy* **159**, 488 (2015).
- [213] A. J. C. Wilson, *Acta Crystallographica* **3**, 80 (1950).
- [214] R. E. DeWames and W. F. Hall, *Acta Crystallographica Section A* **24**, 206 (1968).
- [215] A. Winkelmann, B. Schröter, and W. Richter, *Physical Review B* **69**, 245417 (2004).
- [216] K. Siegbahn, U. Gelius, H. Siegbahn, and E. Olson, *Physica Scripta* **1**, 272 (1970).
- [217] S. Goldberg, R. Baird, S. Kono, N. Hall, and C. Fadley, *Journal of Electron Spectroscopy and Related Phenomena* **21**, 1 (1980).
- [218] O. Fedchenko, A. Winkelmann, K. Medjanik, S. Babenkov, D. Vasilyev, S. Chernov, C. Schlueter, A. Gloskovskii, Y. Matveyev, W. Drube, B. Schönhense, H.-J. Elmers, and G. Schönhense, *New Journal of Physics* **21**, 113031 (2019).
- [219] T. Claesson, M. Månsson, C. Dallera, F. Venturini, C. D. Nadaï, N. B. Brookes, and O. Tjernberg, *Physical Review Letters* **93**, 136402 (2004).
- [220] N. Kamakura, Y. Takata, T. Tokushima, Y. Harada, A. Chainani, K. Kobayashi, and S. Shin, *Europhysics Letters* **67**, 240 (2004).
- [221] A. Sekiyama, S. Kasai, M. Tsunekawa, Y. Ishida, M. Sing, A. Irizawa, A. Yamasaki, S. Imada, T. Muro, Y. Saitoh, Y. Ōnuki, T. Kimura, Y. Tokura, and S. Suga, *Physical Review B* **70**, 060506 (2004).

- [222] C. Papp, L. Plucinski, J. Minar, J. Braun, H. Ebert, C. M. Schneider, and C. S. Fadley, *Physical Review B* **84**, 045433 (2011).
- [223] G. Schönhense, K. Medjanik, S. Babenkov, D. Vasilyev, M. Ellguth, O. Fedchenko, S. Chernov, B. Schönhense, and H.-J. Elmers, *Communications Physics* **3**, 45 (2020).
- [224] K. Medjanik, O. Fedchenko, S. Chernov, D. Kutnyakhov, M. Ellguth, A. Oelsner, B. Schönhense, T. R. F. Peixoto, P. Lutz, C.-H. Min, F. Reinert, S. Däster, Y. Acremann, J. Viefhaus, W. Wurth, H. J. Elmers, and G. Schönhense, *Nature Materials* **16**, 615 (2017).
- [225] G. Schönhense, S. Babenkov, D. Vasilyev, H.-J. Elmers, and K. Medjanik, *Review of Scientific Instruments* **91**, 123110 (2020).
- [226] B. Wannberg, *Journal of Physics E: Scientific Instruments* **7**, 149 (1974).
- [227] B. Wannberg, *Nuclear Instruments and Methods in Physics Research Section A: Accelerators, Spectrometers, Detectors and Associated Equipment* **601**, 182 (2009).
- [228] R. Herzog, *Zeitschrift für Physik* **97**, 596 (1935).
- [229] K. Jost, *Journal of Physics E: Scientific Instruments* **12**, 1006 (1979).
- [230] K. Jost, *Journal of Physics E: Scientific Instruments* **12**, 1001 (1979).
- [231] R. E. Imhof, A. Adams, and G. C. King, *Journal of Physics E: Scientific Instruments* **9**, 138 (1976).
- [232] O. Sise and T. J. M. Zouros, *Journal of Spectroscopy* **2015**, 1 (2015).
- [233] T. Zouros and E. Benis, *Journal of Electron Spectroscopy and Related Phenomena* **125**, 221 (2002).
- [234] E. Benis and T. Zouros, *Journal of Electron Spectroscopy and Related Phenomena* **163**, 28 (2008).
- [235] B. Krömker, M. Escher, D. Funnemann, D. Hartung, H. Engelhard, and J. Kirschner, *Review of Scientific Instruments* **79**, 053702 (2008).
- [236] M. Volkel and W. Sandner, *Journal of Physics E: Scientific Instruments* **16**, 456 (1983).
- [237] *G. Schönhense, Private communication (University of Mainz).*
- [238] V. N. Strocov, *Journal of Electron Spectroscopy and Related Phenomena* **229**, 100 (2018).
- [239] J. P. Rogers, P. H. Cutler, T. E. Feuchtwang, and N. Miskovsky, *Surface Science* **141**, 61 (1984).
- [240] J. P. Rogers, P. H. Cutler, T. E. Feuchtwang, and A. A. Lucas, *Surface Science* **181**, 436 (1987).
- [241] S. Das Sarma, S. Adam, E. H. Hwang, and E. Rossi, *Reviews of Modern Physics* **83**, 407 (2011).

- [242] T. Straub, R. Claessen, P. Steiner, S. Hübner, V. Eyert, K. Friemelt, and E. Bucher, *Physical Review B* **55**, 13473 (1997).
- [243] M. Paul, D. Kufer, A. Müller, S. Brück, E. Goering, M. Kamp, J. Verbeeck, H. Tian, G. Van Tendeloo, N. J. C. Ingle, M. Sing, and R. Claessen, *Applied Physics Letters* **98**, 012512 (2011).
- [244] A. Müller, A. Ruff, M. Paul, A. Wetscherek, G. Berner, U. Bauer, C. Praetorius, K. Fauth, M. Przybylski, M. Gorgoi, M. Sing, and R. Claessen, *Thin Solid Films* **520**, 368 (2011).
- [245] O. Kirilmaz, “Thin film growth and characterization of the transition metal oxides magnetite and layered perovskite iridates”, *Doctoral Thesis (Würzburg, 2019)*.
- [246] A. Barbieri, W. Weiss, M. A. van Hove, and G. A. Somorjai, *Surface Science* **302**, 259 (1994).
- [247] C. Schlueter, A. Gloskovskii, K. Ederer, I. Schostak, S. Piec, I. Sarkar, Y. Matveyev, P. Lömker, M. Sing, R. Claessen, C. Wiemann, C. M. Schneider, K. Medjanik, G. Schönhense, P. Amann, A. Nilsson, and W. Drube, in *13th International Conference on Synchrotron Radiation Instrumentation - SRI2018*, Vol. 2054 (2019), p. 040010.
- [248] P. Kuiper, B. Searle, L.-C. Duda, R. Wolf, and P. van der Zaag, *Journal of Electron Spectroscopy and Related Phenomena* **86**, 107 (1997).
- [249] J. Chen, D. J. Huang, A. Tanaka, C. F. Chang, S. C. Chung, W. B. Wu, and C. T. Chen, *Physical Review B* **69**, 085107 (2004).
- [250] E. Goering, *Physica Status Solidi B* **248**, 2345 (2011).
- [251] E. Goering, S. Gold, M. Lafkioti, and G. Schütz, *Europhysics Letters* **73**, 97 (2006).
- [252] J. Schlappa, C. Schüßler-Langeheine, C. F. Chang, H. Ott, A. Tanaka, Z. Hu, M. W. Haverkort, E. Schierle, E. Weschke, G. Kaindl, and L. H. Tjeng, *Physical Review Letters* **100**, 026406 (2008).
- [253] Y. S. Dedkov, M. Fonin, D. V. Vyalikh, J. O. Hauch, S. L. Molodtsov, U. Rüdiger, and G. Güntherodt, *Physical Review B* **70**, 073405 (2004).
- [254] P. G. Steeneken, L. H. Tjeng, I. Elfimov, G. A. Sawatzky, G. Ghiringhelli, N. B. Brookes, and D.-J. Huang, *Physical Review Letters* **88**, 047201 (2002).
- [255] L. L. Lev, D. V. Averyanov, A. M. Tokmachev, F. Bisti, V. A. Rogalev, V. N. Strocov, and V. G. Storchak, *Journal of Materials Chemistry C* **5**, 192 (2017).
- [256] S. F. Alvarado, *Zeitschrift für Physik B* **33**, 51 (1979).
- [257] D. Mauri, D. Scholl, H. C. Siegmann, and E. Kay, *Physical Review Letters* **61**, 758 (1988).
- [258] C. Schroer, *PETRA IV: Upgrade of PETRA III to the Ultimate 3D X-ray Microscope - Conceptual Design Report (CDR)* (Deutsches Elektronen-Synchrotron, DESY, Hamburg, 2019).
- [259] C. Schlueter, *Private communication (Beamline P22, PETRA III)*.

Appendix

Previous theoretical studies on magnetite

Table A.1: Theoretical calculations based on various approximations and their predicted bulk spin polarization P

Authors	Year	Implementation	P at E_F (%)
Alvarado and Bagus [96]	1978	single ion model	-66.7^b
Yanase and Siratori [63]	1984	APW	-100
de Groot and Buschow [64]	1986	GGA(ASW)	-100
Zhang and Satpathy [65]	1991	LSDA(LMTO)	-100
Pénicaud <i>et al.</i> [66]	1992	GGA(ASW)	-100
Anisimov <i>et al.</i> [67]	1996	LSDA	-100
Yanase and Hamada [68]	1999	APW	-100
Antonov <i>et al.</i> [69, 70]	2001, 2003	LSDA+U	-100
Jeng <i>et al.</i> [71–73]	2002, 2004, 2006	LSDA/LDA+U	-100
Szotek <i>et al.</i> [74]	2003	LSDA	-100
Leonov <i>et al.</i> [75]	2004	LSDA+U(TBLMTO)	-100
Madsen and Novák [76]	2005	LDA+U(FLL-DCC)	-100
Pentcheva <i>et al.</i> [52]	2005	GGA(APW)	-40^a
Pinto and Elliott [77]	2006	GGA+U(PAW)	-100
Zhu <i>et al.</i> [53]	2006	LDA+U	-100
Łodziana [78]	2007	GGA+U	$> -100^a$
Piekarz <i>et al.</i> [79, 80]	2007, 2010	GGA(+U)	-100
Rowan <i>et al.</i> [81]	2009	GGA	-100
Yu <i>et al.</i> [82]	2012	GGA+U	-100
Arras <i>et al.</i> [83]	2013	LSDA+U(APW)	-100
Wang <i>et al.</i> [84]	2013	GGA+U	-100
Noh <i>et al.</i> [85]	2014	GGA+U	-100
Schmitz <i>et al.</i> [86]	2014	GGA+U	-100
Liu <i>et al.</i> [87, 88]	2017, 2019	GGA+U/SCC-DFTB	-100
Mounkachi <i>et al.</i> [89]	2017	LSDA	-100
Chen <i>et al.</i> [90]	2018	GGA(+U)	-100
Sai Gautam and Carter [91]	2018	SCAN(+U)(PAW)	-100

^aCalculations were done explicitly for the surface of $\text{Fe}_3\text{O}_4(001)$.

^bRepresents the photoelectron spin polarization of the whole Fe^{2+} $3d$ shell.

Two-dimensional Delayline Detector

The working principle of a DLD is shown in Fig. A.1. It consists of two perpendicular meandering delaylines X and Y, which are covered with an MCP. In contrast to a channeltron, which is a one-dimensional detector, an MCP consists of many small holes in the μm range providing a lateral resolution of down to $30\ \mu\text{m}$ and therefore supports two-dimensional imaging. When a photoelectron hits the MCP, due to the applied voltage between the front and backside, an electron avalanche of secondary electrons is generated. When such an electron strikes the delayline in the X-direction below the MCP, an electrical pulse moves in both directions at the speed of light and is registered in relation to an external time reference signal by the electronics input X_1 and X_2 . There is a time delay Δt_x between both signals and the arrival time is then averaged over X_1 and X_2 . The same is done for the delayline Y and with both time signals Δt_x and Δt_y the impact position can now be determined very precisely, providing a two-dimensional information of the electron distribution. Especially when featuring TOF recording, the measuring speed of such a detector has significant impact on the energy resolution, since the kinetic energy is encoded in the time-of-flight, as discussed in Sec. 5.2.2 [178]. Typical values for the measuring frequency of a DLD is below 200 ps.

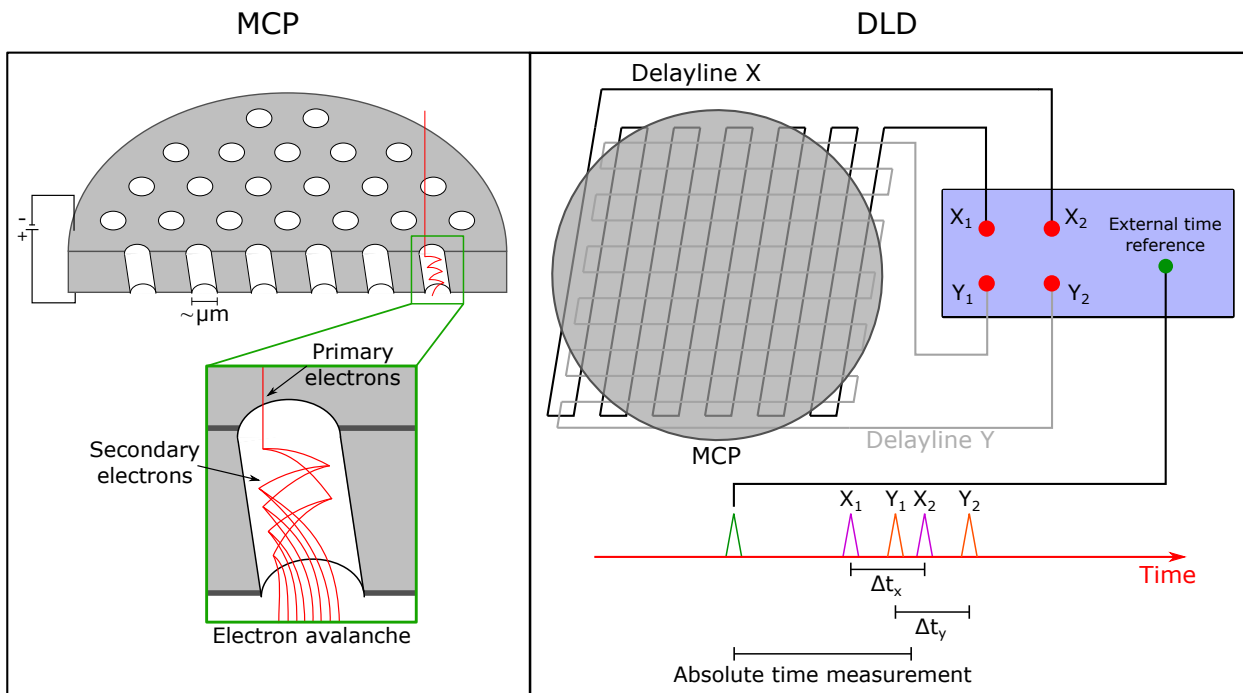


Figure A.1: Schematic view and working principle of an MCP (left) and a DLD (right): A voltage applied to the front and back of the MCP generates from an incoming photoelectron an electron avalanche of secondary electrons in each microchannel. The DLD has two delaylines—one in X- and the other one perpendicular in Y-direction, covered by the MCP. The electronics measure the time between a trigger signal and the signal from the delayline and can thus determine the position of impact on the detector.

Spin-filter Surface Preparation

W(001) spin-filter previously exposed to air

In the case that the spin-filter was previously exposed to ambient conditions, due to the huge amount of carbon that has migrated into the bulk, the crystal must be treated by several hundred LPFs until the pressure increase during each flash disappears (except for the small background). For this treatment reading the chamber pressure is sufficient and no RGA is needed. A time scan of the chamber pressure during the crystal preparation after exposure to air can be seen in Fig. A.2. In total, over 700 LPFs are required to ensure that all of the incorporated carbon migrates to the surface and is desorbed. This becomes clearly visible when single flashes are zoomed in. Here, the 10th, 280th, and 750th LPF cycles reflect the slowly changing pressure increase during each flash. This illustrates the importance of keeping the crystal under UHV conditions if possible.

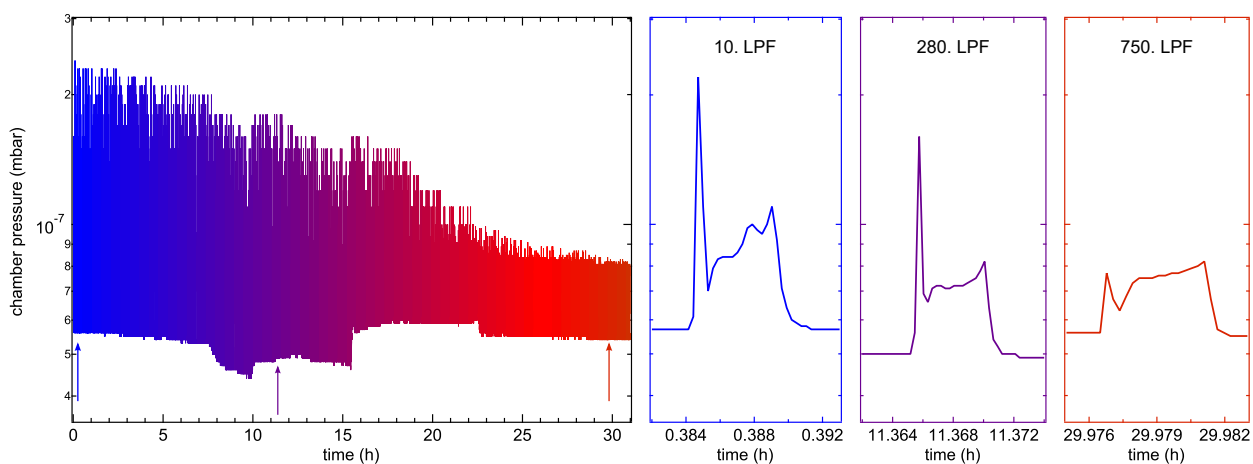


Figure A.2: Time scan of the chamber pressure during 750 LPFs after exposing the spin-filter crystal to ambient conditions. The 10th, 280th, and 750th LPF cycle was zoomed in.

Surface preparation with carbon contamination in the chamber

The LEED pattern of the W(001) after a full preparation cycle at 950 °C shown in Fig. A.3 (a) exhibits a (5x1) reconstruction, which indicates even higher carbon densities than shown in Fig. 5.9 (a), although both images were taken after preparation with the exact same parameters. Also at higher flashing temperatures the (5x1) reconstruction prevails. An analysis of the residual gas within the preparation chamber, which is shown as green curve in Fig. A.3 (b) reveals a high carbon contamination originating from different groups of hydrocarbon CH_x . Clearly, with this high amount of carbon in the atmosphere, an atomic clean crystal surface is not achievable. After cleaning and baking the system thoroughly, another RGA spectrum shows a tremendous decrease and also vanishing signal of these hydrocarbon groups. The LEED study in Sec. 5.1.2.2 was performed in the clean system, after this issue was solved.

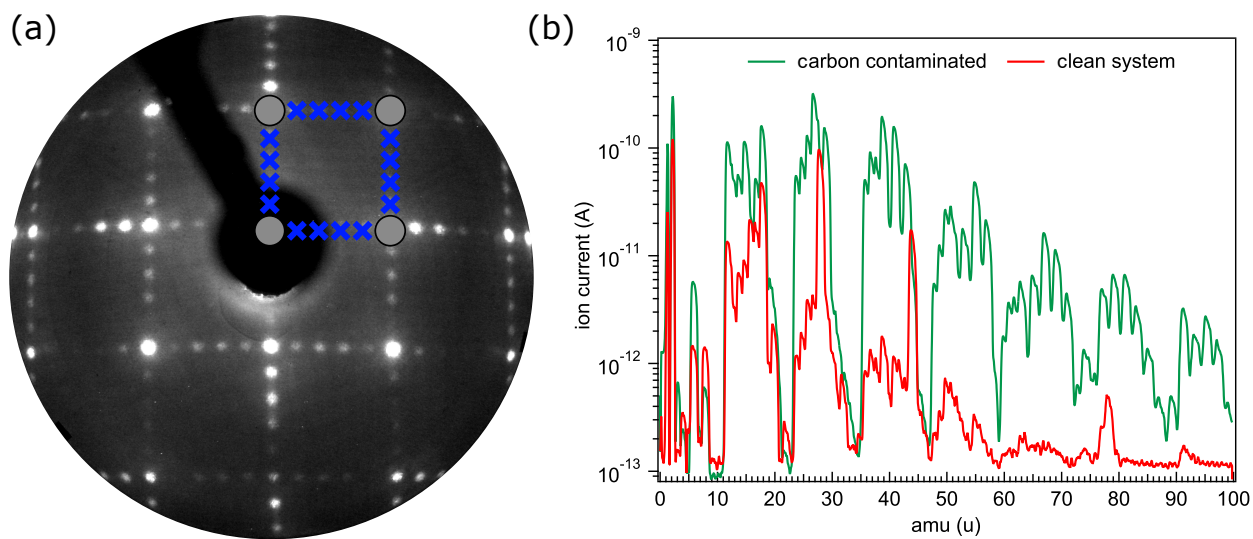


Figure A.3: (a) LEED image after a full preparation cycle showing a (5x1) reconstructed W(100) surface, indicating the highest amount of carbon reported in Ref. [198]. (b) RGA spectrum taken before (green) and after (red) cleaning and baking the system. A significant contamination with hydrocarbon groups CH_x of the preparation chamber can be seen.

List of Own Publications

- M. Zapf*, **M. Schmitt***, J. Gabel, P. Scheiderer, M. Stübinger, G. Sangiovanni, L. Dudy, S. Chernov, S. Babenkov, D. Vasilyev, O. Fedchenko, K. Medjanik, Yu. Matveyev, A. Gloskowskii, C. Schlueter, T.-L. Lee, H.-J. Elmers, G. Schönhense, M. Sing, and R. Claessen
Hard X-ray angle-resolved photoemission from a buried high mobility electron system
submitted to Physical Review B, arXiv:2110.15158
*Authors contributed equally.
- J. Gabel, M. Pickem, P. Scheiderer, L. Dudy, B. Leikert, M. Fuchs, M. Stübinger, **M. Schmitt**, J. Küspert, G. Sangiovanni, J.M. Tomczak, K. Held, T.-L. Lee, R. Claessen, and M. Sing
Toward Functionalized Ultrathin Oxide Films: The Impact of Surface Apical Oxygen
Advanced Electronic Materials 2021, 2101006 (2021)
- **M. Schmitt**, O. Kirilmaz, S. Chernov, S. Babenkov, D. Vasilyev, O. Fedchenko, K. Medjanik, Yu. Matveyev, A. Gloskowskii, C. Schlueter, A. Winkelmann, L. Dudy, H.-J. Elmers, G. Schönhense, M. Sing, and R. Claessen
Bulk spin polarization of magnetite from spin-resolved hard x-ray photoelectron spectroscopy
Physical Review B **104**, 045129 (2021)
- M. Stübinger, J. Gabel, P. Scheiderer, M. Zapf, **M. Schmitt**, P. Schütz, B. Leikert, J. Küspert, P. K. Thakur, T.-L. Lee, P. Potatov, A. Lubk, B. Büchner, M. Sing, and R. Claessen
Hard X-ray photoemission spectroscopy of $\text{LaVO}_3/\text{SrTiO}_3$: Band alignment and electronic reconstruction,
Physical Review B **103**, 235128 (2021), Editors' Suggestion
- B. Leikert, J. Gabel, **M. Schmitt**, M. Stübinger, P. Scheiderer, T.-L. Lee, M. Sing, and R. Claessen
Controlling the electronic interface of $\text{AlO}_x/\text{SrTiO}_3$ heterostructures
Physical Review Materials **5**, 065003 (2021)
- P. Scheiderer, **M. Schmitt**, J. Gabel, M. Zapf, M. Stübinger, P. Schütz, L. Dudy, C. Schlueter, T.-L. Lee, M. Sing, and R. Claessen
Tailoring materials for Motttronics: Excess oxygen doping of a prototypical Mott insulator,
Advanced Materials **30**, 1706708 (2018)

Danksagung

Zum Abschluss möchte ich mich bei einigen Menschen bedanken, die zum erfolgreichen Abschluss meiner Promotion beigetragen haben. Ein besonderer Dank geht dabei an:

Allen voran Prof. Dr. Ralph Claessen für die Betreuung dieser Arbeit und die freundliche Aufnahme am Lehrstuhl für Experimentelle Physik IV. Vor allem für das viele konstruktive Feedback, das mir stets geholfen hat meinen Horizont und mein Wissen erweitern zu können. Bedanken möchte ich mich auch für die Möglichkeit der Teilnahme unzähliger Strahlzeiten bei PETRA III, Diamond Light Source, Soleil und Elettra sowie der Summer School in Cargese, dem International Workshop on Oxide Electronics in Genua und der Teilnahme an diversen Frühjahrstagungen der DPG in Berlin, Regensburg und Dresden.

Ein weitere Dank geht an Prof. Dr. Sing. Lieber Michael, vielen Dank für deine ständige Hilfsbereitschaft bei physikalischen Fragen, technischen Problemen und auch die vielen Bürogespräche über aktuelle Tagespolitik. Das unzählige Korrekturlesen von Strahlzeitanträgen, Abstracts, Postern, Papern und nicht zuletzt dieser Arbeit. Deine konstruktive Kritik zum Schreiben und zur Darstellung wissenschaftlicher Daten hat mir immer sehr geholfen!

Des Weiteren möchte ich mich bei meinen Laborkollegen bedanken: Lenart Dudy—formerly known as *Commander Dudy always on duty*—der mich gerade zu Beginn meiner Promotion bei meinem Projekt unterstützt hat und von dem ich sehr viel über Labortechnik und Problemlösung lernen konnte. Auch für die Unterstützung unserer Strahlzeit bei seiner neuen Heimat Soleil ein großes Dankeschön. Ein weiterer Dank geht sowohl an Philipp Scheiderer, der mich schon während meiner Masterarbeit unterstützt hat, und Alexander Wiegand, der im Rahmen seiner Masterarbeit mich wiederum unterstützte, als auch an meinen langjährigen Bürokollegen Martin Stübinger, sowie meine Arbeitskollegen Berengar Leikert, Ozan Kirilmaz, Judith Gabel, Michael Zapf, Philipp Schütz, und natürlich dem ganzen Rest der EP4! Davon möchte ich noch ganz besonders Moni Seifer hervorheben, die für jedes Problem des bürokratischen Irrsinns immer eine Lösung parat hat.

Ein großer Dank geht auch an die Kollegen der Johannes Gutenberg-Universität Mainz. Allen voran Prof. Dr. Schönhense und Prof. Dr. Elmers. Lieber Gerd, lieber Hajo, vielen Dank für die viele experimentelle Entwicklung und die gute Zusammenarbeit vor Ort am Strahlrohr, die selbstverständlich auch zum Erfolg dieser Arbeit beigetragen hat. Von euch konnte ich viel Neues lernen und bestehendes Wissen vertiefen. An dieser Stelle ist natürlich auch die viele Arbeit von Katja Medjanik, Sergii Chernov, Olena Fedchenko, Sergey Babenkov und Dmitry Vasilyev hervorzuheben.

Auch dem Team von P09/P22 bei PETRA III (Christoph Schlueter, Andrei Gloskovskii, Yury Matveyev, Patrick Lömker, Katrin Ederer und Wolfgang Drube) möchte ich an dieser Stelle danken für die viele Unterstützung bei unseren Strahlzeiten Tag und Nacht und der Hilfe sowohl beim Projekt mit der Halbkugel als auch dem TOF-Instrument.

Abschließend möchte ich mich noch bei meinen Eltern und meinem Bruder für die Unterstützung in den letzten Jahren bedanken und dafür, dass ihr mir diesen Bildungsweg ermöglicht habt.